



**Universidade do Minho**  
Escola de Engenharia

Radouan Bouallala

**Mechanical performance of adhesively bonded innovative aeronautic carbon composites**

Mechanical performance of adhesively bonded innovative aeronautic carbon composites

Radouan Bouallala



**FRP++**

Advanced structural analysis and design using composite materials



UWimho | 2023

The European Master in Advanced Structural Analysis and Design using Composite Materials is a joint initiative of:



Universidade do Minho



UNIVERSITÀ DEGLI STUDI DI NAPOLI FEDERICO II



INSTITUT NATIONAL DES SCIENCES APPLIQUÉES TOULOUSE



UNIVERSITÉ TOULOUSE III PAUL SABATIER



Funded by the European Union

September 2023





**Universidade do Minho**  
Escola de Engenharia

Radouan Bouallala

## **Mechanical performance of adhesively bonded innovative aeronautic carbon composites**



**FRP++**

Advanced structural analysis and  
design using composite materials

Master Dissertation  
European Master in Advanced Structural Analysis and  
Design using Composite Materials

Work developed under the supervision of  
**Prof. Luís Correia**  
**Prof. Filipe Ribeiro**



Funded by  
the European Union

September 2023

## DECLARATION

**Name:** Radouan Bouallala

**Title of the Thesis:** Mechanical performance of adhesively bonded innovative aeronautic carbon composites

**Supervisors:**

Prof. Luís Correia

Prof. Filipe Ribeiro

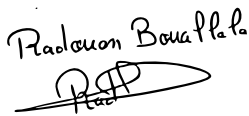
**Year of Conclusion:** 2023

Master Course in Advanced Structural Analysis and Design using Composite Materials

THE ENTIRE REPRODUCTION OF THIS THESIS IS AUTHORIZED ONLY FOR RESEARCH PURPOSES,  
UPON WRITTEN DECLARATION BY THE INTERESTED PERSON, WHICH IS COMMITTED TO.

University of Minho, 20/09/2023

Signature:

Radouan Bouallala  


## ACKNOWLEDGEMENTS

I would like to express my deepest gratitude and appreciation to all those who have supported and guided me throughout this dissertation journey.

First and foremost, I am immensely grateful to my supervisors, Doctor Luís Correia and Doctor Filipe Ribeiro, for their invaluable expertise, unwavering support, and insightful feedback. Their guidance and mentorship have been instrumental in shaping the direction and quality of this research. I am truly grateful for their patience, encouragement, and dedication.

I would like to express my sincere gratitude to the Erasmus Mundus project. The scholarship they provided was crucial to the success of this master's, allowing for total dedication to studying, doing experimental work and writing this dissertation.

I would like to express my sincere gratitude to Prof. José Sena Cruz and Rita Oliveira for their immense contribution to the success of this program. Their dedication and hard work were pivotal in achieving our goals, and we could not have done it without them.

I am deeply grateful to Prof. Albert Turon and Prof. Emilio Vicente for their great guidance in utilising ABAQUS. Additionally, I would like to express my sincere gratitude to Prof. Jordi Renart and Prof. Raul Campilho for providing me with their valuable assistance during my experimental test. Their support made a significant difference in the success of my project. Furthermore, I would like to express my sincere appreciation to all the ISQ, INEGI, OPTIMAL and PIEP members for their invaluable support in providing the necessary equipment for our tests. Your generosity and collaboration have been instrumental in our research efforts. I am also incredibly grateful and honoured to have received guidance and knowledge from the faculties and non-teaching staff involved in the FRP++ program. Their involvement provided me with a fresh perspective and invaluable knowledge, ultimately contributing to the successful completion of this work. Their expertise and passion within their respective fields have not only inspired me but also pushed me to strive for excellence.

I would like to extend my heartfelt appreciation to my family for their unconditional love, endless encouragement, and unwavering belief in me. Their constant support and sacrifices have been a source of strength throughout this journey. I am deeply grateful to my friends and colleagues, especially to Sarath Das, who have provided me with valuable insights, constructive discussions, and moral support. Their friendship and camaraderie have made this journey all the more enjoyable and memorable.

Thank you all from the bottom of my heart.

# **Desempenho mecânico e modelação numérica de ligações adesivas de materiais compósitos inovadores para aeronáutica**

## **RESUMO**

Devido ao impacto das viagens aéreas nas emissões de carbono, o setor da aviação busca materiais e tecnologias mais leves para reduzir emissões de CO<sub>2</sub>, NO<sub>x</sub> e ruído. Os materiais compósitos, substituindo estruturas tradicionais de alumínio em aeronaves, oferecem vantagens de peso, reduzindo o consumo de combustível e melhorando o desempenho. No entanto, a fixação de compósitos com elementos de fixação mecânicos, como parafusos e rebites, pode aumentar o peso estrutural. A ligação adesiva surge como uma solução potencial, proporcionando economia de peso sem comprometer a resistência. Existem desafios no desenho de ligações coladas adesivamente para compósitos, exigindo testes extensivos para determinar a resistência da ligação.

A presente tese teve como objetivo investigar ligações adesivas entre materiais compósitos de carbono. O estudo envolveu a caracterização experimental do adesivo epóxi 3M™ Scotch-Weld™ (EC-9323) para obter propriedades mecânicas que possam ser usadas nas simulações numéricas de estruturas coladas. Com esse propósito, foram realizados quatro tipos de testes: i. testes de tracção, ii. testes de corte TAST (thick adherend shear test), iii. testes de corte DCB (double cantilever beam test) e iv. ensaios de flexão com entalhe no extremo (ENF). Adicionalmente, a resistência ao corte e ao descolamento de ligações adesivas compósito-compósito foram caracterizadas experimentalmente. Diferentes combinações de compósitos foram utilizando o adesivo epóxi 3M™ Scotch-Weld™ (EC-9323). Por fim, uma investigação numérica foi iniciada, que, de momento, está em estado embrionário e requer aprofundamento em estudos futuros. Os resultados dos testes caracterizaram eficazmente o adesivo, proporcionando uma compreensão abrangente da resistência de colagem e resistência ao descolamento em uniões compósito-compósito. Em conclusão, os resultados obtidos neste estudo sobre uniões adesivas de compósitos de carbono sublinham a importância da seleção de materiais, processos de fabrico e tratamentos de superfície para alcançar as propriedades mecânicas e de fratura desejadas em uniões adesivas.

**PALAVRAS-CHAVE:** Materiais compósitos; Ligações adesiva; Ligações compósito-compósito; Ensaios experimentais; Simulação numérica.

# Mechanical performance of adhesively bonded innovative aeronautic carbon composites

## ABSTRACT

The aviation sector is under growing pressure to enhance eco-efficiency due to air travel's impact on global carbon emissions. This has prompted a shift towards lighter materials and technologies to reduce CO<sub>2</sub>, NO<sub>x</sub> emissions, and noise. Composite materials are at the forefront of this movement, replacing traditional aluminium high-performance aircraft structures. Compared to metals, composites offer significant weight advantages, resulting in lower fuel consumption and improved aircraft performance. However, attaching composites with mechanical fasteners like bolts and rivets can increase structural weight. Adhesive bonding emerges as a potential solution, offering weight savings without compromising strength. Challenges persist in designing adhesively bonded joints for composites, requiring extensive testing to determine joint strength.

The present thesis aimed to investigate adhesive joints between carbon composite materials. The study involved experimental characterisation of 3M™ Scotch-Weld™ (EC-9323) epoxy adhesive to obtain mechanical properties that can be further used for the numerical simulation of bonded structures. With this purpose, four tests were performed: i. bulk tensile test, ii. thick adherend shear test (TAST), iii. double cantilever beam test (DCB), and iv. end-notched flexure (ENF). Additionally, the single-lap shear bond and peel strengths of composite-to-composite adhesive joints were experimentally characterised. Various combinations of composites were bonded using 3M™ Scotch-Weld™ (EC-9323) epoxy adhesive. Finally, a numerical study has been initiated; however, it remains in its preliminary stages, necessitating more improvement through future research. The test results effectively characterised the adhesive, offering a comprehensive understanding of bond strength and peel resistance in composite-to-composite joints. In conclusion, the results obtained in this study of adhesive carbon composite joints highlight the importance of material selection, manufacturing processes, and surface treatments in achieving adhesive joints' desired mechanical and fracture properties.

**KEYWORDS:** Composite materials; Adhesive bonding; Composite-to-composite joints; Experimental testing; Numerical simulation.

# TABLE OF CONTENTS

Acknowledgements .....	III
Resumo .....	IV
Abstract .....	V
Table of Contents .....	VI
List of Figures .....	VIII
List of Tables .....	X
List of Abbreviations and Symbols .....	XI
1. Introduction .....	1
1.1. Scope of the thesis .....	1
1.2. GAVIÃO project .....	2
1.3. Objectives and organisation of the thesis .....	2
2. State of the art .....	5
2.1. Composite materials and manufacturing processes .....	5
2.2. Adhesively bonded composites .....	6
2.3. Adhesive characterisation methods .....	8
2.4. Cohesive zone modelling .....	9
3. Experimental program .....	13
3.1. Manufacturing processes .....	13
3.1.1. Heated vacuum-assisted resin transfer moulding (heated-VARTM) .....	13
3.1.2. Stamping .....	16
3.2. Raw and composite materials .....	18
3.3. Adhesive and adhesive joints characterisation .....	22
3.3.1. Tensile test .....	24
3.3.2. Thick adherend shear test .....	26
3.3.3. Double cantilever beam test .....	30
3.3.4. End-notched flexure test .....	40
3.3.5. Single-lap joints test .....	48
3.3.6. Floating roller peel test .....	50



4.	Experimental results .....	57
4.1.	Tensile test .....	57
4.2.	Thick adherend shear test .....	58
4.3.	Double cantilever beam test .....	60
4.4.	End-notched flexure.....	65
4.5.	Single-lap joints test .....	68
4.6.	Floating roller peel test.....	72
5.	Numerical study .....	77
5.1.	Single lap joint .....	77
5.1.1.	Modelling strategy .....	77
5.2.	Subcomponent model .....	78
5.2.1.	Test setup.....	79
5.2.2.	Materials definition.....	81
5.2.3.	Boundary condition .....	82
5.2.4.	Mesh .....	83
5.3.	Numerical results.....	84
6.	Conclusions and further developments.....	87
6.1.	Main conclusions .....	87
6.2.	Further developments .....	90

## LIST OF FIGURES

<b>Figure 2.1:</b> Bilinear cohesive law available in ABAQUS. ....	11
<b>Figure 3.1:</b> Heated VARTM process [35]. ....	14
<b>Figure 3.2:</b> Manufactured part using heated-VARTM process. ....	16
<b>Figure 3.3:</b> Thermoset Hot Press process [35]. ....	17
<b>Figure 3.4:</b> Thermoplastic Hot Stamping process [35]. ....	18
<b>Figure 3.5:</b> HiMax® fabric sequence of layers [36]. ....	19
<b>Figure 3.6:</b> A 3M™ Scotch-Weld™ (EC-9323) adhesive ....	22
<b>Figure 3.7:</b> Bulk tensile specimen dimensions [mm]. ....	24
<b>Figure 3.8:</b> Moulds. ....	24
<b>Figure 3.9:</b> Application of the adhesive. ....	25
<b>Figure 3.10:</b> Universal-joint device. ....	27
<b>Figure 3.11:</b> (a) manufacturing of the specimen and (b) detail of TAST specimen. ....	28
<b>Figure 3.12:</b> TAST setup. ....	29
<b>Figure 3.13:</b> Double cantilever beam specimen. ....	30
<b>Figure 3.14:</b> Test panel. ....	31
<b>Figure 3.15:</b> Specimen manufacturing (adhesive application). ....	32
<b>Figure 3.16:</b> Procedure for the measurement of adhesive thickness. ....	33
<b>Figure 3.17:</b> Surfaces after preparation. ....	34
<b>Figure 3.18:</b> Hinges adhesion. ....	34
<b>Figure 3.19:</b> Pre-crack length [43]. ....	35
<b>Figure 3.20:</b> Setup of the DCB test. ....	36
<b>Figure 3.21:</b> Load displacement trace from DCB test [43] . ....	37
<b>Figure 3.22:</b> Compliance calibration [43]. ....	38
<b>Figure 3.23:</b> Modified beam theory [43]. ....	39
<b>Figure 3.24:</b> Modified Compliance Calibration [43]. ....	39
<b>Figure 3.25:</b> ENF specimen, Fixture, and Dimensions [45]. ....	41
<b>Figure 3.26:</b> Composite panel. ....	42
<b>Figure 3.27:</b> Compliance calibration markings on the ENF specimen. ....	44
<b>Figure 3.28:</b> PC Markings [45]. ....	46
<b>Figure 3.29:</b> Illustration of Compliance and Maximum Load Point Determination [45]. ....	47

<b>Figure 3.30:</b> SLJ Specimen.....	49
<b>Figure 3.31:</b> Testing setup.....	50
<b>Figure 3.32:</b> Example of flexible and rigid adherends.....	51
<b>Figure 3.33:</b> Pressure application.....	52
<b>Figure 3.34:</b> Floating roller peel test specimen configurations.....	52
<b>Figure 3.35:</b> Unbounded area.....	53
<b>Figure 3.36:</b> Specimens after cutting.....	54
<b>Figure 3.37:</b> Testing setup.....	55
<b>Figure 4.1:</b> Stress-strain curves of bulk specimen (3M™ Scotch-Weld™).....	57
<b>Figure 4.2:</b> (a) Failure surface with void and (b) Smooth failure surface.....	58
<b>Figure 4.3:</b> Stress-strain curves of the TAST specimens.....	59
<b>Figure 4.4:</b> Adhesive failure of a TAST specimen after testing.....	59
<b>Figure 4.5:</b> a representative Force-Displacement curves of DCB testing.....	61
<b>Figure 4.6:</b> E-Modulus during crack propagation.....	62
<b>Figure 4.7:</b> R-curves of a representative DCB specimen by CCM, CBT and ECM.....	63
<b>Figure 4.8:</b> Representative DCB specimens after testing (a: Heated VARTM, b: Thermoset hot press and c, Thermoplastic hot stamping).....	64
<b>Figure 4.9:</b> Load-Displacement curves of the ENF specimens.....	66
<b>Figure 4.10:</b> Adhesive failure of Thermoplastic specimen.....	68
<b>Figure 4.11:</b> Failure modes of SLJ specimens.....	72
<b>Figure 4.12:</b> Experimental Pb curves for each configuration.....	73
<b>Figure 5.1:</b> Detail of the mesh for the model.....	78
<b>Figure 5.2:</b> Boundary conditions.....	78
<b>Figure 5.3:</b> Test Specimen (CFRP part).....	79
<b>Figure 5.4:</b> Representation of the test fixtures tight to the Frame and Skin/Stringers and load application point.....	81
<b>Figure 5.5:</b> Frame Material orientation.....	82
<b>Figure 5.6:</b> Boundary condition and constraint applied to the panel.....	83
<b>Figure 5.7:</b> Detail of the mesh.....	84
<b>Figure 5.8:</b> Reaction forces and the imposed load.....	84
<b>Figure 5.9:</b> Hashin damage criterion.....	85
<b>Figure 5.10:</b> Stress Distribution.....	85

# LIST OF TABLES

**Table 3.1:** Stacking sequences. .... 20

**Table 3.2:** List of the standard used in the experimental program. .... 23

**Table 3.3:** tests combinations. .... 23

**Table 3.5:** Test's dimensions. .... 42

**Table 4.1:** Tensile mechanical properties. .... 58

**Table 4.2:** Shear mechanical properties. .... 60

**Table 4.3:** Non-precracked and precracked interlaminar fracture toughness in mode I. .... 65

**Table 4.4:** Non-precracked and precracked interlaminar fracture toughness in mode II. .... 67

**Table 4.5:** Single lap joint test results. .... 69

**Table 4.6:** Floating roller test results ..... 74

# LIST OF ABBREVIATIONS AND SYMBOLS

## Abbreviations

DCB	Double cantilever beam
BTT	Bulk tensile test
ENF	End-notched flexure
TAST	Thick adherend shear test
BTT	European Committee for Standardization
NO <sub>x</sub>	Nitrogen oxides
CFRP	Carbon Fibre Reinforced Polymer
CZM	Cohesive zone model
CO <sub>2</sub>	Carbon Dioxide
AoO	Out-of-Autoclave
VARTM	Vacuum-assisted resin transfer moulding
SLJ	Single lap joint
NPC	Non-precracked
PC	Precracked
ASTM	American Society for Testing and Materials
ELS	End-loaded split
4ENF	Four-point end-notched flexure
UD	Unidirectional
ISO	International Organization for Standardization
PTFE	Polytetrafluoroethylene
DIC	Digital image correlation
MBT	Modified beam theory
MCC	Modified compliance calibration
CCM	Compliance Calibration Method
FT	Fracture Test
CC	Compliance calibration
CCM	Compliance Calibration Method
FT	Fracture Test

## Symbols

$E$	Elastic modulus of the adhesive
$G$	Ultimate strain of the adhesive
$\sigma_f$	Elastic modulus of the CFRP laminate
$\tau_f$	Ultimate strain of the CFRP laminate
$G_{Ic}$	Fracture toughness in mode I
$G_{IIc}$	Fracture toughness in mode II
$\delta_i$	Opening displacement
$t_n$	Cohesive strength in tension
$t_s$	cohesive strength in shear (direction 2)
$t_t$	cohesive strength in shear (direction2)
$K_{coh}$	stiffness matrix
$\langle \rangle$	Macaulay brackets
$\varepsilon_f$	Failure strain
$\nu$	Poisson's ratio
$C_i$	Compliance
$\Delta$	Crack correction
$a$	Crack length
$G_Q$	Candidate toughness
$P$	Force

# 1. INTRODUCTION

## 1.1. Scope of the thesis

The aviation industry is increasingly pressed to improve its eco-efficiency due to the significant contribution of air travel to global carbon emissions. Consequently, there is a robust shift towards the development of lightweight materials and technologies with an aim to mitigate CO<sub>2</sub>, NO<sub>x</sub> emissions, and noise.

In this landscape, composite materials have emerged as a frontrunner for next-gen aircraft. These materials are gradually superseding conventional aluminium in high-performance aeronautical structures, especially where there's an imperative for weight savings without compromising on the ability to bear high loads. When compared to traditional metallic counterparts, composites offer a pronounced weight advantage. This reduction in weight directly correlates to decreased fuel consumption, consequently augmenting aircraft performance [1].

Yet, there are challenges. Traditional composite assembly methods using mechanical fasteners like bolts and rivets can inadvertently augment structural weight. This is primarily because the regions punctuated with holes (which disrupt the fibres) necessitate thicker laminates to maintain structural integrity [2]. Besides, bolted connections promote high stress concentration and corrosion in metallic parts, and potential damage to the composite structure through drilling holes, which could introduce delamination [3].

Adhesively bonded connections are a potential game-changer that promises weight savings without diminishing mechanical properties [4]. This technique offers advantages especially when coupling composite aerostructures: contribution to lower structural weight, reduction of manufacturing costs, and high fatigue strength with low stress concentration in the adherents by the distribution of stresses throughout a large surface [5]. Additionally, adhesive connections do not suffer from corrosion and do not disrupt the continuity of reinforcing fibres.

The realm of adhesively bonded joints for composite materials is still evolving. Reliable analytical methods remain elusive [6], necessitating extensive testing on representative specimens to ascertain joint strength. Besides, adhesive connections have also their limitations. They exhibit less resistance to environmental

conditions, the presence of moisture in adhesive joints may weaken the adhesive's physical and chemical properties and the interface between the adhesive and the substrate [6] and require stringent quality control during manufacturing.

## 1.2. GAVIÃO project

The work developed in the context of this thesis was carried out based on the ongoing work in the Gavião Project (Research and Development of Technologies for Large-Scale Aircraft Component Production).

The Gavião project aims to globally promote the use of composite materials in new, large-scale aeronautical structures. The intention is for these structures to exhibit a high level of component integration. The project will pave the way for new eco-efficient Out-of-Autoclave (OoA) manufacturing and assembly technologies, such as heated vacuum-assisted resin transfer moulding and thermo-stamping. Additionally, it aims to produce a full-scale demonstrator of a regional aircraft fuselage section using the newly developed manufacturing processes. The GAVIÃO Project is being developed by a consortium consisting of OPTIMAL Structural Solutions, ISQ, and INEGI.

The work developed in this thesis contributes to increasing the knowledge about the performance of the adhesive bond between the different composite materials that are being developed in the project and that will be integrated into the final demonstrator.

## 1.3. Objectives and organisation of the thesis

This present thesis aims to investigate adhesive joints between carbon composite materials. Three types of innovative carbon composites were manufactured according to heated vacuum-assisted resin transfer moulding (heated-VARTM) and two variations of stamping: thermoset hot press and thermoplastic hot stamping. The study involves experimental characterisation to obtain mechanical properties that can be further used for the numerical simulation of bonded structures. With this purpose, four tests were performed: i. bulk tensile test (BTT), ii. thick adherend shear test (TAST), iii. double-cantilever beam (DCB), and iv. end-notched flexure (ENF).

Additionally, the single-lap shear bond and the peel strengths of composite-to-composite adhesive joints were experimental and numerically characterised.

Lastly, numerical procedure for the skin–stringer debonding simulation was also developed.



The methodology used to pursue this objective is structured as follows. The thesis is divided in four chapters: Introduction, state of the art, experimental program, and experimental results.

The first chapter describes the scope of the thesis and the main objectives of the thesis.

The second chapter provides an overview of composites in the context of the aerospace industry, focusing on their classification, types, and manufacturing methods. It begins by classifying composites into thermoset and thermoplastic based on their polymeric matrix. It highlights the distinctive characteristics of each type, emphasising the rising importance of thermoplastic composites due to their unique properties and environmental benefits. Also, it gives an overview of the drawbacks of autoclave manufacturing for aerostructures, prompting the exploration of out-of-autoclave (OoA) solutions. Furthermore, it discusses the importance of bond-line thickness in the fracture behaviour of bonded joints. Also, it presents the different existing methods to characterise adhesives and bond strength. Finally, it oversees the cohesive modelling approach to simulate adhesive joints.

The third chapter describes the experimental program. It starts by describing the manufacturing methods used to fabricate the composite laminates used to manufacture the specimens. Secondly, it describes each test performed in this experimental campaign, including the standard adopted, the procedure followed, and the data reduction methods used to analyse the final results.

The fourth chapter focuses on presenting and analysing the experimental results obtained from the conducted tests. The data collected from the experimental program outlined in the previous chapter are comprehensively examined and discussed. The results include a detailed analysis of the mechanical properties of the adhesive and the bond strength of adhesive joints. Chapter five provides a detailed description of the numerical work conducted in this thesis.

The thesis is concluded in Chapter six with an overall assessment of its achievements and a discussion of possible avenues for future developments.

THIS PAGE WAS INTENTIONALLY LEFT BLANK

## 2. STATE OF THE ART

### 2.1. Composite materials and manufacturing processes

Composites can be categorized into two types based on the polymeric matrix: thermoset or thermoplastic. The defining characteristic of thermosetting composites is that they do not soften or melt during heating cycles and are completely cross-linked, meaning that polymer chains are linked together by a series of bonds. In contrast, thermoplastic composites can go through numerous heating and cooling cycles and have minimal cross-linking, which makes them appropriate for recycling because they can be reshaped and reformed repeatedly [7], [8]. Although thermosets currently have a larger presence in the composites market, their numerous drawbacks have led to an increased focus on thermoplastic composites. There are still many open questions regarding thermoplastics but, when compared to their thermoset counterparts, their unique physical, thermal, and electrical properties can potentially introduce cost savings due to non-heated tooling, shorter manufacturing cycle times, enhanced mechanical properties, chemical and environmental resistance, and the potential to be recycled by recovering and reusing composite material from a used component [9].

Currently, almost all aerostructures include components produced using composite materials. Although these materials were introduced in aeronautical structures in the 1950s, they have only recently become a major part of aircraft, as seen in the Boeing 787 Dreamliner [10]. With growing environmental concerns and the need to replace current metal alloys, composite materials, particularly thermosets, have gained significant relevance in the aeronautic industry. The fibre material is usually carbon. Their potential for weight reduction can lead to lower fuel consumption and reduced operational emissions.

However, the practical limitation of autoclave manufacturing, which is the predominant method for aeronautic composite structures, raises questions about the viability of composite materials. The autoclave processes involve high cycle times, capital costs, and tooling expenses. Additionally, the dimensions of autoclaves directly impact production capacity, restricting the feasibility of large component manufacturing [11].

In light of the increasing demand and production of aircraft, it has become crucial to explore out-of-autoclave (OoA) solutions that offer lower costs, reduced cycle times, and improved environmental

friendliness. In the past, OoA solutions were disregarded due to inferior material quality compared to autoclave-produced materials. However, the new generation of OoA processes is gaining acceptance as they now offer the possibility of achieving composite materials with equivalent autoclave quality [12]. These processes utilize vacuum, pressure, and heat outside of the autoclave to manufacture composites. In the scope of present thesis, two OoA manufacturing are explored to manufacture the composite materials: i. heated vacuum-assisted resin transfer moulding (heated-VARTM) (also known as vacuum infusion) and ii. stamping. These processes offer alternatives to traditional autoclave-based methods, providing unique advantages and enabling the production of high-quality composite materials for aerospace applications. Each technique involves specific procedures and equipment to create composite laminates with unique properties (see more details in Chapter “ Experimental program “). Two variations of stamping were explored.

Vacuum-assisted resin transfer moulding (VARTM) is one of the most robust and attractive replacements for autoclave processes. VARTM is a closed mould process that places dry reinforcements into a mould, seals them with a sealed flexible membrane (vacuum bag) and then, using differential pressure, injects resin to infuse and impregnate the dry fibres. The process can occur at ambient or elevated temperatures, depending on the selected resin system. In contrast, to autoclave processes, this method offers several advantages. It is capable of processing low-cost composites with complex shapes, resulting in excellent properties and a good surface finish. In the present thesis is explored an innovative heated-VARTM to process high-temperature mono-component epoxy resins, which due to their high viscosity cannot be used in conventional VARTM.

Stamping has been also seen as very promisor manufacturing process. In this process, thermoset or thermoplastic prepregs are heated and stamped to form a composite structure. The mould then shapes the composite to the desired shape of the component. Stamping stands out from autoclave processes due to its ability to effectively eliminate voids and improve interlaminar bonding in a short amount of time, often in the order of seconds, and with low energy consumption. This makes it a cost-effective method capable of producing large volumes[13], [14].

## **2.2. Adhesively bonded composites**

Adhesively bonded composites have emerged as a cutting-edge approach to materials engineering and design, key in diverse industries such as aerospace, automotive, and construction. Adhesive bonding has proven to be a fitting technology for achieving the desired balance of weight reduction and mechanical

performance. However, traditional joint topologies such as single overlap joints induce high peel stresses, resulting in sudden failure and low joint strength compared to metal adherends [2]. Various parameters can influence the strength of adhesively bonded joints, and understanding these factors is crucial for achieving strong and reliable bonds. Some key parameters affecting adhesive bond strength include surface preparation, adhesive selection, adhesive cure conditions, joint design, and adhesive thickness.

The bond-line thickness plays a prominent role in the fracture behaviour of bonded joints. Therefore, understanding this behaviour is critical for optimising the thickness of the adhesive layer in bonded joints in such applications. The general observation in the literature is that the critical energy release rate is highly affected by the bond-line thickness, which is explained by the physical constrain applied by the adherents. In a thin adhesive layer, these constraints prevent the full development of the fracture process zone. Consequently, the value of the fracture energy decreased. However, in a thick adhesive layer, the effect of this constraint is lower; as a result, the fracture process zone will be fully developed, which leads to a higher value of the fracture energy.

Banea *et al.* [15] studied the effect of a Polyurethane adhesive thickness layer varying from 0.2 to 2 mm using a double cantilever beam (DCB). The obtained result shows a linear fracture energy increase when the thickness increases from 0.2 to 1 mm. This is explained by the ability of the adhesive to generate a plastic zone before the propagation of the crack. On the other hand, between a thickness of 1mm and 2mm, there is a slight decrease in fracture energy due to the amount of defect a thick adhesive layer contains. A similar study was conducted by Marzi *et al.* [16], using 31 specimens with five different nominal thicknesses ( $t=0.2, 0.5, 1, 2, \text{ and } 4$  mm). In general, the result demonstrates an increase in the fracture energy with increasing the adhesive layer thickness. Furthermore, the crack propagates with constant fracture energy in the case of 0.2 mm and 0.5 mm, while it decreases during the propagation of the crack in the case of the 1mm adhesive layer. However, it increases in the case of 2mm and 4mm.

Five different thicknesses were tested by Lopes Fernandes *et al.* [17] (0.4, 1.1, 2.6, 4.1, and 10.1mm); these thicknesses were selected for maritime application. Contrary to most studies, the fracture energy was the same for the first three thicknesses. The author explained these findings by pointing out that the failure surface was smoother in the case of a thicker bond line, and the change on the crack path plane might prevent the formation of the fracture process zone. In the case of 4.1mm bond-line thickness, the fracture energy increased because the adherend constrains is smaller than 2.6 mm. Carlberger *et al.* [18] investigates the influence of the change in the thickness from 0.1 mm up to 1mm on the fracture energy. The fracture energy increases monotonically up to 1 mm in thickness, after which it decreases

at 1.6mm, indicating that a maximum exists between 1 mm and 1.6 mm. Another interesting finding is that the fracture energy reaches a maximum for a bond line equal to the diameter of the fracture process zone.

The result obtained by Cooper *et al.* [19] showed an increase in the fracture energy when increasing the bond thickness from 0.25mm to 1.3mm and remained constant for thicker bond thickness, which following previous work, i.e., fracture energy increased until the diameter of the plastic zone under plain strain condition, reaches the bond thickness.

[20] concluded that both the adherend and the bond line thicknesses have been shown to impact the adhesive joint's fracture toughness significantly. The trend observed is that thinner specimens result in higher fracture toughnesses for both modes I and II. Similarly, thicker adhesive layers also result in higher bond toughness.

### 2.3. Adhesive characterisation methods

Peel and shear loads are the main loads acting on an adhesive joint. However, the determination of the adhesive's elastic modulus  $E$ , shear modulus  $G$ , tensile failure stress  $\sigma_f$ , and the shear failure stress  $\tau_f$  are insufficient for accurately predicting joint behaviour [21]. Advanced modelling techniques like cohesive zone modelling (CZM) require additional information, specifically, the values of fracture toughness in mode I,  $G_{Ic}$ , and mode II,  $G_{IIc}$ . These parameters are crucial in comprehensive modelling, enabling more accurate predictions and analysis of adhesive joint performance.

Several experimental methods are available to characterise adhesives, each providing specific information regarding their mechanical properties. Tensile, shear, and peel tests are commonly employed to assess the adhesive's properties. There are two main categories of tests to estimate the tensile properties of an adhesive: i. those using bulk adhesive specimens and ii. adhesive joint tests. The adhesive joint configuration is the most used method for determining tensile properties, but there is also the option of using tensile bulk tests [21].

Shear tests for adhesives also can be categorised into bulk and adhesive joint tests. In adhesive joint tests, accurately measuring the small adhesive shear displacement is challenging. On the other hand, bulk specimens provide more precise results due to their higher length. However, the size and thickness of bulk specimens may not accurately represent the adhesive properties within a joint. Several tests are commonly employed to characterise the shear properties of adhesives, such as the notched beam shear

method (Iosipescu), the notched plate shear method (Arcan), torsion of bulk material, butt torsion (napkin ring or solid specimen), and (TAST) method [6], [21], [21].

TAST uses two thick adherends to decrease peel stress and provide a pure shear stress state in the adhesive layer [22]. This method was used by Banea *et al.* [23] to characterise two different adhesive types: a polyurethane and a high-temperature thixotropic adhesive sealant. The TAST procedure is described in the standard ISO 11003-2001 [24].

The typical test used to determine  $G_{Ic}$  is the DCD as described in ASTM D5528/D5528M – 21 and the tapered double-cantilever Beam (TDCB) [25]. Additionally, for determining  $G_{IIc}$ , the typical tests employed are the (ENF), the end-loaded split (ELS), and the four-point end-notched flexure (4ENF). Among these tests, the ENF described in the standard ASTM D7905/D7905M – 19 is the simplest and most widely used for the shear characterisation of adhesive joints. According to the literature, the DCB and ENF tests are considered reliable methods for obtaining  $G_{Ic}$  and  $G_{IIc}$  of adhesive joints, respectively.

## 2.4. Cohesive zone modelling

Cohesive zone models (CZM) predict the adhesive joint's strength and simulate damage growth in structures. It has many advantages over other methods (VCCT and XFEM), such as its capacity to simulate the onset and non-self-similar damage growth and not require an initial crack [26]. In CZM the entire fracture process is lumped into the crack plane, and it is characterised by a cohesive law which associates traction and displacement jumps across the cohesive surface. With separation increasing, the traction increases reach maximum stress (cohesive strength or interface strength), then, governed by a softening curve, decreases, and eventually vanishes, allowing for traction-free crack surface creation [27].

The CZM laws are used to connect superimposed nodes of elements representing different materials to simulate a zero-thickness interface, or they can be applied directly between two non-contacting materials to simulate a thin strip of finite thickness between them, e.g., to simulate an adhesive bond. The cohesive zone model defines the relationship between the traction in the cohesion zone and the opening displacement of the interface. The Equation (2.1) describes the constitutive law [28]:

$$\begin{pmatrix} t_n \\ t_s \\ t_t \end{pmatrix} = \begin{bmatrix} K_n & 0 & 0 \\ 0 & K_s & 0 \\ 0 & 0 & K_t \end{bmatrix} \begin{pmatrix} \delta_n \\ \delta_s \\ \delta_t \end{pmatrix} = K_{coh} \delta \quad (2.1)$$

Where  $t_n$  is the cohesive strength in tension,  $t_s$  and  $t_t$  are the cohesive strength in shear in direction 2 and 3.,  $\delta_i$  is the opening displacement,  $K_{coh}$  is the stiffness matrix containing the adhesive bond parameter  $K_n$ ,  $K_s$  and  $K_t$  [29]. The definition of these parameters depends on whether the continuum or the local approach is used. In the local approach, the  $K_{coh}$  parameters are chosen to avoid any interference between the cohesive element deformation and the deformation of the structure. In the continuum approach,  $K_n = E$  and  $K_s = G$  [30]. Also, according to [28], the stiffness matrix component in the normal direction can be calculated as the ratio of the normal modulus to adhesive thickness  $K_n = E/t_A$ . Meanwhile, the stiffness matrix components in shear are the ratio of the shear modulus to adhesive thickness  $K_s = G/t_A$ . As an approximation, the tension cohesive strength ( $t_n^0$ ) and the shear cohesive strength ( $t_s^0$ ) could initially be considered as the tensile strength ( $\sigma_f$ ) and the shear strength ( $\tau_f$ ), respectively. The final cohesive law is found by iteratively fitting the experimental and numerical P- $\delta$  curves up to the best possible match [31].

After the elastic part, damage initiation starts, and it can be specified by different criteria: maximum nominal stress criterion (equation (2.2)), maximum nominal strain criterion (equation (2.3)), quadratic nominal stress criterion (equation (2.4)), and quadratic nominal strain criterion (equation (2.5)).

$$\max \left\{ \frac{\langle t_n \rangle}{t_n^0}; \frac{t_s}{t_s^0}; \frac{t_t}{t_t^0} \right\} = 1 \quad (2.2)$$

$$\max \left\{ \frac{\langle \varepsilon_n \rangle}{\varepsilon_n^0}; \frac{\varepsilon_s}{\varepsilon_s^0}; \frac{\varepsilon_t}{\varepsilon_t^0} \right\} = 1 \quad (2.3)$$

$$\left\{ \frac{\langle t_n \rangle}{t_n^0} \right\}^2 + \left\{ \frac{t_s}{t_s^0} \right\}^2 + \left\{ \frac{t_t}{t_t^0} \right\}^2 = 1 \quad (2.4)$$

$$\left\{ \frac{\langle \varepsilon_n \rangle}{\varepsilon_n^0} \right\}^2 + \left\{ \frac{\varepsilon_s}{\varepsilon_s^0} \right\}^2 + \left\{ \frac{\varepsilon_t}{\varepsilon_t^0} \right\}^2 = 1 \quad (2.5)$$

Where " $\langle \rangle$ " are the Macaulay brackets meaning that a compressive stress state does not initiate damage [32]. The damage triggers for the maximum nominal criterion when the maximum nominal stress ratio or the maximum nominal strain ratio reaches one. On the other hand, the damage starts when a quadratic interaction function involving the nominal stress ratios or the nominal strain ratios reaches one. After the crack initiation, softening occurs in the material. The softening process is described by introducing the damage variable  $d$ . The value of  $d$  ranges from 0 during the elastic portion of the CZM law to 1 at the end of the softening process. When damage occurs, traction and shear can be either



coupled or uncoupled during the damage propagation. This is achieved by setting the non-diagonal terms of the stiffness matrix to zero [33].

$$t_n = \begin{cases} (1-d)\bar{t}_n \\ \bar{t}_n \end{cases} \quad (2.6)$$

$$t_s = (1-d)\bar{t}_s \quad (2.7)$$

$$t_t = (1-d)\bar{t}_t \quad (2.8)$$

Where  $\bar{t}_n$ ,  $\bar{t}_s$  and  $\bar{t}_t$  are the stress components predicted by the elastic traction-separation behaviour for the current strains without damage. The typical traction-separation response of cohesive laws is bilinear (as shown in Figure 2.1), exponential, or trapezoidal. It depends on the nature of the adhesive used, whether it is brittle or ductile [34].

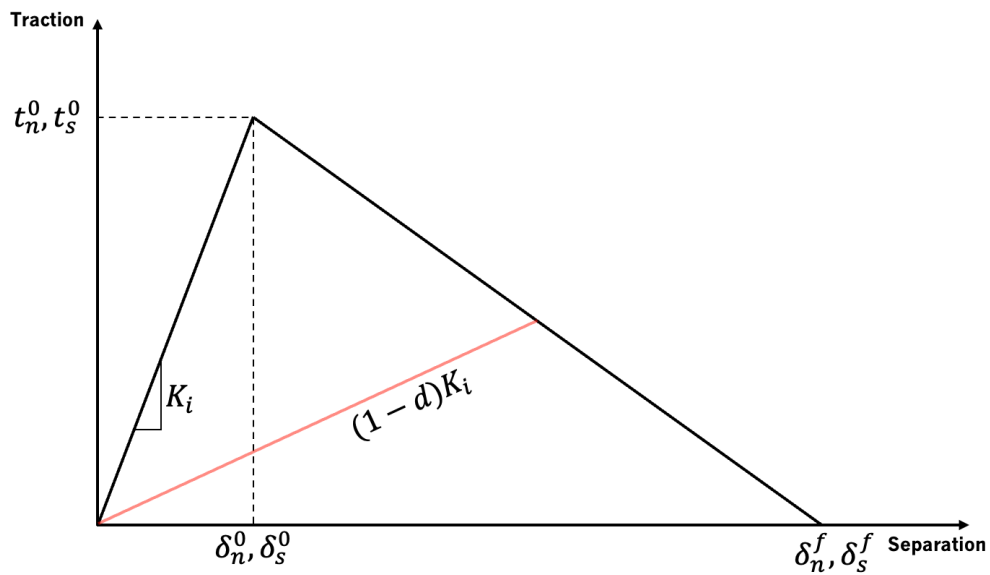


**Figure 2.1:** Bilinear cohesive law available in ABAQUS.

THIS PAGE WAS INTENTIONALLY LEFT BLANK

## 3. EXPERIMENTAL PROGRAM

### 3.1. Manufacturing processes

In the present work, three types of carbon composites were manufactured by INGEI and OPTIMAL according to heated vacuum-assisted resin transfer moulding (heated-VARTM) and two variations of stamping: thermoset hot press and thermoplastic hot stamping, as described in the following subsections.

#### 3.1.1. *Heated vacuum-assisted resin transfer moulding (heated-VARTM)*

Vacuum-assisted resin transfer moulding process usually involves special equipment such as mould, vacuum pots, vacuum pump, vacuum bag, Flow mesh, Peel plies, sealant tape, temperature control system, inlet and outlet hoses, and control units and data acquisition. Furthermore, using aeronautic-grade resin necessitates a high-pressure and temperature control system to ensure high-quality components. This manufactured process, used in the present work, is known as heated-VARTM.

Manufacturing composite parts using a heated-VARTM process involves the next nine primary steps [35]:

- **Reinforcement cutting:** in this step, reinforcement fabric, peel-ply and flow mesh are cut according to the specific dimensions of the parts to be produced.
- **Resin preparation:** in this step, the resin is defrosted and heated according to the manufacturing indication. Normally, the resin comes in large containers with more product than needed for each vacuum infusion. Therefore, it is important to calculate the resin needed for each process and separate it into individual containers. This helps to avoid exposing the resin to multiple heating cycles. In addition to that, degasification is performed to remove all the air to avoid any risk of air bubbles inside the produced parts.
- **Mould cleaning:** it is crucial to ensure that the mould is free of contamination and dust and that the produced part can be removed easily. Three layers of mould cleaner are applied at 5-minute intervals between each layer to achieve a clean surface. After the surface is dry, three more layers of a mould release agent are applied at the same time intervals.

- Layup:** reinforcement layers are placed according to the stacking sequence. Subsequently, a layer of peel-ply and flow mesh is added to complete the stacking process, as illustrated in Figure 3.1. Peel-ply is used to facilitate removing the part from the mould, and flow helps the resin flow throughout the reinforcement due to its high permeability. After placing the resin inlet and outlet of the mould, the vacuum bag is placed on top; it is essential to mention that its dimension should be bigger than the part to avoid any possible damage due to the tension inside the mould.

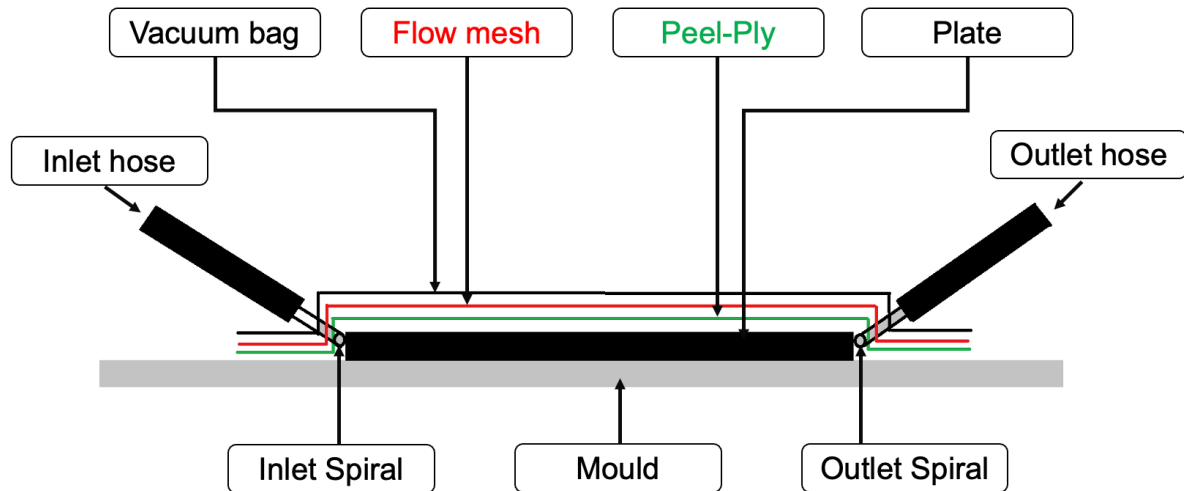


**Figure 3.1:** Heated VARTM process [35].

- Leak test:** the procedure consists of several steps to ensure the integrity of the vacuum bag and obtain high-quality parts in the vacuum infusion process. The first step is the initial leak test. At room temperature, a vacuum pressure of 700 mbar is applied to the mould. Pressure data inside the vacuum bag is collected for 10 minutes. If the pressure drop exceeds 20 mbar during this period, it indicates a potential leak in the vacuum bag. In such a case, the bag needs to be inspected for leaks. If a solution cannot be found, the bag should be removed and replaced with a new one.
- Debulking:** which involves cycling the pressure inside the vacuum bag at 950 mbar. This process helps eliminate significant porosity between the fabrics, leading to better-quality parts. Following debulking, a second leak test is performed. The mould is heated to the temperature required for the vacuum infusion process (120 °C). After the resin's degasification, the final leak test is conducted before the infusion begins. A vacuum of 700 mbar is applied to the mould while it remains at 120 °C. Pressure data inside the vacuum bag is again collected for 10 minutes. If the pressure drop exceeds 20 mbar during this period, it indicates a possible leak in the vacuum

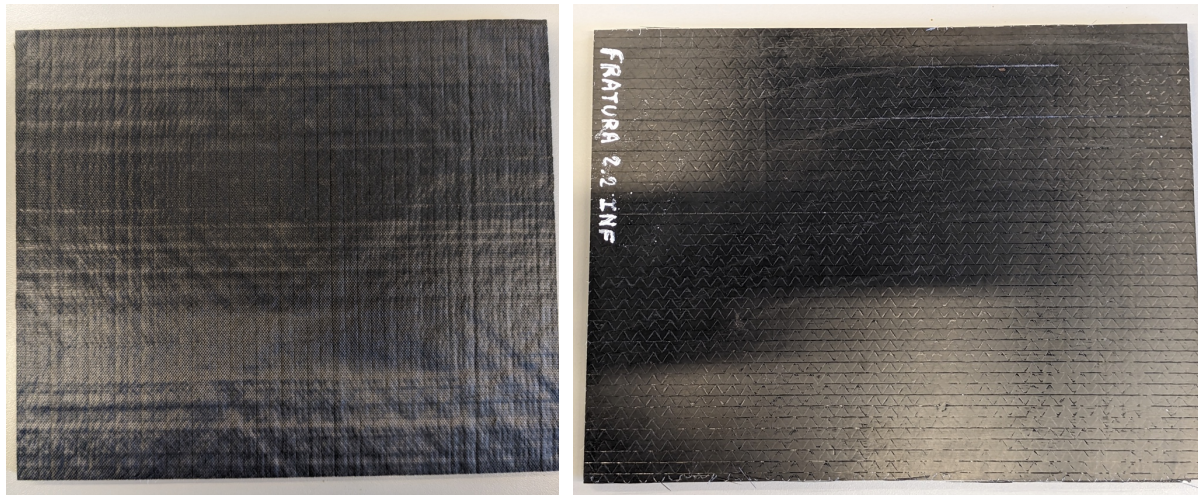
bag. In such cases, the bag should be inspected for leaks; if no solution is found, it must be replaced with a new one.

- **Resin impregnation:** once the leak test is done, the next step is impregnating the fibres with resin. This step is considered complete once the hose is fully filled with resin.
- **Curing:** the initial curing step involves increasing the mould temperature to the specified temperature in the resin's datasheet. This temperature increase is carried out in stages, with specific heating rates for each stage. In the first stage, the temperature is increased from 120°C to 150°C, with a heating rate of 3°C per minute. In the second stage, the temperature is increased from 150°C to 170°C, with a slightly slower heating rate of 2°C per minute. The third stage begins once the second stage is complete, where the temperature is raised from 170°C to 180°C at a rate of 1°C per minute. It is crucial to follow these heating rates to allow for proper thermal expansion and avoid potential damage to the mould or resin. After reaching the final temperature of 180°C, the temperature is maintained steady for 120 minutes. This maintenance period ensures that the resin undergoes the necessary curing process to achieve the desired properties and structural integrity.

By following these steps, the resin can effectively cure within the mould, resulting in a high-quality final product with the desired mechanical properties.

- **Demoulding:** is performed when the resin is completely cured and the material reaches room temperature.

Figure 3.2 shows a laminate produced using Heated-VARM method.



**a:** peel ply side

**b:** mould side

**Figure 3.2:** Manufactured part using heated-VARTM process.

### 3.1.2. Stamping

Thermoset hot press process, here described, has several benefits, including the ability to produce high-quality structural parts at a high rate, a fast-curing cycle, low energetic consumption, and it allows automation. However, it requires expensive custom-made tools with excellent heat transfer capabilities along the entire part contact surface, and the final quality depends on the mould design capacity. This process involves several stages.

Firstly, the laminate preparation phase consists of laying up multiple unidirectional prepreg or fabric sheets. Subsequently, the preform is created by shaping the stacked layers to achieve its nearly final shape. The preform is then carefully positioned within a heated mould and placed in a press. The mould ensures that the part conforms to the desired shape and undergoes complete curing and consolidation, resulting in a fully formed component with the intended characteristics. Finally, the mould is opened, and the demoulding process takes place, as illustrated in Figure 3.3.

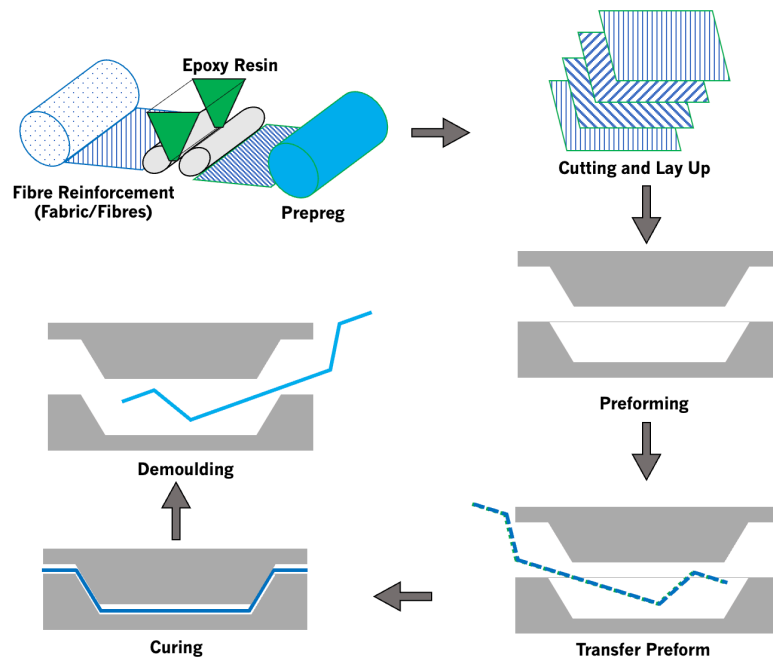


**Figure 3.3:** Thermoset Hot Press process [35].

At least, hot stamping process was also explored to manufacture composite in the context of the present work. This process, illustrated in Figure 3.4, involves several main steps:

- **Cutting and positioning the unidirectional tapes:** the prepreg tape is cut and positioned in this first step according to the stacking sequence. Ultrasonic spot welds maintain adhesion between layers. Automatic tape laying can be used to perform this procedure or manually by an operator. At the end of this step, a non-consolidated tailored layup is obtained.
- **Blank consolidation:** the second step involves consolidating the blank using a hot plate press. Controlled pressure and temperature are applied to the laminate during this step. The consolidation cycle requires a processing temperature above the material's melting point, and the cooling of the blank must be carefully controlled.
- **Mould preparation:** includes applying a cleaner followed by a release agent.
- **Blank heating:** after the mould preparation, the blank is secured onto the blank holder, which serves as a grip and transportation mechanism. The blank holder applies adjustable tension to the blank, ensuring a plane-stress state. Subsequently, the transport system moves the blank into an infrared oven, where heat is evenly applied to both sides of the blank. This elevated temperature surpasses the melting point of the matrix material, causing it to lose its stiffness.

- **Forming:** once the desired temperature is attained, the blank holder is directed towards the mould. Once it aligns with the mould correctly, the press applies defined pressure to shape the blank. It is essential to quickly transfer the blank to the press while maintaining its temperature. However, the transfer process must also be smoothly executed regarding acceleration at the start and end points to prevent any compromise in positioning. The quality of the final stamped part is directly influenced by the blank holding force, holding time and tool closing speed.
- **Cooling:** depending on the materials used, a cooling ramp may be applied; if it is not necessary, the mould is kept at room temperature.
- **Demoulding:** after finishing all processes, the manufactured component is extracted from the mould through the demoulding procedure.

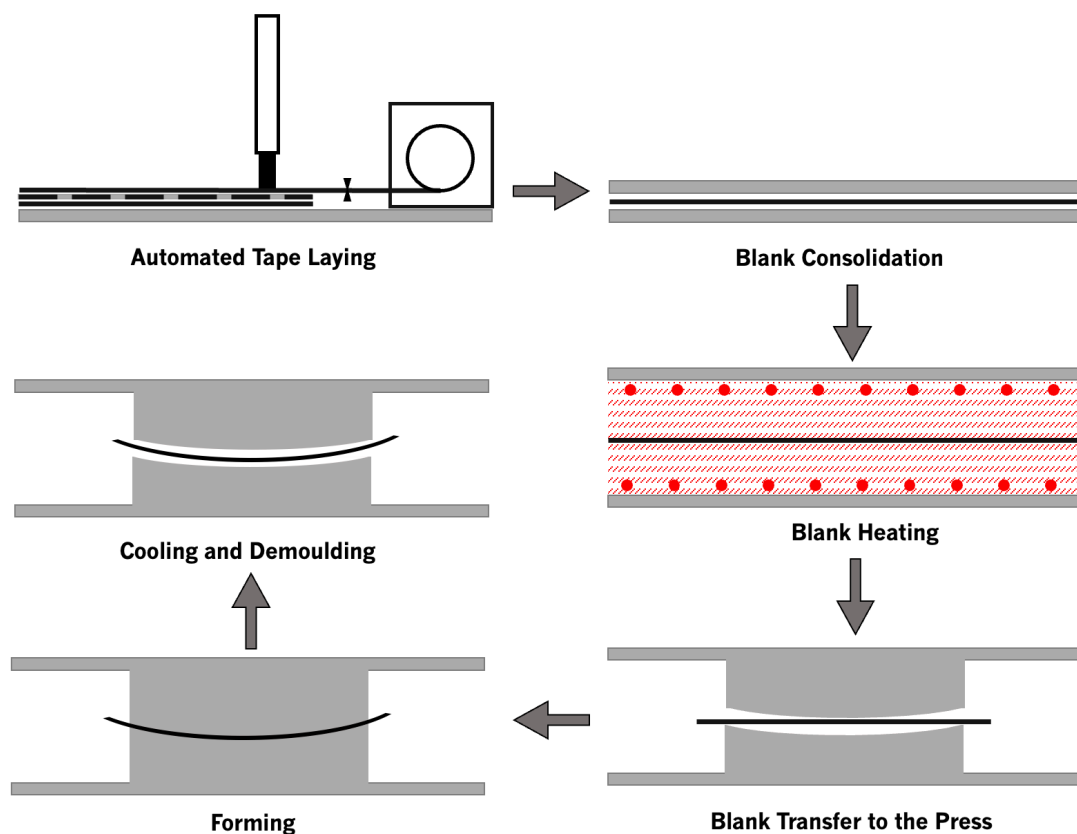


**Figure 3.4:** Thermoplastic Hot Stamping process [35].

### 3.2. Raw and composite materials

In the present work, a mono-component epoxy resin (RTM6 [36]) in the form of a paste was used as matrix to produce composites by heated-VARTM. RTM6 was specially developed for liquid composite



moulding processes. This resin meets the aerospace standards requirements because of its high mechanical properties. Furthermore, it is susceptible to temperature variations, meaning that a slight increase in temperature results in a high reduction of the working window. The carbon fabric HiMax® (HexTow® AS7)[37] was used as the reinforcement of the composite. As illustrated in Figure 3.5, the HiMax® fabric is composed of the following sequence of layers: 1. AS7 carbon fibre aligned along a first direction; 2. ECS 5.5 STs; 3. AS7 carbon fibre aligned along a second direction; and 4. polyester 20D Tex pillar stitch lines.

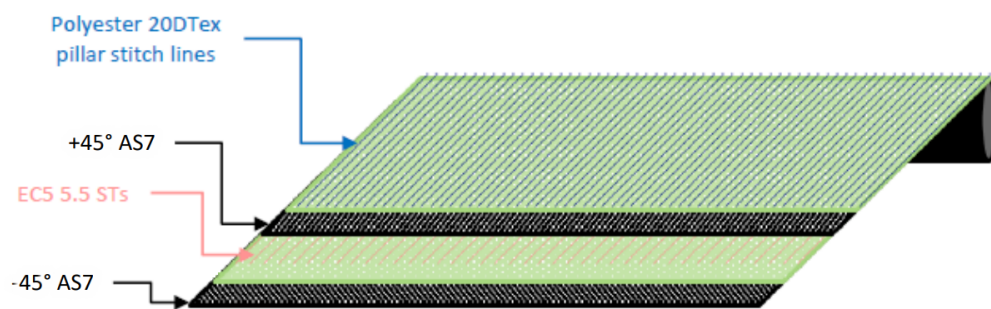


**Figure 3.5:** HiMax® fabric sequence of layers [36].

A unidirectional (UD) thermoset prepreg was used to manufacture composites by hot press. The prepreg consists in a high viscosity epoxy resin DT120 [38] as a base, reinforced by continuous high-performance carbon fibres T1000 [39].

Finally, unidirectional (UD) prepreg thermoplastic tape was used to manufacture composites by hot stamping process. Thermoplastic tape comprising carbon fibres material in a volume fraction of 58% (resin weight fraction of 34%). the matrix can be consolidated in a press, and the tapes can be laid by automated processes such as automated fibre placement (AFP) or tape laying (ATL). The typical consolidation cycle refers to a temperature of 340-380 °C, applied pressure, and consolidation (holding). Also, a 5-25 °C/min cooling rate is suggested to preserve the prepreg tape crystallinity.

According to the manufacturing processes previously described, three types of carbon composite laminates were manufactured: Heated-VARTM, thermoset hot press, and thermoplastic hot stamping. All laminates have the same thickness of 2.5mm.

A composite laminate is defined as the stacking of unidirectional plies with the same or different fibre orientations. The plies can be made of the same or different materials with individual thicknesses. The fibre orientation of each ply defines the stacking sequence with respect to the first axis of the laminate coordinate system, Table 3.1 illustrates the stacking sequence used to manufacture the composite

laminates. It is worth mentioning that thermoset hot press laminates were symmetric, as illustrated in Table 3.1 by the symbol “s”.

**Table 3.1:** Stacking sequences.

Laminate	Total thickness (mm)	Ply thickness (mm)	Stacking sequence
Heated-VARTM	2.576	0.184	$[0^\circ/90^\circ/0^\circ/90^\circ/45^\circ/-45^\circ/0^\circ/90^\circ/-45^\circ/45^\circ/90^\circ/0^\circ/90^\circ/0^\circ]$
Thermoset hot press	2.520	0.140	$[90^\circ/0^\circ/90^\circ/45^\circ/-45^\circ/0^\circ/90^\circ/90^\circ/0^\circ/-45^\circ/45^\circ/90^\circ/0^\circ/90^\circ/0^\circ/90^\circ/0^\circ/90^\circ]$
Thermoplastic hot stamping	2.500	0.125	$[0^\circ/90^\circ/0^\circ/90^\circ/45^\circ/-45^\circ/0^\circ/90^\circ/45^\circ/-45^\circ]_s$

Table 3.2, 3.3, and 3.4, present a summary of the mechanical properties for thermoplastic hot stamping, heated-VARTM and thermoset hot press, respectively.

**Table 3.2:** Summary of the mechanical properties for heated-VARTM material.

Standard	Properties	Unit	Mean value	STDv
ASTM D3039	Tensile strength – $F^{tu}$	MPa	969	54
	Modulus of elasticity – $E^{chord}$	GPa	74	12
	Poisson’s ratio – $\nu$	–	0.04	0.01
ASTM D6641	Compressive strength – $F^{cu}$	MPa	680	30
	Compressive modulus – $E^c$	GPa	60	4
ASTM D3518	In-plane shear stress – $\tau_{12}^m$	MPa	174	3
	Shear modulus of elasticity – $G_{12}^{chord}$	GPa	3.1	0.2
ISO 14130	Interlaminar shear strength – $\tau$	MPa	48.1	3.4

**Table 3.3:** Summary of the mechanical properties for thermoset hot press material.

Standard	Properties	Unit	Mean value	STDV
ASTM D3039	Tensile strength – $F_{11}^{tu}$	MPa	2546.00	155.00
	0° Modulus of elasticity – $E_{11}^{chord}$	GPa	140.00	5.00
	Poisson's ratio – $\nu_{12}$	–	0.36	0.04
ASTM D6641	90° Tensile strength – $F_{22}^{tu}$	MPa	43.00	5.00
	Modulus of elasticity – $E_{22}^{chord}$	GPa	5.00	0.40
ASTM D6641	90° Compressive strength – $F_{22}^{cu}$	MPa	97.60	7.50
	Compressive modulus – $E_{22}^c$	MPa	6.30	0.50
ASTM D3518	In-plane shear stress – $\tau_{12}^m$	MPa	55.00	3.00
	Shear modulus of elasticity – $G_{12}^{chord}$	MPa	3.20	0.10
ISO 14130	Interlaminar shear strength – $\tau$	MPa	59.30	2.70

**Table 3.4:** Summary of the mechanical properties for thermoplastic hot stamping material.

Standard	Properties	Unit	Mean value	STDV
ASTM D3039	Tensile strength – $F_{11}^{tu}$	MPa	1499.00	94.00
	0° Modulus of elasticity – $E_{11}^{chord}$	GPa	123.00	3.00
	Poisson's ratio – $\nu_{12}$	–	0.27	0.04
ASTM D6641	90° Tensile strength – $F_{22}^{tu}$	MPa	60.00	7.00
	Modulus of elasticity – $E_{22}^{chord}$	GPa	8.10	0.10
ASTM D6641	0° Compressive strength – $F_{11}^{cu}$	MPa	769.00	60.00
	Compressive modulus – $E_{11}^c$	GPa	113.00	15.00
	90° Compressive strength – $F_{22}^{cu}$	MPa	147.00	15.00
	Compressive modulus – $E_{22}^c$	MPa	8.50	1.00
ASTM D3518	In-plane shear stress – $\tau_{12}^m$	MPa	347.00	31.00
	Shear modulus of elasticity – $G_{12}^{chord}$	GPa	4.10	0.04
ISO 14130	Interlaminar shear strength – $\tau$	MPa	94.60	2.10
ASTM D5528	Mode I interlaminar fracture toughness – $G_{Ic}$	kJ/mm <sup>2</sup>	0.99	0.06
ASTM D7905	Mode II interlaminar fracture toughness – $G_{IIc}$	kJ/mm <sup>2</sup>	2.24	0.14
ASTM D5766	Open-hole tensile strength – $F_x^{OHTu}$	MPa	481.00	42.00
ASTM D6484	Open-hole compressive strength – $F_x^{OHCu}$	MPa	337.00	32.00

### 3.3. Adhesive and adhesive joints characterisation

A 3M™ Scotch-Weld™ (EC-9323) structural epoxy adhesive was characterized in the present work and it was applied in several combinations of composite-to-composite adhesive joints. The adhesive consisting of two-component epoxy paste EC-9323 B/A and EC-9323-150 B/A This adhesive cures at room temperature or with mild heat to form a durable structural bond. It can adhere to a variety of substrates, including metals, glass, ceramics, and plastics, such as GFRP and CFRP [41].



**Figure 3.6:** A 3M™ Scotch-Weld™ (EC-9323) adhesive

This section presents the experimental program to characterise the adhesive and the bond strengths of composite-to-composite adhesive joints through a series of six distinct tests. All tests are performed using a tensile testing machine.

The experimental program comprises four tests dedicated to the characterisation of the adhesive: bulk tensile test, (TAST) test, (DCB) test and (ENF) test. Besides, the experimental program comprises two tests to characterize composite-to-composite bond strength: single lap joints (SLJ) test and floating roller peel resistance test.

The Table 3.5 outlines the corresponding standards used for each test.

**Table 3.5:** List of the standard used in the experimental program.

Test	Standard
BTT	ISO 527-2 [42]
TAST	ISO 11003-2:2001 [24]
DCB	ASTM D5528/D5528M – 21 [43]
ENF	ASTM D7905/D7905M – 19ε1 [45]
SLJ	D5868 – 01 [46]
Floating Roller Peel Resistance	ASTM D3167 – 10 [50]

Several combinations of adherends were considered, as shown in Table 3.6.

**Table 3.6:** Tests combinations.

Test	Combinations	
	Adherend 1	Adherend 2
<b>DCB</b>	Heated-VARTM	Heated-VARTM
	Thermoset hot press	Thermoset hot press
	Thermoplastic hot stamping	Thermoplastic hot stamping
<b>ENF</b>	Heated-VARTM	Heated-VARTM
	Thermoset hot press	Thermoset hot press
	Thermoplastic hot stamping	Thermoplastic hot stamping
<b>SLJ</b>	Thermoplastic hot stamping	Thermoplastic hot stamping
	Thermoplastic hot stamping	Heated-VARTM
	Thermoset hot press	Thermoset hot press
	Thermoset hot press	Heated-VARTM
	Heated-VARTM	Heated-VARTM
	Thermoplastic hot stamping	Thermoset hot press
	Thermoplastic hot stamping	Thermoplastic hot stamping (Flexible)
<b>Floating Roller Peel Resistance</b>	Heated-VARTM	Thermoset hot press (Flexible)
	Thermoset hot press	Thermoset hot press (Flexible)
	Thermoplastic hot stamping	Thermoplastic hot stamping (Flexible)
	Thermoset hot press	Thermoplastic hot stamping (Flexible)

### 3.3.1. Tensile test

Bulk tensile test was conducted in the present work to determine the tensile properties of the adhesive. Test was performed using bulk specimens (see Figure 3.7) with a dog-bone shape. The specimens were manufactured according to the indications and dimensions of Standard ISO 527 [42], as illustrated in Figure 3.7, the thickness of the specimen was 4mm.

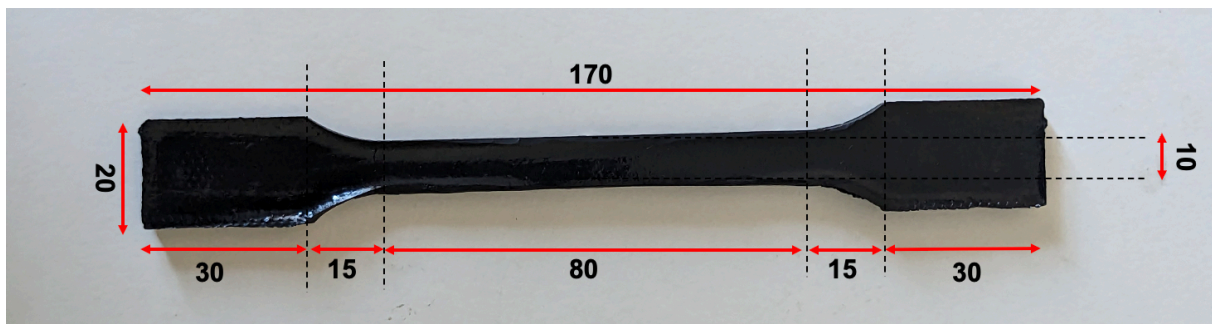


**Figure 3.7:** Bulk tensile specimen dimensions [mm].

Two moulds, presented in Figure 3.8, were used to fabricate the specimens, allowing to produce 12 simultaneously. Each mould is comprised of a metal base and a teflon top. The base is covered with a teflon cover to facilitate the removal of the specimens after curing.

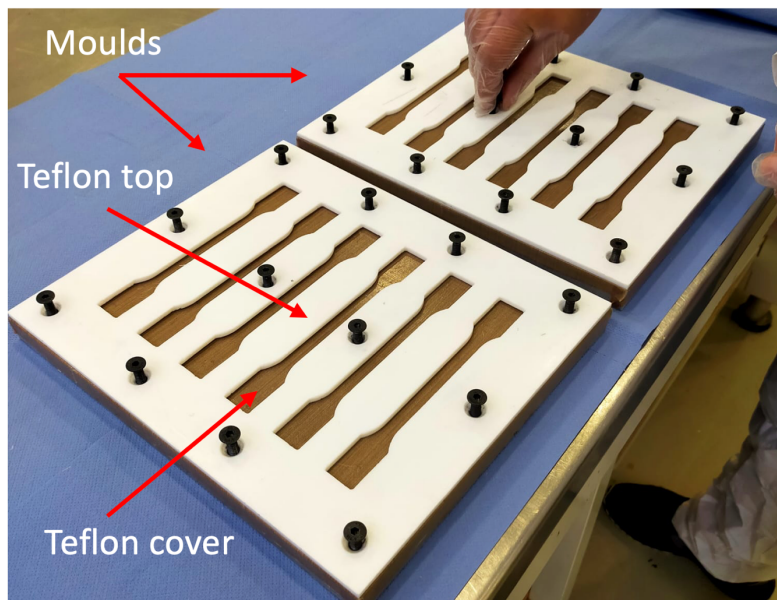


**Figure 3.8:** Moulds.

Mould preparation involved cleaning with acetone followed by the application of a demoulding agent to facilitate removing the specimens after curing. The adhesive was manually applied in the mould cavities,

and the mould was closed for curing. In the first attempt, the specimens were cured inside a preheated muffle for 2 hours at  $65^{\circ}\text{C}$ , according to the manufacturer. However, the obtained results from the first two specimens shows that the adhesive did not fully cure. After that, the curing time was extended from 2 to 24 hours at  $65^{\circ}\text{C}$  to ensure proper curing and avoid inaccurate results.



**Figure 3.9:** Application of the adhesive.

The specimens were tested using an MTS EXCEED MODEL E45 electromechanical testing machine equipped with a 100 kN load cell at room temperature and a 1 mm/ min test velocity. Strain measurement was undertaken using a video extensometer system – Model XT-104 (typical extension resolution of  $0.6\ \mu\text{m}$  and accuracy class B-2) – with a base length of 50 mm and 8 mm in the longitudinal and transverse directions, respectively.

The test was done according to the next procedure:

1. Place gauge marks on the specimen at an equidistant from the midpoint.
2. Measure the width  $b$  to the nearest 0.1 mm and the thickness  $h$  to the nearest 0.02 mm at the centre of each specimen and within 5 mm of each end of the gauge length.
3. Place the test specimen in the grips, taking care to align the longitudinal axis of the test specimen with the axis of the testing machine.
4. Set and calibrate the video extensometer to the gauge length of the test specimen.
5. Set the speed of testing at 1mm/min.
6. Record the force and the corresponding values of the increase of the gauge length and of the distance between grips during the test.

The ISO 527-1 was considered to determine the tensile properties of the adhesive. Four properties are calculated by this standard, the tensile elastic modulus ( $E$ ), the failure stress ( $\sigma_f$ ), the failure strain ( $\varepsilon_f$ ), and Poisson's ratio, ( $\nu$ ).

The tensile elastic modulus is calculated using equation (3.1).

$$E = \frac{\sigma_2 - \sigma_1}{\varepsilon_2 - \varepsilon_1} \quad (3.1)$$

Where  $E$  is the tensile modulus of elasticity, expressed in (MPa);  $\sigma_1$  is the stress, in (MPa), measured at the strain value  $\varepsilon_1 = 0.05\%$ ; and  $\sigma_2$  is the stress, in (MPa), measured at the strain value  $\varepsilon_2 = 0.25\%$ .

Failure stress ( $\sigma_f$ ) is calculated by the ratio between the maximum load and the initial cross-section of the specimen.

$$\sigma_f = \frac{P}{A} \quad (3.2)$$

Where  $P$  is the maximum load, expressed in (N) and  $A$  is the initial cross-section, expressed in ( $\text{mm}^2$ ).

The failure strain  $\varepsilon_f$  refers to the value of strain measured during a test that corresponds to the maximum displacement supported by the specimen.

The Poisson's ratio is calculated following the equation (3.3).

$$\nu = -\frac{\varepsilon_l}{\varepsilon_t} \quad (3.3)$$

Where  $\nu$  is the poisson's ratio,  $\varepsilon_t$  is the strain in the longitudinal direction and,  $\varepsilon_l$  is the strain in the transverse direction.

### 3.3.2. Thick adherend shear test

In TAST tests, the specimen was subjected to a tensile force, resulting in shear stress on the adhesive. The load was applied using a universal-joints design device, illustrated in Figure 3.10, so that negligible torque develops when force is applied to the specimen [24].



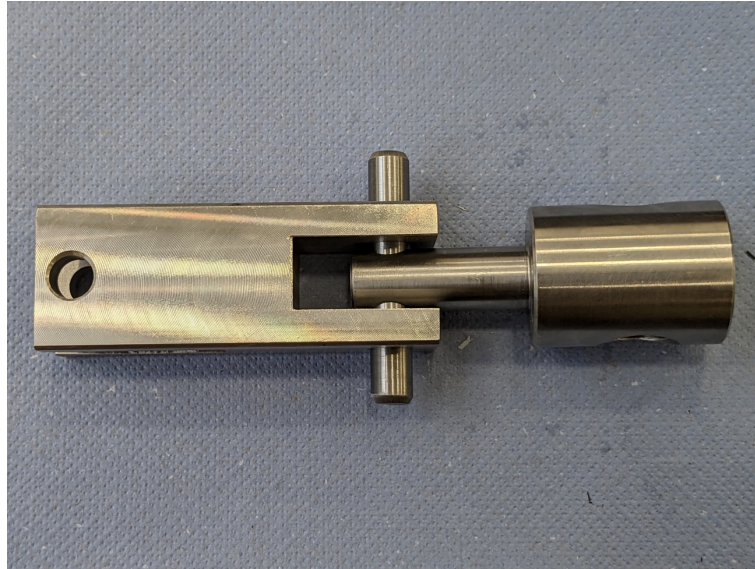


**Figure 3.10:** Universal-joint device

The specimens were prepared according to the standard ISO 11003-2-2001 by bonding steel adherends machined to the shape shown in Figure 3.11. Steel adherends were chosen because of their high modulus. The bonded surface was carefully prepared to have cohesive failure inside the adhesive. The bonding process was carried out securely within a frame, As illustrated in Figure 3.11 (a) that guarantees the precise alignment of the adherends and simultaneously manufacturing of six specimens. To produce a bond of well-defined shape and length, strips coated with a release agent of PTFE of thickness 1.5 mm were inserted in the gaps between the adherends after applying the adhesive and before curing. These strips were removed after the adhesive had cured.

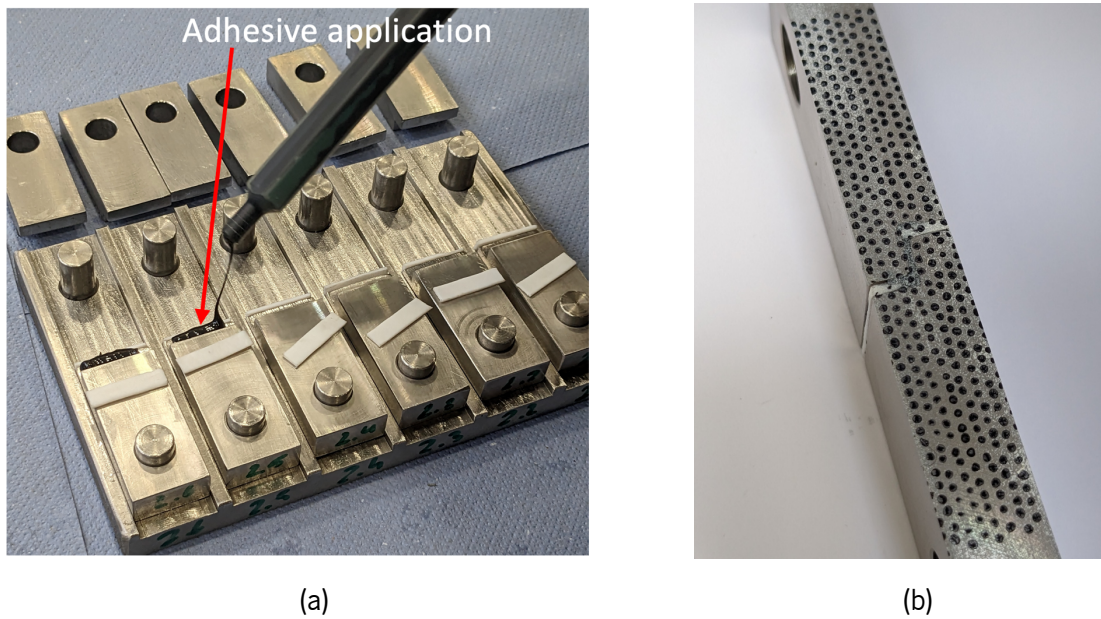


**Figure 3.11:** (a) manufacturing of the specimen and (b) detail of TAST specimen.

The test was done according to the next procedure:

1. Measure the temperature.
2. Measure the length  $l$  of the overlap and the width  $b$  of each specimen to the nearest 0.1 mm.
3. Measure the thickness of the adhesive joint in the overlap zone at both ends and on each side of the specimen with an accuracy of 0.01 mm. i.e., In our case, the bond thickness is obtained from measurements, before bonding, of the thickness of the stepped ends of the adherends and the thickness of the bonded specimen in the overlap region.
4. Record the average value of the four measurements.
5. Place the extensometer.
6. Perform the test with a speed of 0.5mm/min. Figure 3.12 shows TAST setup.
7. Record the force on, and the displacement of, the specimen as it is loaded to fracture.



**Figure 3.12:** TAST setup.

The ISO 11003-2:2001 standard [24] was considered to determine the shear mechanical properties of the adhesive.

The average shear stress  $\tau$  in the adhesive is given by equation (3.4).

$$\tau = \frac{P}{l \times B} \quad (3.4)$$

Where  $P$  is the force applied to the specimen, expressed in (N),  $l$  is the bond length expressed in (m)  $B$  is the width of the specimen.

The shear strain ( $\gamma$ ) in the adhesive is given by the equation (3.5).

$$\gamma = \frac{d_s}{t} \quad (3.5)$$

Where  $d_s$  is the shear displacement of the adhesive  $t$  is the average adhesive thickness measured in the overlap zone at both ends and on each side of the specimen with an accuracy of 0.01mm.

$$d_s = d - \frac{\tau(t_a - t)}{G_a} \quad (3.6)$$

Where  $d$  is the measured displacement,  $\tau$  is the average shear stress on the adhesive,  $t_a$  is the extensometer pin separation,  $t$  is the average adhesive thickness.  $G_a$  is the shear modulus of the adherend.

The shear modulus of the adhesive  $G$  is determined in the elastic portion of the  $\sigma - \gamma$  curves.

$$G = \frac{\tau}{\gamma} \quad (3.7)$$

### 3.3.3. Double cantilever beam test

The DCB specimen, employed to determining fracture toughness ( $G_{Ic}$ ), comprises two rectangular composite laminate plates of uniform thickness bonded using 3M™ Scotch-Weld™ (EC-9323) adhesive. A PTFE tape insert is carefully placed between the two plates to introduce an initial crack. Subsequently, opening forces are applied to the DCB specimen using hinges or loading blocks attached to the pre-cracked end. The controlled opening displacement or vertical crosshead movement governs the opening of the arms of the DCB specimen while concurrently monitoring the force applied and the progression of crack propagation throughout the test. This experimental setup ensures accurate measurements and allows for a comprehensive analysis of fracture behaviour in adhesive joints.

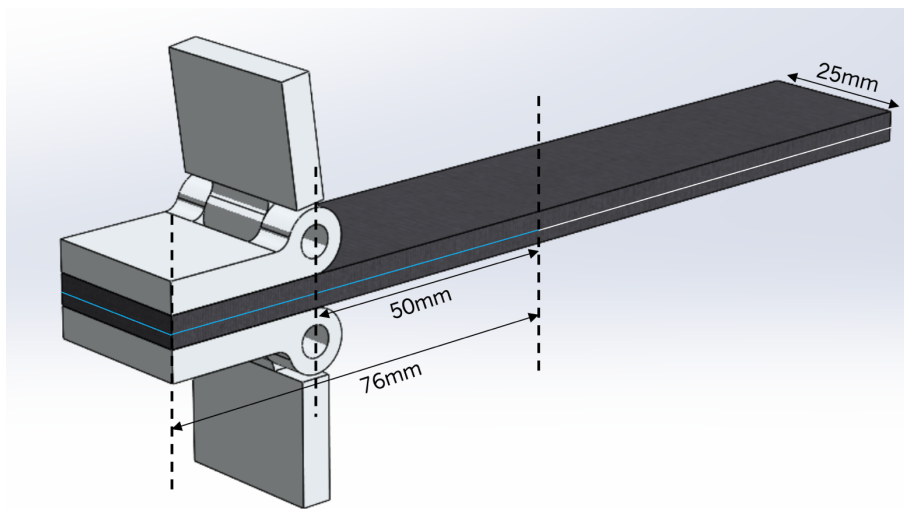


**Figure 3.13:** Double cantilever beam specimen.

The specimens used for testing were carefully extracted from a manufactured panel as illustrated in Figure 3.14, which was constructed using two laminates of uniform thickness.

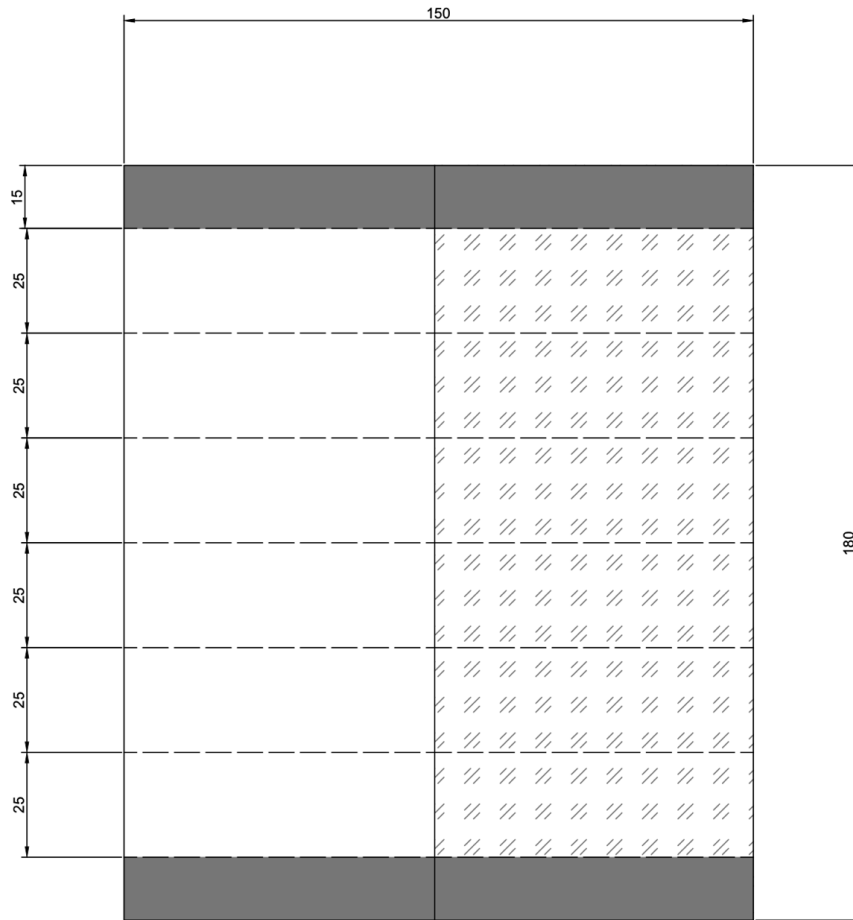


**Figure 3.14:** Test panel.

These laminates were joined using 3M™ Scotch-Weld™ (EC-9323) adhesive, ensuring a bond-line thickness of 0.2mm and cured for 24 hours at 65°C. A steel wire measuring 0.2mm thick was employed to guarantee the desired thickness during manufacturing. Pressure was applied on the panel to ensure proper bonding. The specimen's dimensions are presented in Figure 3.13.

Figure 3.15 shows the manufacturing of the specimens, more specifically, the application of the adhesive.

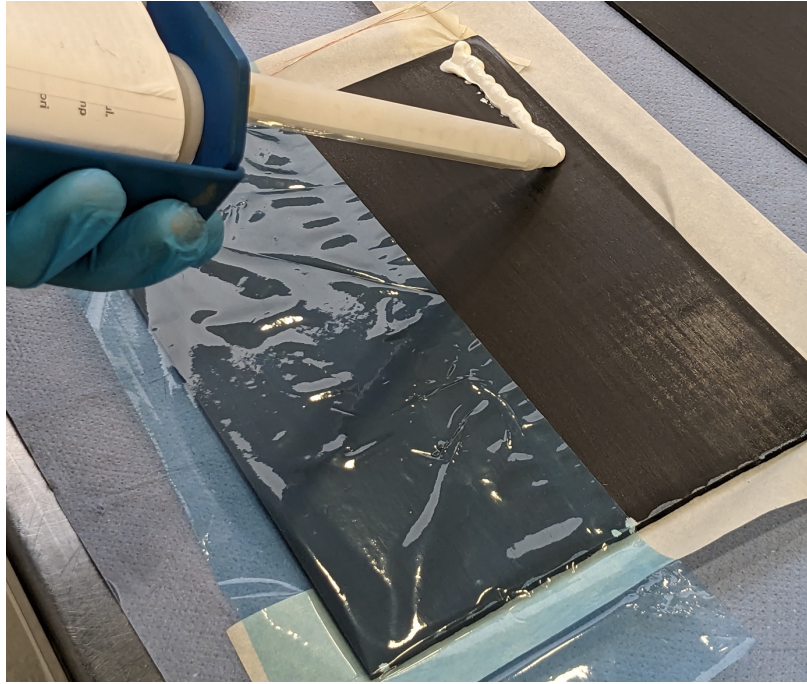
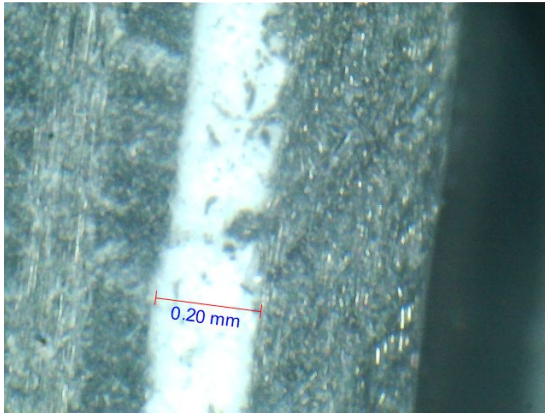


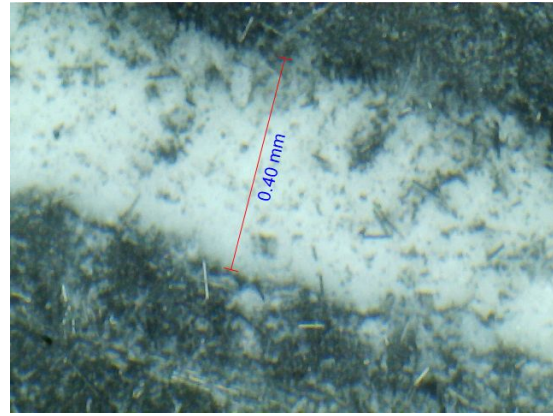
**Figure 3.15:** Specimen manufacturing (adhesive application).

After manufacturing the specimens, the adhesive thickness was measured using a microscope as a first step. The result shows that the thickness varies from 0.2 to 0.4 mm, which reveals the difficulty in guaranteeing the thickness, even using steel wires and applying pressure (0.014MPa), as widely used in literature. Figure 3.16 shows an example of a thickness value taken using the microscope. It's also possible to observe the starter foil located in the middle of the adhesive (d), but in (c), it is placed near the edge, showing the difficulty in producing the DCB specimens.

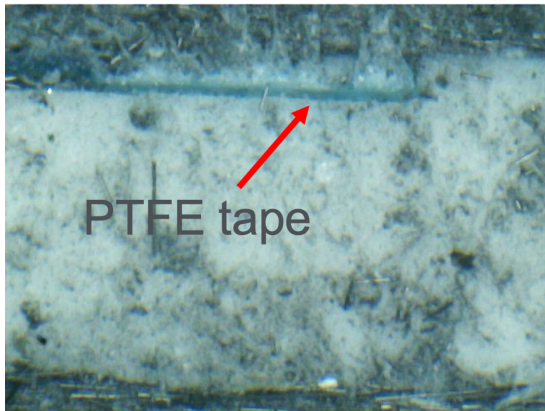
The measurement setup for the test involved several important considerations. For crack length measurement, there are several options available. One approach is to use a travelling microscope. Alternatively, visual measurements aided by optical lenses could be employed or digitally captured images using a video extensometer or DIC (digital image correlation) setup. Our test adopted a video extensometer indicating its accuracy in providing reliable results.



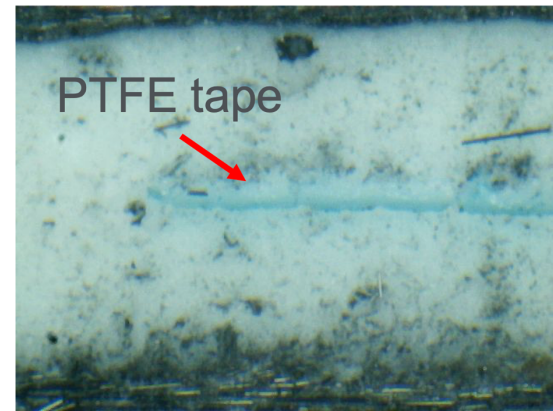
(a) adhesive thickness



(b) adhesive thickness



(c) Position of the PTFE tape near to the edge



(d) Position of the PTFE tape inside the adhesive

**Figure 3.16:** Procedure for the measurement of adhesive thickness

Bonding the piano hinge began by marking the bonding area on the joint edge and placing masking tape to guide the surface preparation. The surface was then abraded using 220-grit sandpaper as illustrated in Figure 3.17, ensuring the removal of the matrix surface layer without damaging the carbon fibres.

After the tape was removed, a solvent-soaked cloth was used to wipe away the dirt on the joint edge and the piano hinge surface. Next, masking tape was applied around the specimen edges to define the bonding area clearly. The adhesive was applied evenly on both surfaces. It was crucial to ensure proper alignment of the piano hinge and prevent any slipping during the bonding and curing process, as illustrated in Figure 3.18. This ensured that the force could be introduced along a straight line. Once the adhesive was applied, residual adhesives along the sides were carefully removed using a sharp knife. Following these steps, the piano hinge was securely bonded to the joint edge while maintaining alignment and preventing any damage.



**Figure 3.17:** Surfaces after preparation.



**Figure 3.18:** Hinges adhesion.

A microscope was used to measure the pre-crack length, denoted as  $a_0$ , referring to the red lines shown in Figure 3.19. Next, a thin layer of white correction fluid on both sides of the crack was applied. This coating facilitated the measurement process. After the layer had dried, vertical lines at regular intervals of 1mm were marked as illustrated in Figure 3.20. These marked lines provided reference points for measuring the crack length precisely.



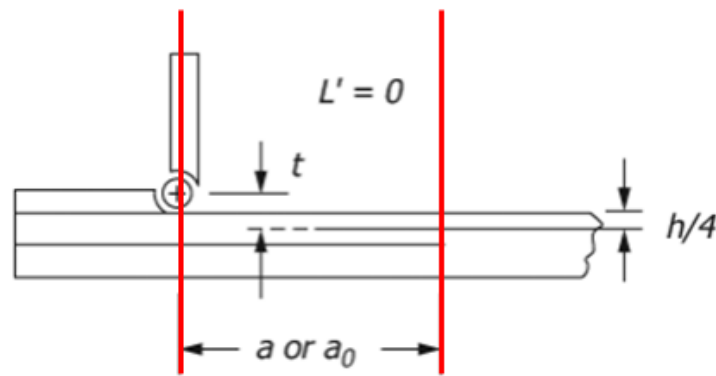


**Figure 3.19:** Pre-crack length [43].

The test was executed according to the procedure described in the standard ASTM D5528/D5528M – 21, [43] following these steps:

1. Load the specimen at a constant crosshead rate 2 mm/min.
2. Record the force and displacement continuously or at frequent and regular intervals during the initial and reloading cycles; a sampling rate of 5 Hz or greater and a target minimum of 500 data points per loading cycle are recommended.
3. Check for crack length, which should be between 3 mm to 5 mm beyond the initial insert. If the unstable crack is less than 3 mm, continue loading so the crack length is between 3 mm and 5 mm. However, loading should be stopped if the unstable crack length is higher than 5 mm. Crack length outside of the 3 mm to 5 mm range should be noted in the report.
4. If the unstable crack is less than 3 mm, continue loading such that the crack length is between 3 mm to 5 mm.
5. If the unstable crack length is higher than 5 mm, loading should be stopped. Crack length outside of the 3 mm to 5 mm range should be noted in the report.
6. Unload the specimen at a rate of 25 mm/min to 50% of the previously reached load during the initial loading stage while continuously recording the load-displacement values. (Pause the unloading at 50%).
7. Using an optical microscope, measure the crack length  $a_1$  on both sides. Mark the crack tip position on both sides. if the difference is more than 2 mm, record and report it.
8. Unload the Specimen until the opening force is zero. (Do not zero the displacement reading at any test stage.)

9. Reload the specimen at a constant crosshead displacement rate of 2 mm/min.
10. On reloading, record the crack length values as many values as possible for the first 10 mm, along with the corresponding load and displacement values.
11. Continue taking crack length values along with force and displacement until the crack reaches 30 mm.
12. Finally, unload the specimen at a constant crosshead rate of 25 mm/min. Pause the unloading at approximately 50 % of the force reached at the end of the test and measure the crack length on both sides. If it varies more than by 2 mm, report in the report.
13. Unload the specimen to the original displacement position.
14. Negative force indicates permanent deformation of the adherend or any other damage. Check with the flat surface for residual curvature.
15. After completing the test, open the specimen to observe the failure. Note down the failure mode and take images of the fracture surface using a professional camera.

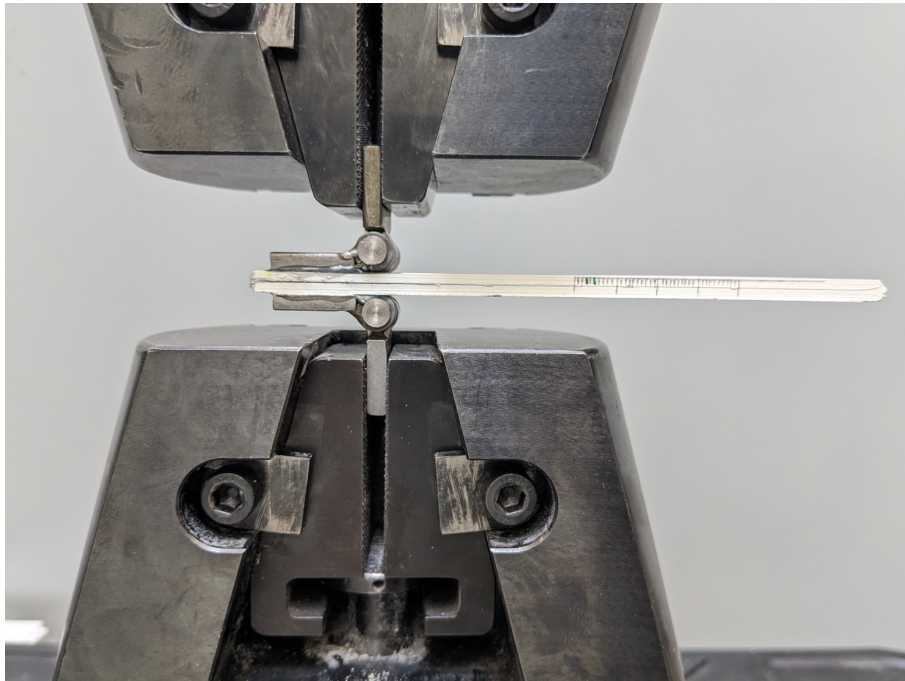


**Figure 3.20:** Setup of the DCB test.

For the calculation of  $G_{Ic}$ , the standard provides three methods: compliance calibration method (CCM), modified beam theory (CBT), and modified compliance calibration method (ECM). The three data reduction methods were evaluated during round-robin testing, and the  $G_{Ic}$  values determined from each

method differed by no more than 3.1 % [44]. The main distinction between the presented methods lies in the process of determining the slope of the compliance plot in relation to the length of the crack. The specimen compliance,  $C_i$  corresponds to each crack length,  $a_i$  recorded during fracture testing is determined using the equation (3.8):

$$C = \frac{\delta}{P} \quad (3.8)$$

Where  $\delta$  is the load-point displacement, and  $P$  is the applied force. The first two compliance values, corresponding to  $a_0$  and  $a_1$ , are determined from the critical forces and the corresponding critical displacement values. Compliance values for all propagation points are determined using force and displacement values corresponding to the visually observed crack growth.

Sometimes, the force-displacement curves of non-precracked (NPC) and precracked (PC) specimens may show some initial nonlinearity due to the way they are loaded or seated. To fix this, the displacement values must be shifted such that the linear fit to the initial part of each curve passes through the origin. This is to be performed by subtracting the displacement value of the nonlinear region (represented by  $\delta_{NL}$ ) from all recorded displacement values.

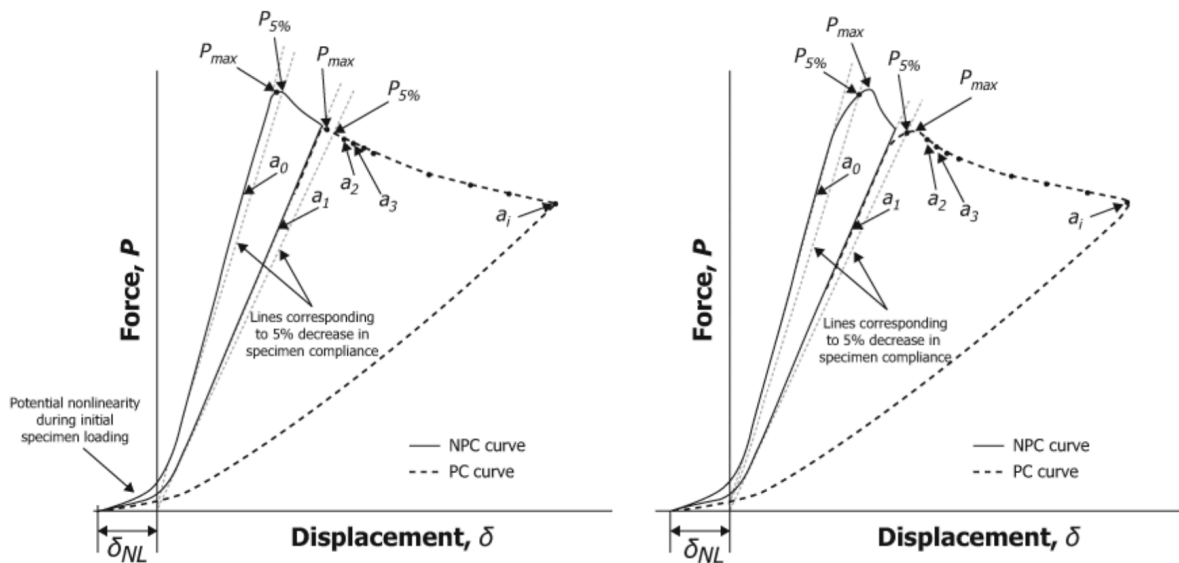
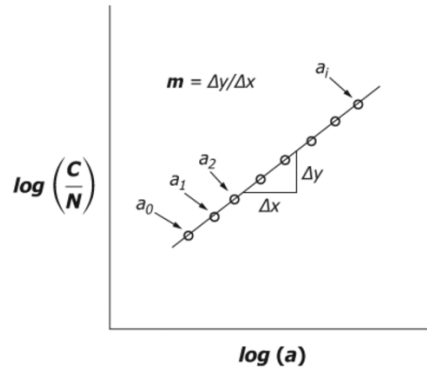


Figure 3.21: Load displacement trace from DCB test [43] .

The governing equation for calculating  $G_{Ic}$  according to the compliance calibration method:

$$G_{Ic} = \frac{mP_c\delta_c}{2ba} \frac{F}{N} \quad (3.9)$$

Where  $P_c$ ,  $\delta_c$ ,  $b$ , and  $a$  are the load, displacement, width, and crack length in each stage of the test, respectively. The  $m$  value is calculated through the slope of  $\frac{C}{N}$  vs  $a$ , in logarithmic scaling as illustrated in Figure 3.22.



**Figure 3.22:** Compliance calibration [43].

$F$  is a parameter that corrects for the effects of large displacement at fracture, while  $N$  is a parameter that accounts for large displacements and fracture and for stiffening of the specimen by the piano hinges:

$$F = 1 - \frac{3}{10} \left( \frac{\delta_c}{a} \right)^2 - \frac{3}{2} \left( \frac{\delta_c t}{a^2} \right) \quad (3.10)$$

$$N = 1 - \left( \frac{L'}{a} \right)^3 - \frac{9}{8} \left[ 1 - \left( \frac{L'^2}{a} \right) \right] \left( \frac{\delta_c t}{a^2} \right) - \frac{9}{35} \left( \frac{\delta_c}{a^2} \right)^2 \quad (3.11)$$

The correction factors ( $F$  and  $N$ ) that have been mentioned will also apply to the other theories. Their nomenclature will remain unchangeable for the other two methods.

The second method, known as the Modified Beam Theory (MBT), calculates  $G_{Ic}$  by assuming a perfectly built-in double cantilever beam in the beam theory as presented in Equation (3.12).

$$G_{Ic} = \frac{3P_c \delta_c}{2ba} \quad (3.12)$$

However, this approach tends to overestimate  $G_{Ic}$  because it does not consider the rotation of the specimen during testing. To address this singularity, the double cantilever beam can be treated as if it had a slightly longer crack, denoted as  $a + |\Delta|$ , where  $\Delta$  is a crack correction. The value of  $\Delta$  is determined experimentally by generating a least squares plot of the cube root of the normalised compliance,  $(C/N)^{\frac{1}{3}}$ , as a function of crack length  $a$  as illustrated in Figure 3.23. This plot includes the observed crack initiation values as well as all the propagation values.

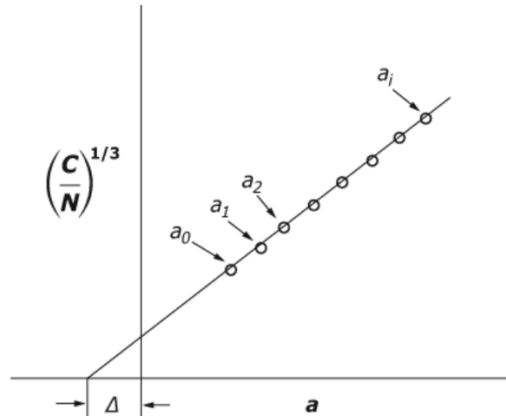


**Figure 3.23:** Modified beam theory [43].

The  $G_{Ic}$  according to the modified beam theory method is calculated using the equation (3.13):

$$G_{Ic} = \frac{3P_c \delta_c}{2b(a + |\Delta|)} \frac{F}{N} \quad (3.13)$$

The final method is the Modified Compliance Calibration (MCC) method, where the relation between crack length and compliance is established as follows:

$$\frac{a}{h} = A_1 C^{\frac{1}{3}} \quad (3.14)$$

Where  $h$  is the thickness, and  $A_1$  the slope of the plot  $\frac{a}{h} = f(C^{\frac{1}{3}})$ , as illustrated in Figure 3.24. The plot is generated using the visually observed crack initiation values and all the propagation values.

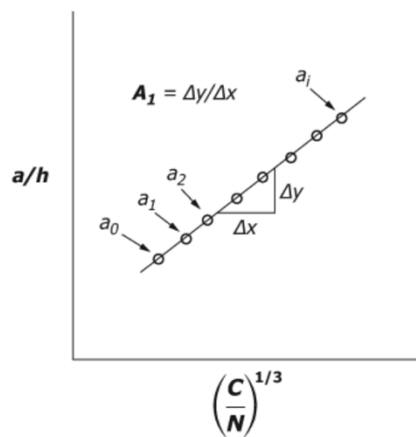


**Figure 3.24:** Modified Compliance Calibration [43].

The  $G_{Ic}$  according to the compliance calibration method is calculated using the equation (3.15):

$$G_{Ic} = \frac{3P_c^2 (C/N)^{\frac{2}{3}}}{2A_1bh} F \quad (3.15)$$

#### 3.3.4. End-notched flexure test

The end-notched Flexure (ENF) test is a practical and widely employed method for characterising fracture toughness in mode II. It presents many advantages, including its simplicity, relatively straightforward specimen preparation, and the capability to provide precise measurements of Mode II fracture toughness.

ENF specimens, commonly employed for determining mode II fracture toughness  $G_{IIc}$  in adhesive joints, comprises two rectangular composite laminate plates of uniform thickness bonded using an epoxy-based adhesive. A PTFE insert is placed between the plates to introduce an initial crack. Subsequently, forces are applied to the specimen through an ENF fixture under displacement-controlled loading. In this work, Fracture toughness in mode II ( $G_{IIc}$ ) is obtained using the compliance calibration (CC) method according to ASTM D7905/D7905M-19 [45].

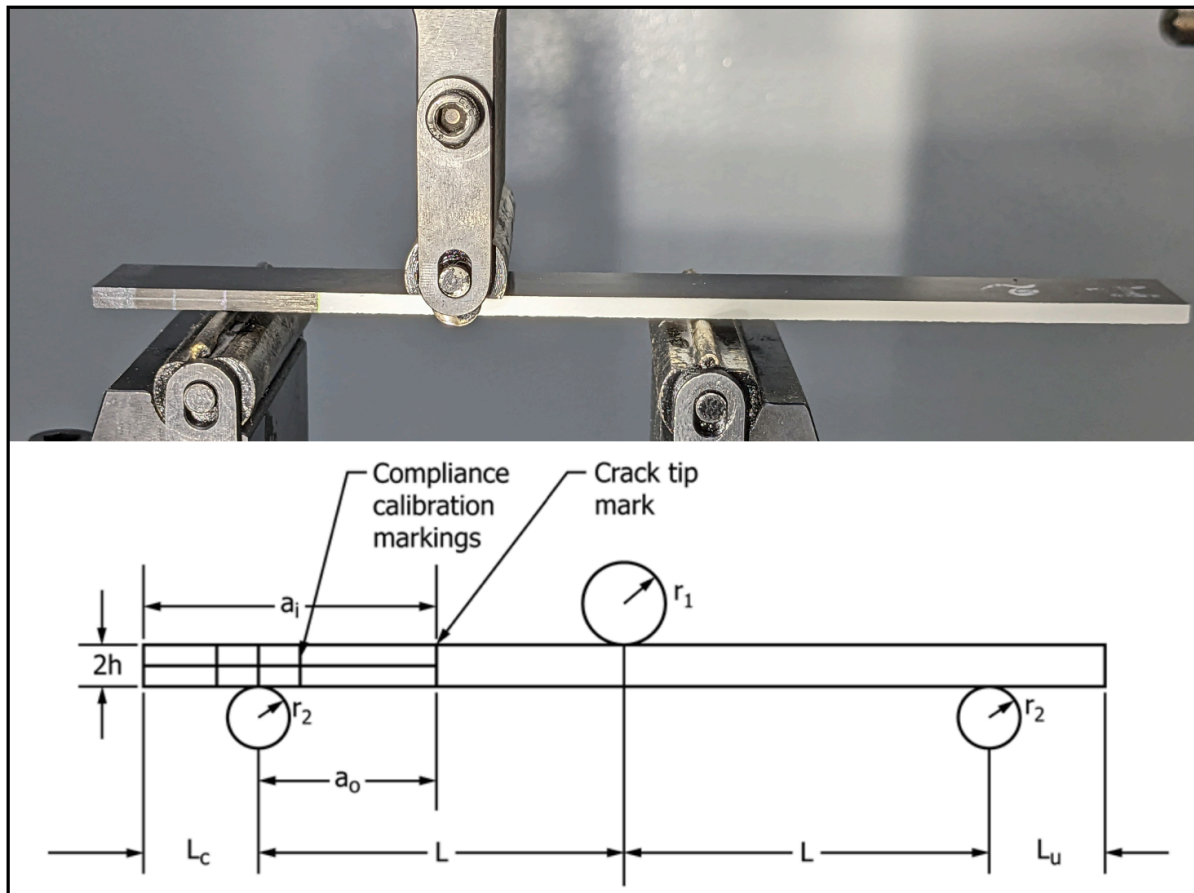


**Figure 3.25:** ENF specimen, Fixture, and Dimensions [45].

In this work, the specimens used for determining  $G_{IIc}$  were carefully extracted from the manufactured composite panels illustrated in Figure 3.26. constructed using two carbon fibre laminates of uniform thickness 2.5mm.

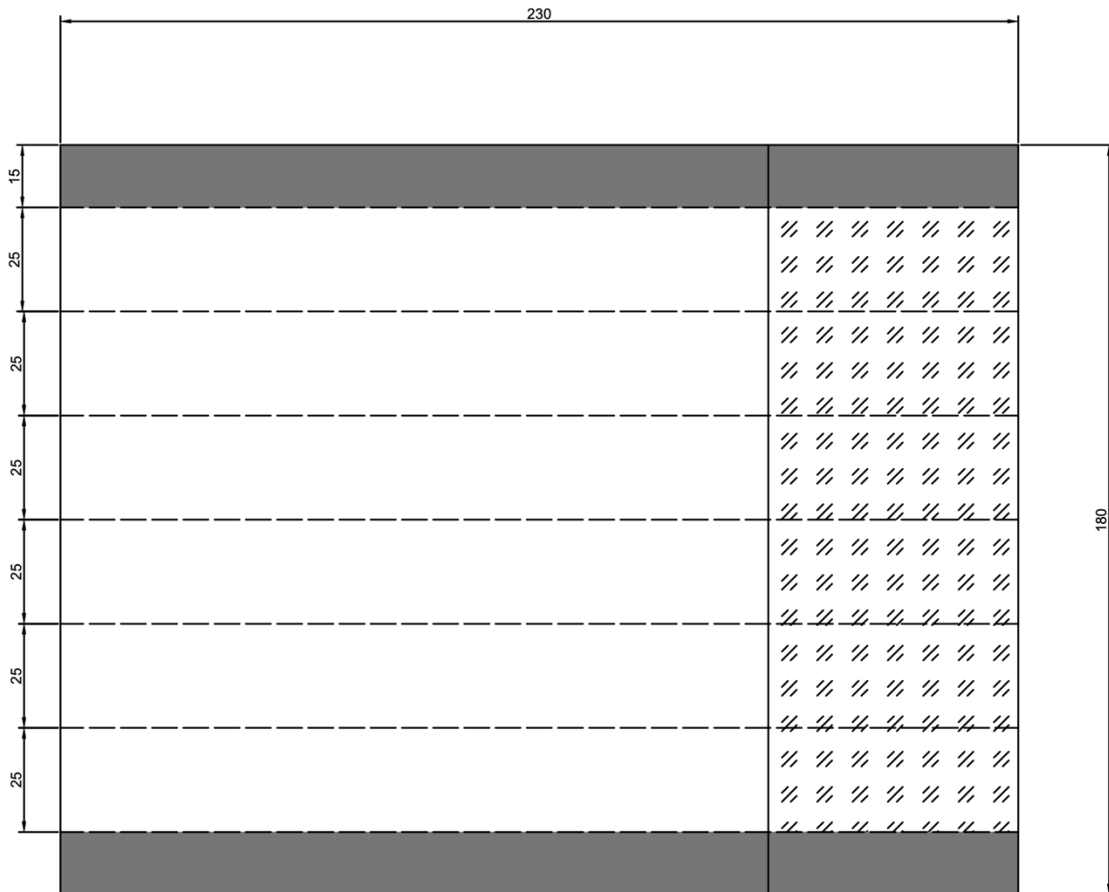


**Figure 3.26:** Composite panel.

These laminates were joined using 3M™ Scotch-Weld™ (EC-9323) adhesive, ensuring a bond-line thickness of 0.2mm and cured at 65 degrees for 24 hours, pressure of 0.014 MPa was applied to ensure proper bonding. A steel wire measuring 0.2mm in thickness was employed to guarantee the desired thickness during the manufacturing process. The test's dimensions are shown in Table 3.7.

**Table 3.7:** Test's dimensions.

$r_1$ [mm]	9.8
$r_2$ [mm]	4
$a_0$ [mm]	30
$L$ [mm]	50
$L_c$ [mm]	30
$L_u$ [mm]	$\geq 45$



Several options are available for crack length measurement, similar to the DCB test. One option is to use a travelling microscope. Alternatively, visual measurements aided by optical lenses could be employed, or digitally captured images using a video extensometer or DIC (digital image correlation) setup. Our test adopted a video extensometer on literature, indicating its accuracy in providing reliable results.

The risks associated with adhesive testing include various factors that can lead to failure or inaccurate results. One such risk is the possibility of failures other than cohesive, such as adhesive failure or the failure of the adherents. The pre-moisture and curing conditions can also impact the adhesive, affecting its overall performance. Another risk is the potential for permanent deformation of the adherends, which can compromise the integrity of the adhesive joint.

To ensure accurate measurements, it is essential to consider the measuring technique and loading fixture. The machine stiffness calibration, which involves determining the stiffness of the testing equipment, must be properly performed. Misalignment of the specimen in the supports and load line within the loading fixture can introduce errors and should be carefully addressed. During specimen mounting, it is important to verify that the loading and support rollers are aligned parallel to each other. This alignment guarantees consistent loading conditions. Additionally, the longitudinal direction of the specimen should be perpendicular to the direction of the rollers. Manual adjustment of the moving crosshead should be performed until the loading roller contacts the specimen, ensuring proper positioning within the testing setup.

It is important to mark the specimens on their lateral edges and support rollers with a vertical line to facilitate the positioning of the specimens in the testing machine. This marking can assist in accurately aligning the specimens during testing.

Specific measurements need to be taken. Each specimen's width ( $B$ ) should be measured at three points corresponding to the contact locations of the three rollers. Additionally, each specimen's thickness ( $2h$ ) should be measured at six points, with two measurements at each previously determined width measurement point (one on the left side and one on the right side).

For every specimen, two experimental procedures are required:

- Three experimental procedures with NPC (2 CC tests and 1 Fracture test (FT)).
- Three experimental procedures with PC (2 CC tests and 1 Fracture test FT).

After the test's completion, two fracture toughness values will be measured: one from the NPC and one from the PC specimen.

The loading and unloading rate for (CC) and (FT) tests is 0.5mm/min.

A light coating of white spray paint was applied to the specimen edges. This facilitates the visual detection of the crack tip and in making (CC) markings. Once the paint was dried, the insert tip was marked with a thin vertical pencil line. The edges were then marked with three vertical compliance calibration markings, within the cracked region, at distances of 20, 30, and 40 mm from the tip of the insert as illustrated in Figure 3.27.

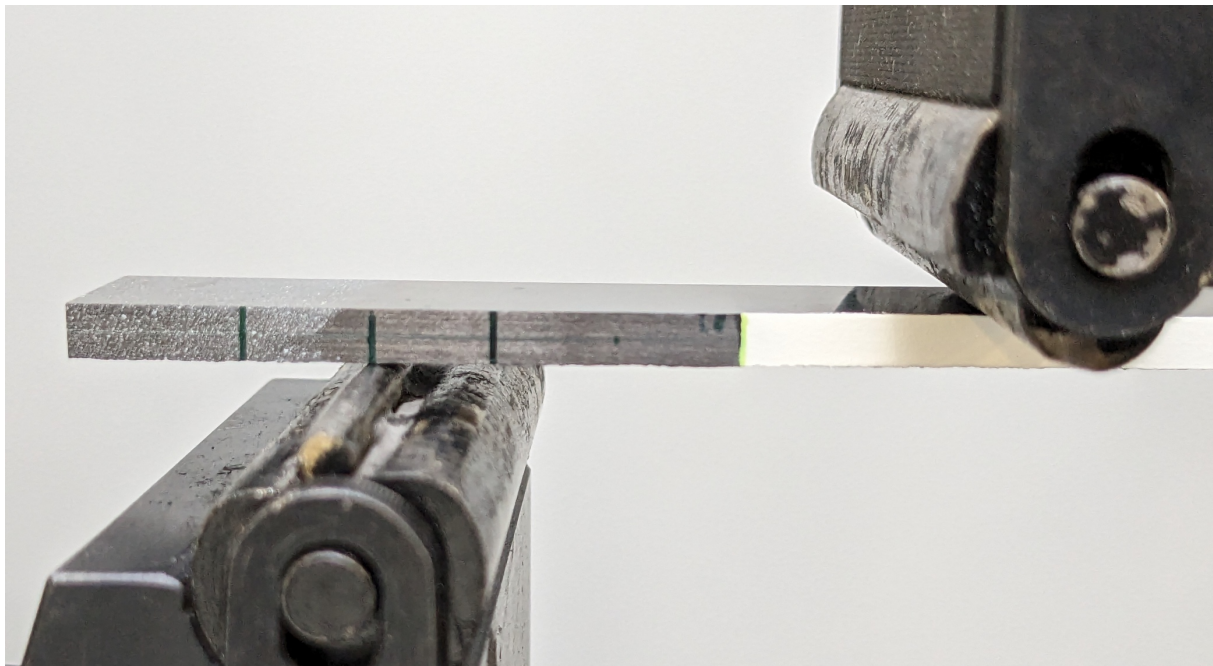


**Figure 3.27:** Compliance calibration markings on the ENF specimen.

The NPC compliance calibration was done according to the next procedure:

1. Calculate the peak CC forces  $P_1$  and  $P_2$  for  $a = 20mm$  and  $a = 40mm$  respectively.
2. Place the specimen in the fixture so that the farthest CC mark is aligned with the centre of the roller. The first CC test is then performed with a crack length,  $a = 20mm$ .
3. Perform the compliance calibration tests by loading the specimen up to the 50% of the peak CC force for  $a = 20mm$  ( $P_1/2$ ) and then unloading. record the force and deflection data continuously or at frequent and regular intervals during the loading portion only; a sampling rate of 5 Hz or greater and a target minimum of 500 data points per test are recommended.

4. After the completion of CC test for  $a = 20mm$ , reposition the specimen in a way that  $a = 40mm$  i.e., so that the CC mark that is closest to the cracked end is aligned with the centre of the support roller at the cracked end.
5. Perform the NPC CC test to the 50% of peak CC force for  $a = 40mm$  (P2/2)
6. Unloading the specimen in the same way as for the NPC CC test for  $a = 20mm$ .

after finishing the NPC CC test, the NPC FT was performed following these steps:

7. Reposition the specimen in the fixture so that  $a = 30mm$ . This corresponds to placing the centre CC mark over the centre of the support roller that is at the cracked end.
8. Load the specimen until the debonding advances, as seen by a visual assessment on the specimen or by a drop in force on the force versus displacement plot.
9. Unloaded the specimen at a constant rate of 0.5mm/min. the force and displacement data are to be recorded continuously or at frequent and regular intervals during the entire test; a sampling rate of 5 Hz or greater and a target minimum of 1000 data points per test are recommended.
10. Calculate  $a_{calc}$  from the NPC FT unloading data as shown in the data reduction section.

The second experimental procedure follows the same steps as the first. The PC CC test was executed as follows:

1. Make new PC CC markings at a distance of 20, 30 and 40 mm from the  $a_{calc}$ .
2. Perform PC CC tests for  $a=20$  mm and 40 mm and PC FT for  $a = 30mm$ , similarly to the case of NPC CC and NPC FT.
3. The compliances from two different crack lengths are obtained by appropriate placement of the specimen in the fixture. The first CC test is performed with  $a = 20mm$  and the second with  $a = 40mm$ . This is performed using the PC CC markings.

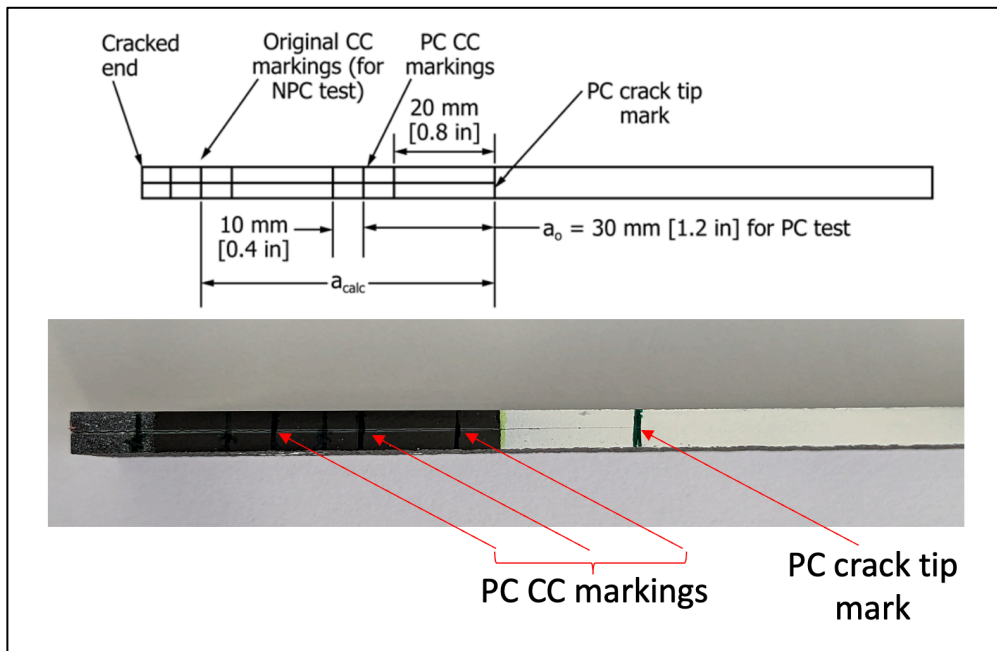


**Figure 3.28:** PC Markings [45].

After finishing the NPC CC test, the NPC FT was performed following these steps:

1. Reposition the specimen in the fixture so that  $a = 30\text{mm}$ . This corresponds to placing the centre PC CC mark over the centre of the support roller at the cracked end.
2. Load the specimen until the debonding advances, as seen by a visual assessment on the specimen or by a drop in force on the force versus displacement plot.
3. Unload the specimen. The force and deflection data are to be recorded continuously or at frequent and regular intervals during the loading portion only; a sampling rate of 5 Hz or greater and a target minimum of 750 data points per test are recommended.
4. Reload the sample until failure, then open the specimen and capture the failure surface images.

The calculation of  $G_{IIc}$  comprises three steps: calculation of NPC CC and PC CC coefficients, determination of Candidate Toughness and assessment of the Candidate Toughness.

NPC CC coefficients are calculated by Plotting the three compliances from the NPC test versus crack length cubed. The three compliances are those from the two CC tests (at  $a = 20$  and  $a = 40\text{mm}$ ) and the fracture test ( $C_0$ , which is at crack length  $a = 30\text{mm}$ ). At each crack length, the compliance is calculated by a linear least squares regression analysis to obtain the slope of the displacement versus force ( $\delta$  versus  $P$ ) data.

For the two CC tests, the regression analysis (curve-fit) includes all data for which the force is greater than or equal to 90 N, including the peak force used during the test. The 90 N force is chosen to be sufficiently large such that the curve-fit excludes any data affected by an initial nonlinearity Figure 3.29.

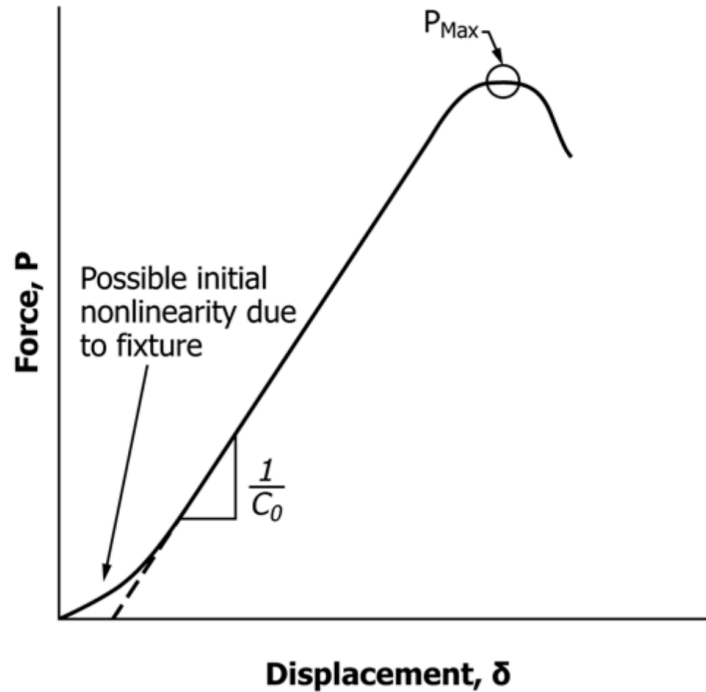


**Figure 3.29:** Illustration of Compliance and Maximum Load Point Determination [45].

For the fracture test, the regression analysis (curve-fit) includes all data for which the force is greater than or equal to 90N and less than or equal to 50 % of the maximum force from the fracture test.

The CC coefficients,  $A$  and  $m$ , are calculated using a linear least squares linear regression analysis of the compliance,  $C$ , versus crack length cubed  $a^3$  data of the form:

$$C = A + ma^3 \quad (3.16)$$

Where  $A$  is the intercept and  $m$  is the slope obtained from the regression analysis. The correlation coefficient,  $r^2$ , for the curve-fit is also calculated.

Note that the precracked CC Coefficients PC CC coefficients are calculated the same way as the NPC CC coefficients, except that the three compliances from the PC test and their respective crack lengths are to be used.

Then, A candidate toughness,  $G_Q$ , is calculated and checked for validity. If it is valid, then:

$$G_{IIC} = G_Q \quad (3.17)$$

Otherwise, the results from the test are discarded (in which case  $G_Q$  is generally used to modify the CC forces for subsequent testing). The NPC and PC candidate toughness is calculated using:

$$G_Q = \frac{3mP_{max}^2a_0^2}{2B} \quad (3.18)$$

Where  $m$  is the CC coefficient,  $P_{max}$  is the maximum force from the fracture test,  $a_0$  is the crack length used in the fracture test, and  $B$  is the width of the specimen. When calculating the NPC  $G_Q$ , these parameters are taken from the NPC CC and fracture tests. When calculating the PC  $G_Q$ , they are taken from tests of the PC.

The NPC and PC candidate toughness is evaluated by calculating the percentages of  $G_Q$  ( $\%G_Q$ ) achieved during compliance calibration.

$$\%G_{Q,j} = \left[ \frac{100(P_j a_j)^2}{(P_{max} a_0)^2} \right]; j = 1,2 \quad (3.19)$$

Where  $\%G_{Q,j}$  are the two values of  $G_Q$  associated with the two compliance tests,  $P_{max}$  is taken from the fracture test,  $P_j$  is the peak value of the force achieved during CC at  $a_j$ , and  $a_j$  is the  $j^{th}$  crack length used during CC. For each NPC and PC test, the two values of  $\%G_Q$  are computed at  $a_1 = 20mm$  and  $a_2 = 40mm$ . If both values satisfy  $15 \leq \%G_Q \leq 35$ , then the candidate toughness is accepted, therefore:

$$G_{IIC} = G_Q \quad (3.20)$$

### 3.3.5. Single-lap joints test

The lap shear test described in ASTM D5868 – 01 (2014) [46] was used for measuring the bonding characteristic of adhesives used in joining composite to composite. This standardised method applies to random and fibre-oriented composite materials, making it flexible in assessing various bonding cases. One of the key advantages of this test method is its ability to generate comparative data on the apparent shear strength of joints formed with different composite materials. Consequently, it facilitates the comparison of composite surface treatments, enabling the evaluation of the effectiveness of different techniques in enhancing bonding characteristics.

The specimens used in the test were fabricated following the guidelines outlined in ASTM D5868 – 01 (2014). Composites laminates were employed to manufacture these specimens and subsequently cut

into flat coupons measuring 25 by 100 mm, with a specified thickness of 2.5 mm. To prepare the surface of the laminate, the recommended method suggested by the adhesive manufacturer was implemented, which involved roughening and cleaning the surface thoroughly.

In the case of thermoplastic adherents, two surface treatments were employed to determine the most suitable option for using a thermoplastic matrix. These treatments included grinding with sandpaper and sulfuric acid. The objective was to assess the effectiveness of each treatment and identify the optimal approach for enhancing adhesion in thermoplastic applications.

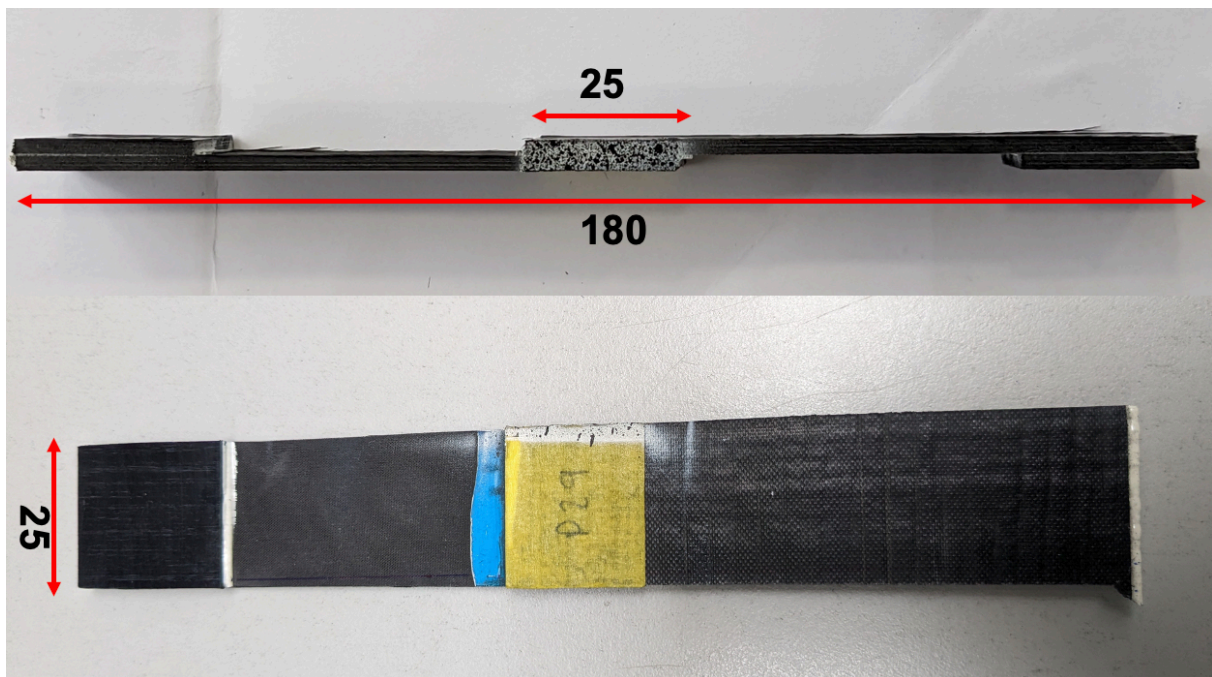


**Figure 3.30:** SLJ Specimen.

To ensure proper application, the adhesive was applied according to the recommendations provided by the adhesive supplier. Additionally, to guarantee the thickness of the adhesive bondline, glass beads with an intended thickness of 0.76 mm were employed. The lap shear overlap, denoting the area of overlap between the bonded specimens, was standardised at 25 by 25 mm. Five lap shear specimens in each case presented in Table 3.6 were manufactured. Specimens were named using the nomenclature PXX, with XX is the specimen number.

The testing machine features self-aligning grips specifically designed to securely hold the specimens in place during the test, effectively preventing any slippage. Furthermore, the tensile machine employed in this study could apply a loading rate of 13mm/min, adhering to the recommended guidelines established by the relevant standard.

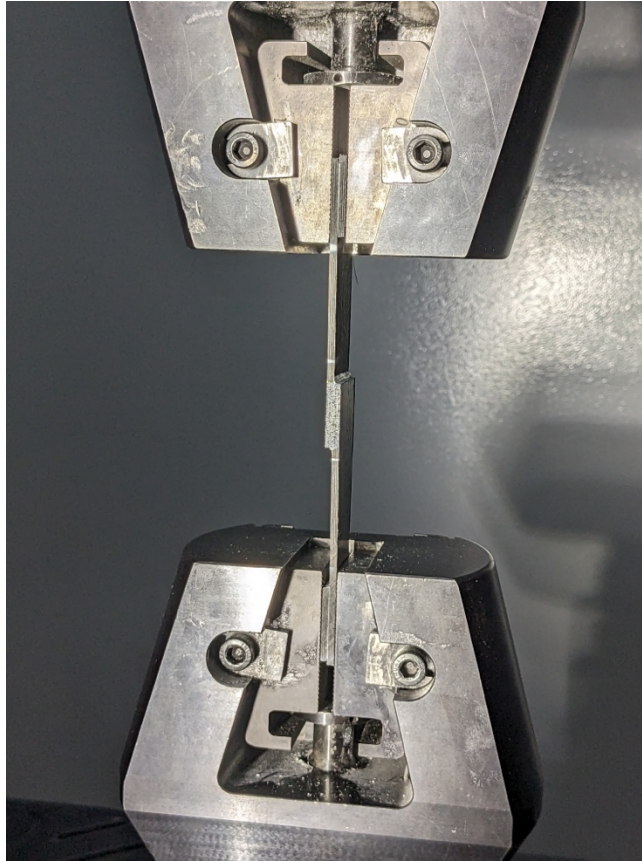


**Figure 3.31:** Testing setup.

The test was done according to the procedure described in the standard ASTM D5868 – 01 (2014), following these steps.

1. Mount the specimen making sure that the sample is fixed between the grips.
2. Load the specimen at a rate of 13 mm/min.
3. Open the specimen and capture the failure surface images (such as fibre tear, cohesive, and adhesive).

#### *3.3.6. Floating roller peel test*

The floating roller method, widely employed as a quality control test and for determining peel strength in the aeronautical industry [47], defines the resistance of high-strength adhesive bonds between rigid adherend and flexible adherend.

In this study, the influence of the adherend on the peel strength of a toughened adhesive is experimentally investigated using the floating roller peel test. The main purpose is to evaluate the peel resistance of



bonded joints when subjected to peeling loads. It is also intended to make a comparison between composite-composite joint performance.

The specimens used in this test were obtained from bonded panels. These panels consisted of two adherends as illustrated in Figure 3.32 and Figure 3.34, with the rigid adherend having a nominal thickness of 2.5mm and the flexible adherend having a nominal thickness of 0.5mm.

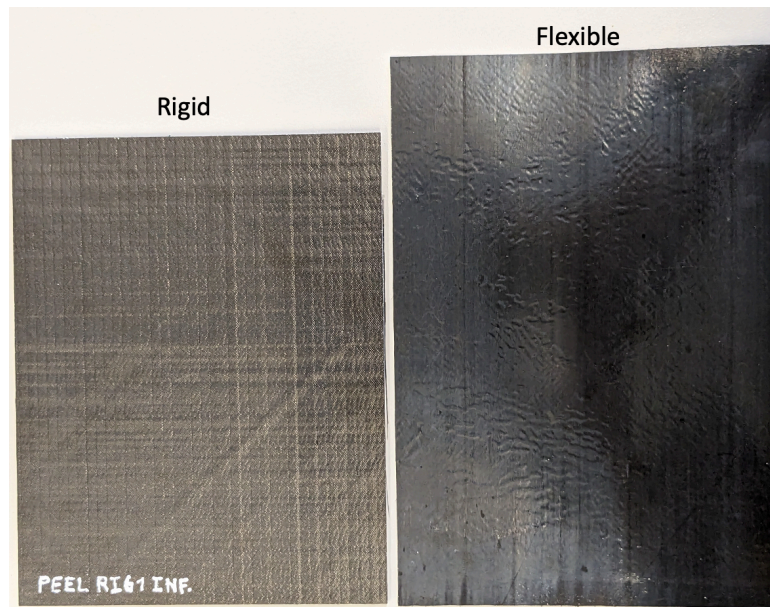


**Figure 3.32:** Example of flexible and rigid adherends.

To ensure the integrity of the bonding process, careful preparation of the adherends was conducted according to the recommendations provided by the adhesive manufacturer. Surface preparation of the adherends involved employing sandpaper to prepare the surfaces, followed by cleaning using acetone-soaked microfiber cloths. This procedure aimed to eliminate any potential sources of contamination that could compromise the peel strength of the bonded joint.



**Figure 3.33:** Pressure application.

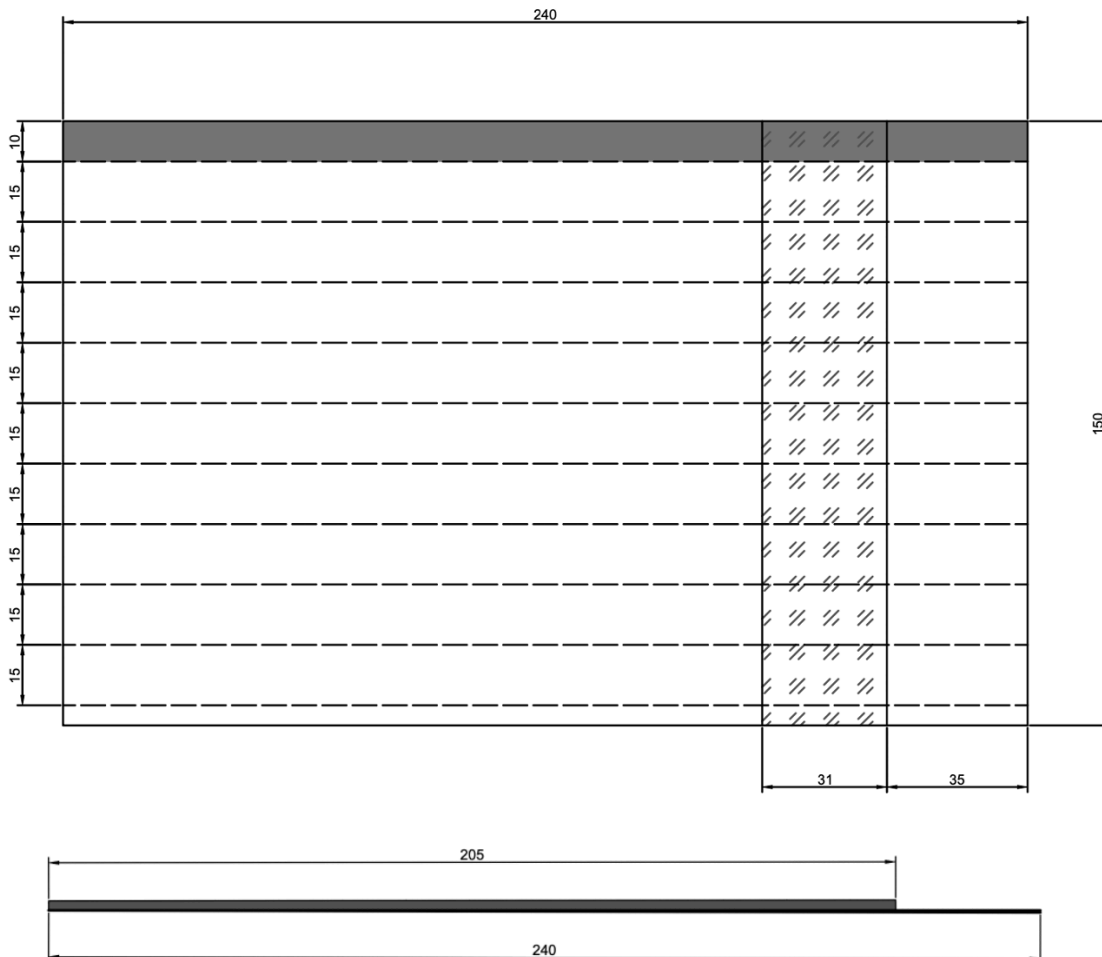


**Figure 3.34:** Floating roller peel test specimen configurations.

A specific segment measuring 31mm of the rigid adherend was masked using PTFE tape release film to create an unbounded area within the specimens.

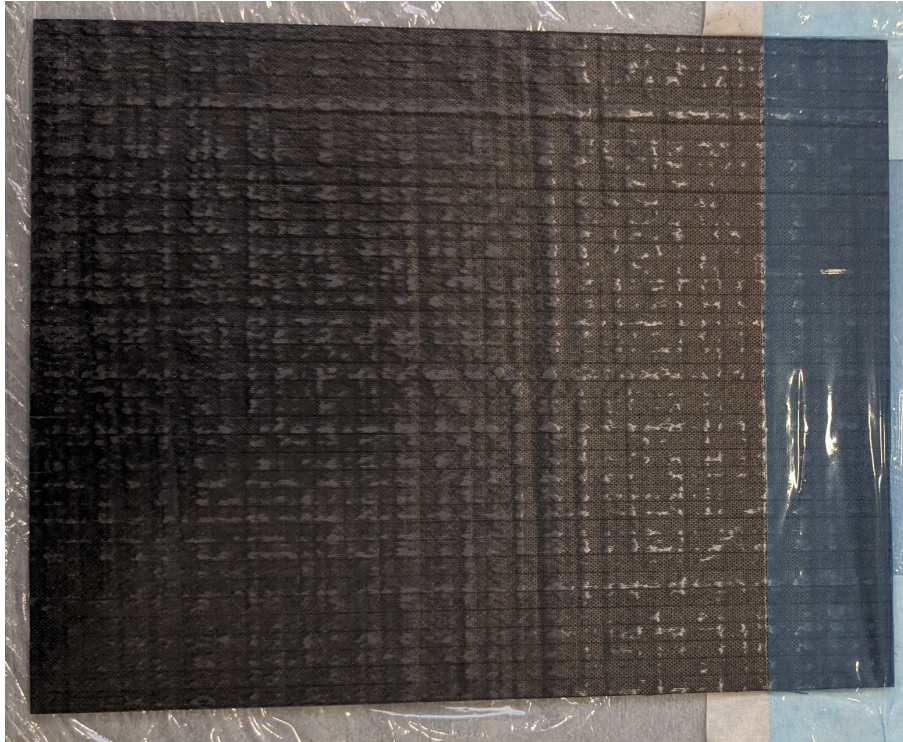


**Figure 3.35:** Unbounded area.

After the bonding stage, the specimens were cured at room temperature for 24 hours. A specific pressure was applied throughout this period to ensure proper bonding between the adherends, as illustrated in Figure 3.33. The specimens were subjected to a post-curing phase at 65°C Celsius for 24 hours to guarantee complete adhesive curing. Finally, specimens were cut, as illustrated in Figure 3.36.

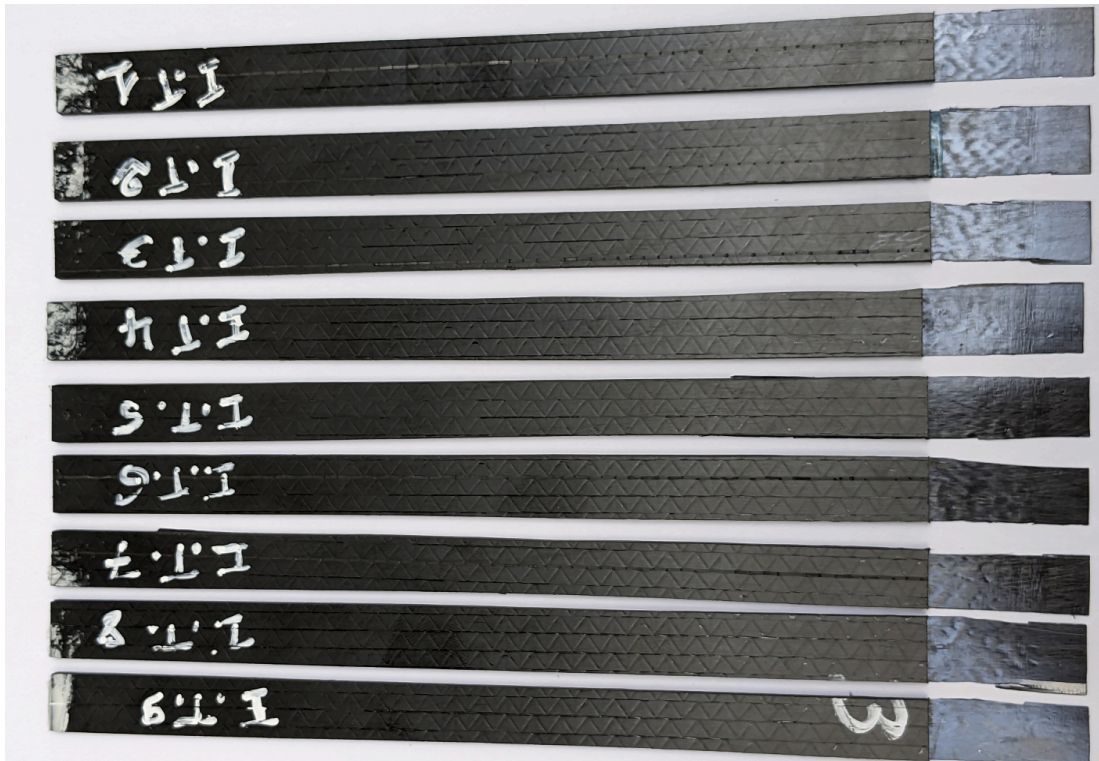


**Figure 3.36:** Specimens after cutting.

The test procedure is presented in the following steps.

1. Insert the test specimen into the peel test fixture as shown in Figure 3.37. The test accessory is attached to the upper grip while the flexible adherent of the specimen is attached to the lower grip.
2. Peel the specimen at 125 mm/min bond separation rate by applying the load at a constant crosshead speed of 125 mm/min [47] [48] [49].
3. During the peel test, make an autographic recording of load versus crosshead movement (load versus distance peeled).
4. Record the load over at least 76.2 mm length of the bond line, disregarding the first 25.4 mm of peel.

According to the ASTM D3167 [50] standard, at the end of the floating roller peel test, the following data must be reported: Average, maximum, and minimum peeling load values for each individual specimen and the average peel strength in  $N/mm$  of width for each combination of materials and failure modes. To determine these parameters, the standard specifies that the first

25.4 *mm* of crack propagation must be ignored, and at least 76.2 *mm* of propagation must be analysed.

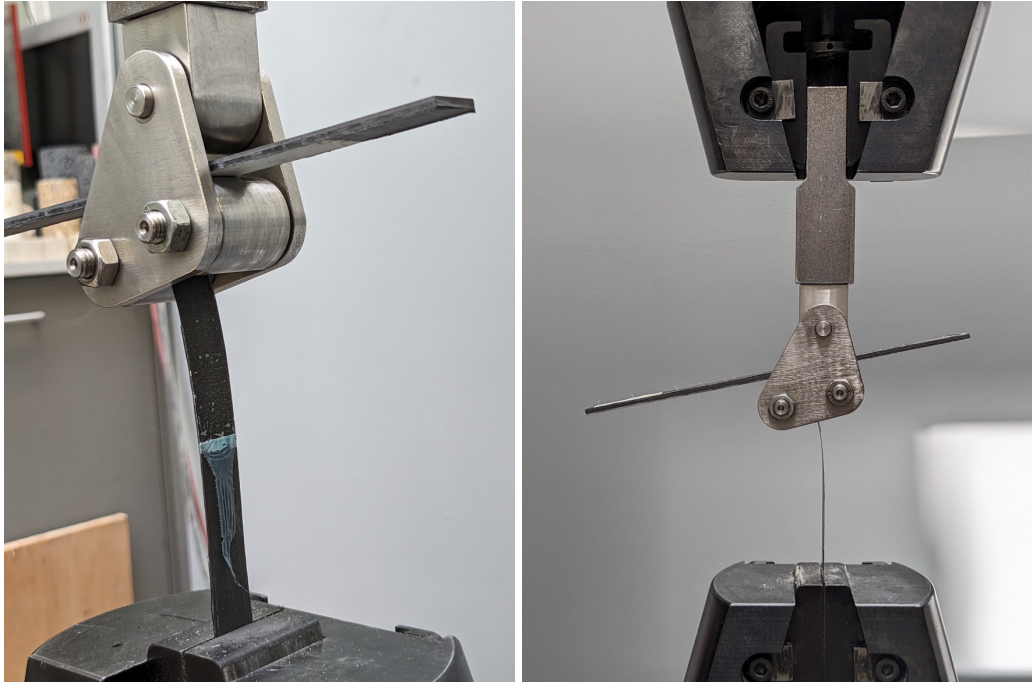


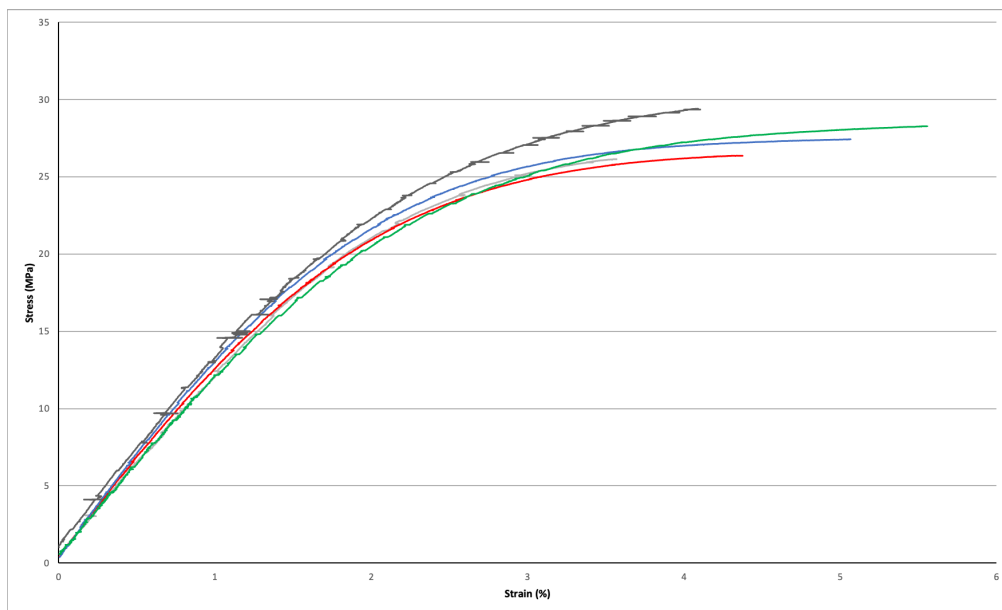
**Figure 3.37:** Testing setup

THIS PAGE WAS INTENTIONALLY LEFT BLANK

## 4. EXPERIMENTAL RESULTS

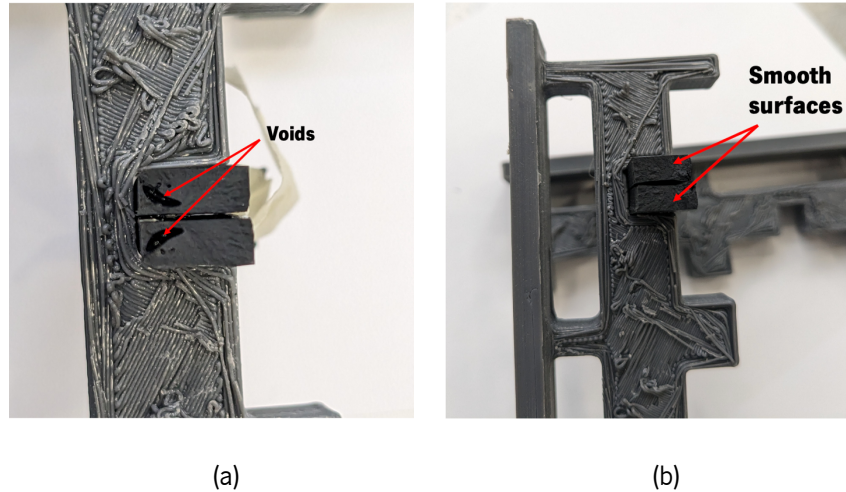
### 4.1. Tensile test

Figure 4.1 shows tensile stress-strain curves of 3M™ Scotch-Weld™ (EC-9323) epoxy adhesive. As it is possible there is high repeatability of the results. The slight difference between the curves in terms of failure strain, as illustrated in Figure 4.1, can be explained by the presence of small fabrication defects in the specimens that could compromise the full ductility of the specimen to develop [51].



**Figure 4.1:** Stress-strain curves of bulk specimen (3M™ Scotch-Weld™ (EC-9323)).

The failure mode exhibit voids in some specimens and a smooth surface in others, as shown in Figure 4.2. As the results reveal, it is confirmed that one of the problems of producing bulk specimens is the difficulty of manufacturing them without defects [22]; more attention should be given to the manufacturing process to avoid any defect that may compromise the result of future test.



**Figure 4.2:** (a) Failure surface with voids and (b) Smooth failure surface.

Table 4.1 presents the individual and average tensile properties of the adhesive. The mean failure stress was  $\sigma_f = 27.53 \pm 1.36 \text{ MPa}$  with a small coefficient of variation of 4.9%. The obtained mean value of  $\varepsilon_f = 4.54 \pm 0.79\%$  with a coefficient of variation of 17.4% and for  $E = 1275 \pm 88.89\%$  with a coefficient of variation of 6.97%. No information is available in the datasheet for all tensile properties to compare.

**Table 4.1:** Tensile mechanical properties.

Specimen	$E$ [MPa]	$\sigma_f$ [MPa]	$\varepsilon_f$ [%]	$\vartheta$
1	1238.00	26.15	3.57	0.42
2	1331.00	26.37	4.38	0.41
3	1389.00	27.44	5.07	-
4	1200.00	28.28	5.56	0.39
5	1176.00	29.42	4.10	0.42
<b>Mean value</b>	1275.00	27.53	4.54	0.41
<b>STDV</b>	88.89	1.36	0.79	0.014
<b>COV (%)</b>	6.97	4.90	17.40	3.41

## 4.2. Thick adherend shear test

Figure 4.3 present the stress-strain curves obtained from TAST testing. High repeatability between the specimens is observed regarding shear strength and shear failure strain. However, looking at the curves it is possible to observe that, after the linear part, there is a deviation. This deviation could be due to several reasons, including material properties, testing conditions, specimen geometry, specimen preparation,



adhesive curing state or defect. It is worth mentioning that three results were lost out of the six specimens tested due to a technical issue during testing.

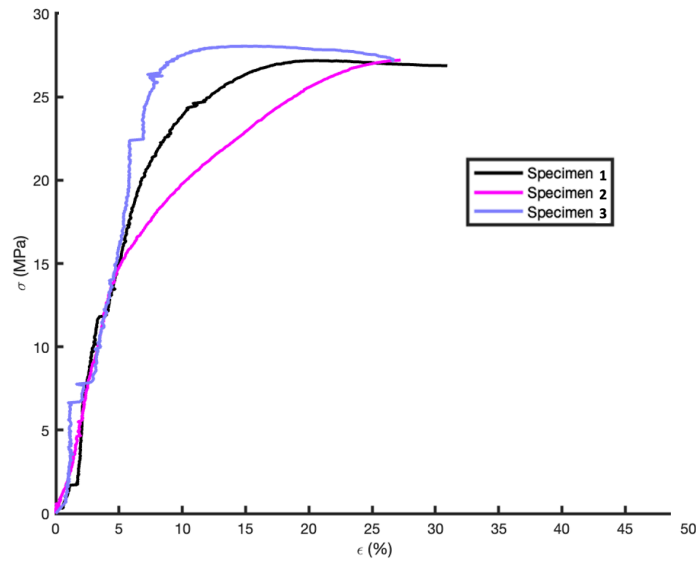


**Figure 4.3:** Stress-strain curves of the TAST specimens.

All TAST specimens experienced an adhesive failure, and the topology of the fractured surfaces was identical as illustrated in Figure 4.4. According to the standard, an adhesive thickness between 2 and 8 mm is recommended. From our test results, we recommend using an initial gap (space between adherends) close to 2 mm. This initial gap gives more flexibility regarding the surface treatment to avoid an adhesive failure.

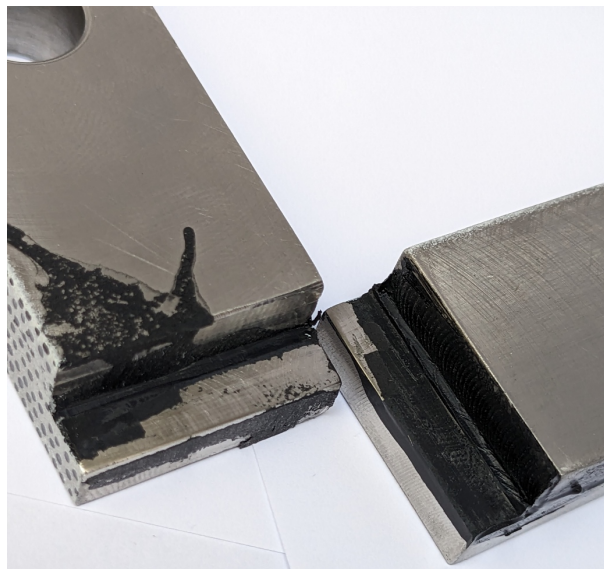


**Figure 4.4:** Adhesive failure of a TAST specimen after testing.

The shear properties of the adhesives (shear modulus, shear strength, and shear failure strain) are determined from the shear stress-strain curves. Table 4.2 presents the adhesive's individual and mean

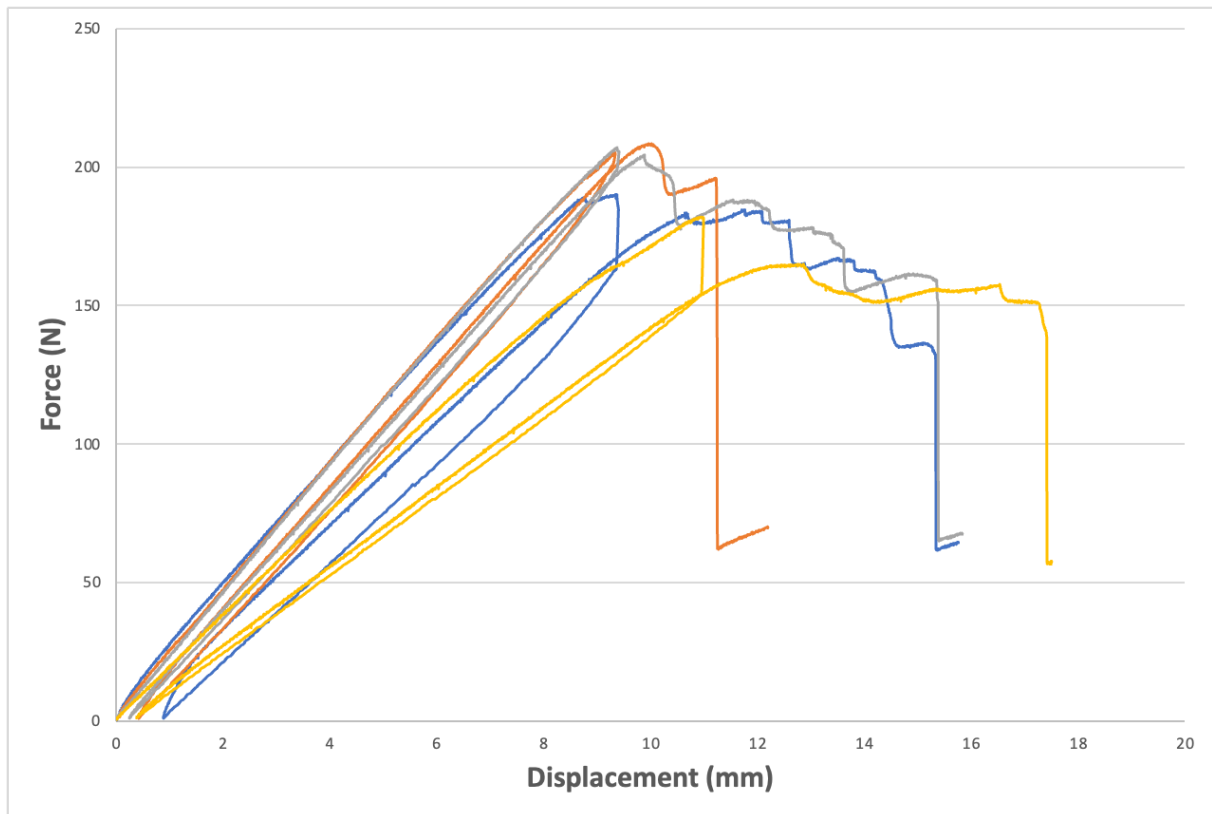
values shear properties. The results of the TAST test gave a mean value of  $\tau_f = 28.08 \pm 0.92$  MPa with a small coefficient of variation of 3.27% which agreed with the value given by the manufacturer (27 MPa). The obtained value of  $\gamma_f = 28 \pm 3.2\%$  with a coefficient of variation of 11.4% and for  $G = 308 \pm 15.7$ MPa with a coefficient of variation of 5.1%.

**Table 4.2:** Shear mechanical properties.

Specimen	$G$ [MPa]	$\tau_f$ [MPa]	$\gamma_f$
<b>1</b>	291	27.18	0.32
<b>2</b>	314	29.02	0.27
<b>3</b>	321	28.04	0.26
<b>Mean value</b>	308	28.08	0.28
<b>STDV</b>	15.7	0.92	0.032
<b>COV (%)</b>	5.1	3.27	11.4

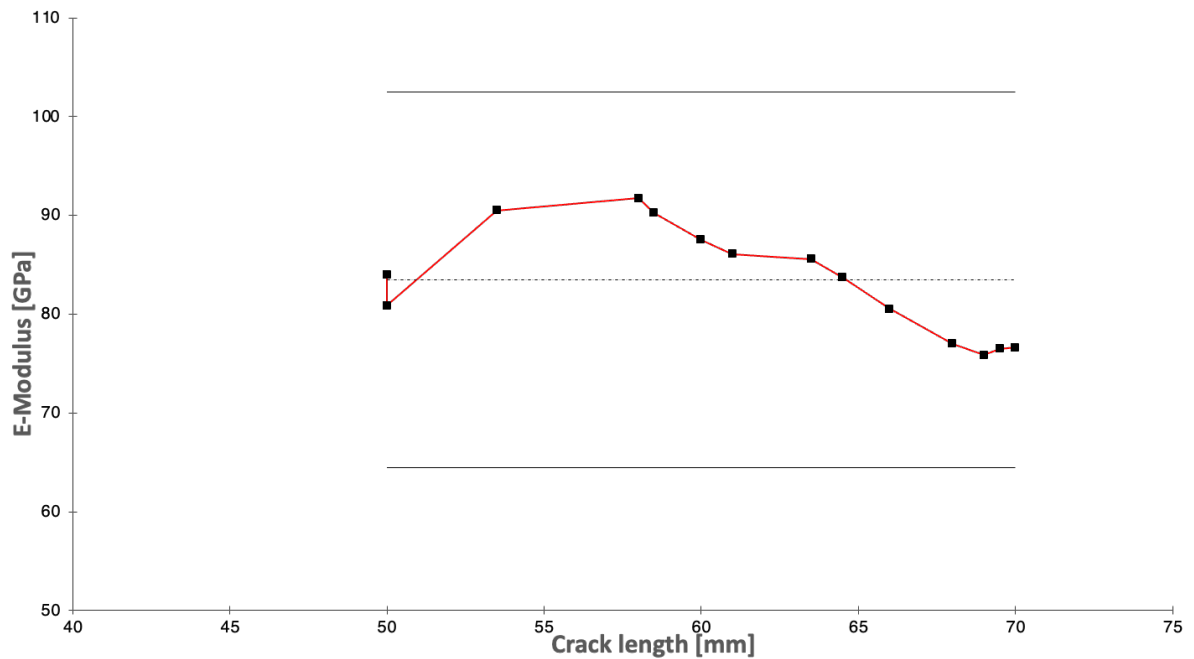
### 4.3. Double cantilever beam test

Figure 4.5 shows the force-displacement curves of the DCB tests. Initially, with the linear increase of P, the energy stored in the specimen increases as well until it equals  $G_{Ic}$  [51].



**Figure 4.5:** a representative Force-Displacement curves of DCB testing.

Once the crack starts to propagate, there is a relaxation of  $P$  corresponding to the crack progression at a constant value of tensile strain energy release rate  $G_I$  [52]. A good agreement was found in the elastic stiffness and during damage propagation.



**Figure 4.6:** E-Modulus during crack propagation.

The R-curves were calculated for all specimens. These curves relate to the evolution of  $G_I$  with  $a$  or  $a_{eq}$  and show the crack propagation with a steady-state value of  $G_I$ . However, some experimental fluctuation occurred in the case of the infusion specimen as shown in Figure 4.7, which can be explained by the changes in crack propagation, or it can be related to adhesion problems, defects, or interlaminar failure in the specimens for this configuration. Also, it should be mentioned that, in the toughened adhesive used in our work, at the onset of crack propagation, progressive toughening occurs through plastic deformation, potentially resulting in microfissures [52].

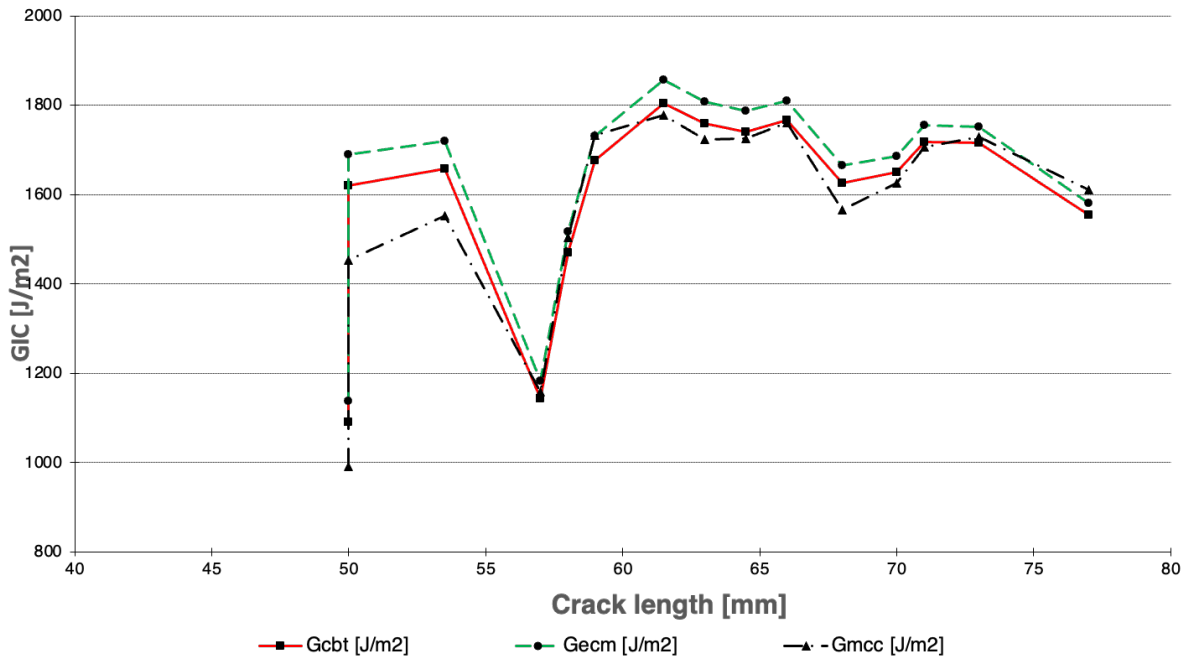


**Figure 4.7:** R-curves of a representative DCB specimen by CCM, CBT and ECM

Following the tests, the failure surfaces of the specimens were documented. The results, illustrated in Figure 4.8, reveal a consistent failure mode across all specimens. Firstly, in the case of Heated-VARTM specimens, a distinctive pattern happened. The crack initiation occurred within the adhesive, progressing cohesively until reaching a crack length of 70mm. Beyond this point, the failure mode transitioned to a fibre tear within the adherend. It is worth to mention that within this combination, one specimen diverged from the norm, demonstrating a comparatively shorter propagation of cracks within the adhesive layer. ultimately, the test provided a valid result regarding  $G_{IC NPC}$  and  $G_{IC NPC}$ . However, the propagation values may not be representative, due to the failure mode experienced during the test.

The thermoplastic hot stamping specimens consistently showed adhesive-based failure, characterised by developing crack patterns distinct from those observed in thermoset hot press specimens. Despite the relatively smooth crack propagation, instability occurred at the crack onset, with crack lengths exceeding 5mm—a critical observation warranting reporting. To conclude, it is essential to exercise caution when interpreting results derived from this test.

Parallel to these results, the thermoset hot press specimens exhibited an adhesive failure, as illustrated in Figure 4.8, with unstable crack propagation accompanied with a big drop in load displacement curve, which led us to non-valid test. We concluded that extra care should be taken when treating the surface and recommend using 60 to 80 mesh sandpaper for optimal results.

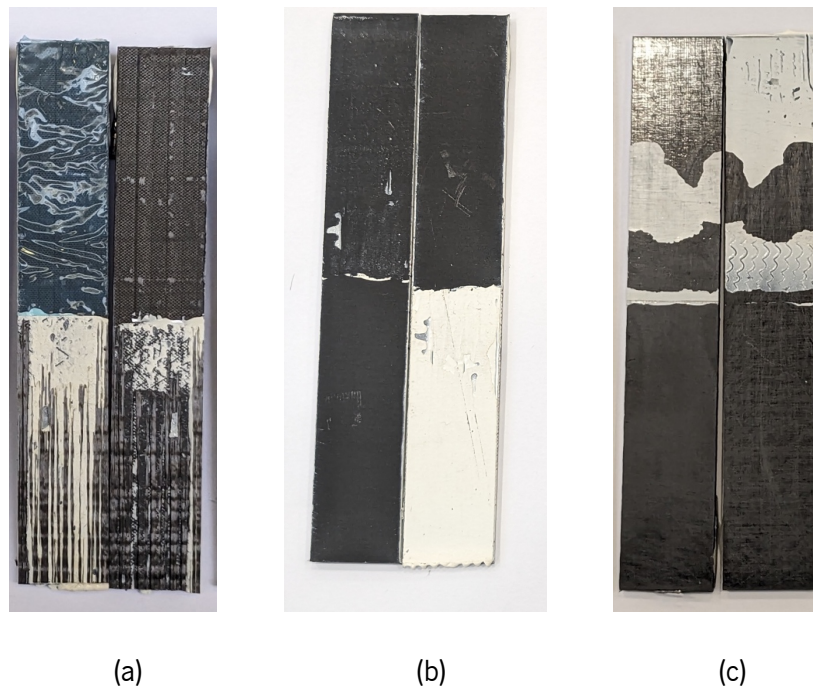


**Figure 4.8:** Representative DCB specimens after testing (a: Heated-VARTM, b: Thermoset hot press and c: Thermoplastic hot stamping).

Table 4.3 shows the values of  $G_{IC}$  obtained by the different data reduction methods described above, showing the consistency of results between the three methods in the case of Heated-VARTM but noticeable different results in the case of thermoplastic hot stamping, which can be related to the unstable crack propagation and the adhesive failure.

**Table 4.3:** NPC and PC interlaminar fracture toughness in mode I.

Specimen	$G_{Ic}(J/m^2)$						
	NPC			PC			
	CBT	ECM	CCM	CBT	ECM	CCM	
<b>Heated-VARTM</b>	<b>1</b>	-	-	-	-	-	
	<b>2</b>	972.4	1395.1	1351.1	1486.6	2109.7	2118
	<b>3</b>	-	-	-	1657.7	1720.7	1553.5
	<b>4</b>	1268.1	1308	1237.7	1291	1309.6	1310.1
	<b>5</b>	1505.1	1539.3	1461.6	1709.1	1734.8	1743.2
	<b>6</b>	1244.8	1326.3	1159.4	1543	1624.3	1474.7
	<b>Mean value</b>	1247.6	1392.175	1302.45	1537.48	1699.82	1681.2
	<b>STDV</b>	217.92	105	132.10	163.76	286.19	309.34
	<b>COV (%)</b>	17.46	7.5	10.14	10.65	16.84	18.4
	<b>Thermoplastic hot stamping</b>	<b>1</b>	-	-	-	-	-
<b>2</b>		55.5	60.7	53.7	64.1	65.8	75.5
<b>3</b>		49.1	53.6	49.4	53.2	55.1	65.1
<b>4</b>		72.7	96.2	76.4	79.4	101.5	132.9
<b>5</b>		60.9	60.2	59.7	73.3	72.4	73.7
<b>6</b>		-	-	-	-	-	-
<b>Mean value</b>		59.55	67.68	59.8	67.5	73.7	86.8
<b>STDV</b>		10	19.28	11.84	11.42	19.85	31.01
<b>COV (%)</b>		16.79	28.42	19.79	16.91	26.90	53.71

#### 4.4. End-notched flexure

Figure 4.9 shows representative load-displacement curves from the ENF FT tests. Consistent results were found between specimens in terms of peak load, although in the case of “Specimens 1 and 2”, as illustrated in Figure 4.9, the maximum load was lower than the rest. The CC forces affect whether the candidate toughness is valid; these forces are directly related to the  $G_{IIc}$  and  $G_{If}$ . To conduct the test, we need an initial value for these parameters. Specimens 1 and 2 are considered as “exploratory”. Generally, the value of  $G_Q$  calculated from the first specimen is not valid; this value of  $G_Q$  is used with a new value of  $G_{If}$  to calculate the new CC forces.

After reaching the peak loads, the load starts to decrease; this first part corresponds to the interesting part of the ENF tests, in which  $G_{IIC}$  is measured. Later, the load increases again when the FPZ reaches the vicinity of the loading cylinder [51]. Similar observations made by *J. P. R. Monteiro et al.* [51].

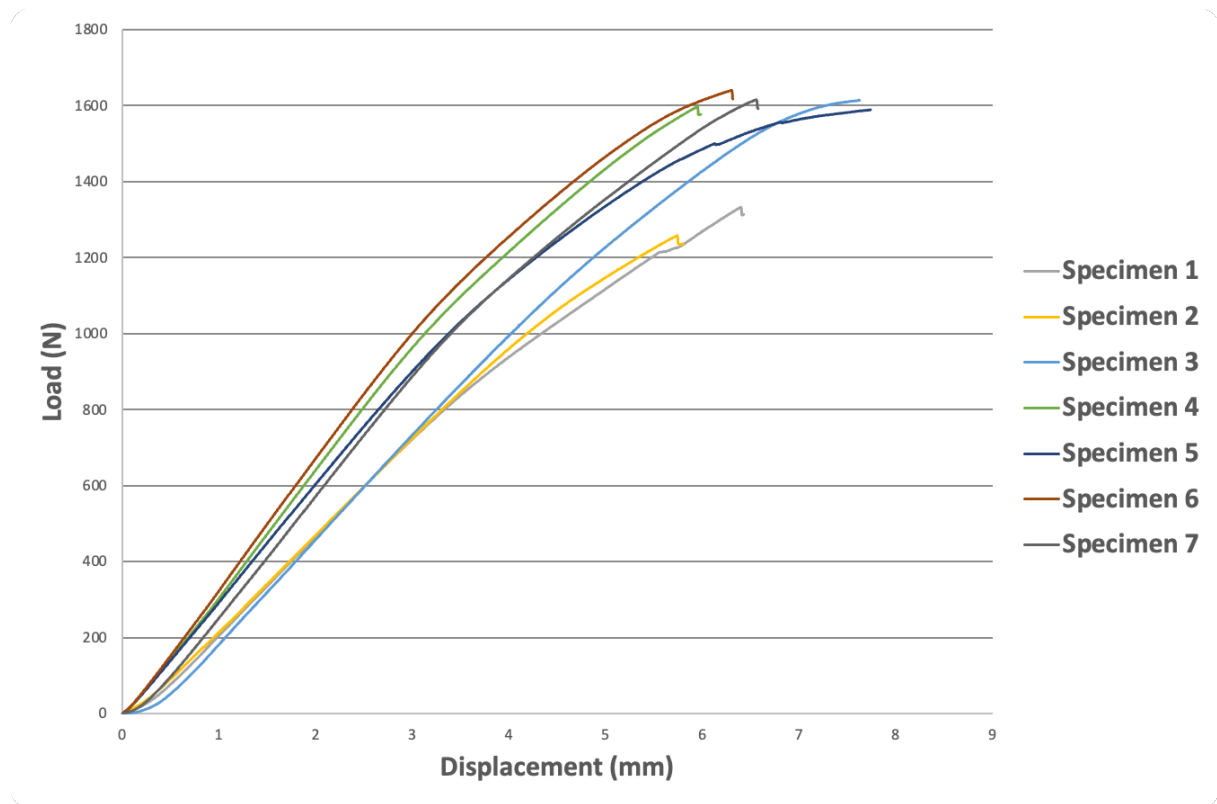


**Figure 4.9:** Load-Displacement curves of the ENF specimens.

Table 4.4 presents the individual and average  $G_{IIC}$  of thermoset hot press, Heated-VARTM, and thermoplastic hot stamping specimens. The results of the hot press ENF test a value of  $G_{IIC\ NPC} = 5.28 \pm 0.54 \text{ kJ/m}^2$  with a coefficient of variation of 10.34%. The obtained value of  $G_{IIC\ PC} = 5.12 \pm 0.32 \text{ kJ/m}^2$  with a coefficient of variation of 6.34%.



**Table 4.4:** NPC and PC interlaminar fracture toughness in mode II.

	Specimen	$G_{IIc}(\text{kJ/m}^2)$	
		NPC	PC
Thermoset hot press	1	4.37	5.19
	2	-	5.03
	3	5.73	5.61
	4	5.29	4.6
	5	5.08	-
	6	5.27	5.11
	7	5.93	5.18
	<b>Mean value</b>	5.28	5.12
	<b>STDV</b>	0.546	0.325
	<b>COV (%)</b>	10.34	6.34
Heated VARTM	1	5.12	4.51
	2	5.24	3.66
	3	4.48	-
	4	-	4.66
	5	5.16	4.27
	6	4.86	4.3
	<b>Mean value</b>	4.97	4.28
	<b>STDV</b>	0.311	0.381
	<b>COV (%)</b>	6.23	8.87
	Thermoplastic hot stamping	1	-
2		2.50	1.76
3		2.88	1.53
4		2.71	1.58
5		2.81	1.67
6		-	1.52
<b>Mean value</b>		2.73	1.61
<b>STDV</b>		0.165	0.102
<b>COV (%)</b>		6.04	6.33

Similar results were found in the case of the infusion test,  $G_{IIc\ NPC} = 4.97 \pm 0.31 \text{ kJ/m}^2$  with a coefficient of variation of 6.23%. The obtained value of  $G_{IIc\ PC} = 4.28 \pm 0.38 \text{ kJ/m}^2$  with a coefficient of variation of 8.87%.

The failure surfaces show a cohesive failure in the first two cases (Thermoset hot press and Heated-VARTM). In the case of thermoplastic hot stamping, the obtained values were lower than in the other cases; this can be explained by the fact that the failure was adhesive as illustrated in Figure 4.10, so it is more of an interface property than adhesive property.

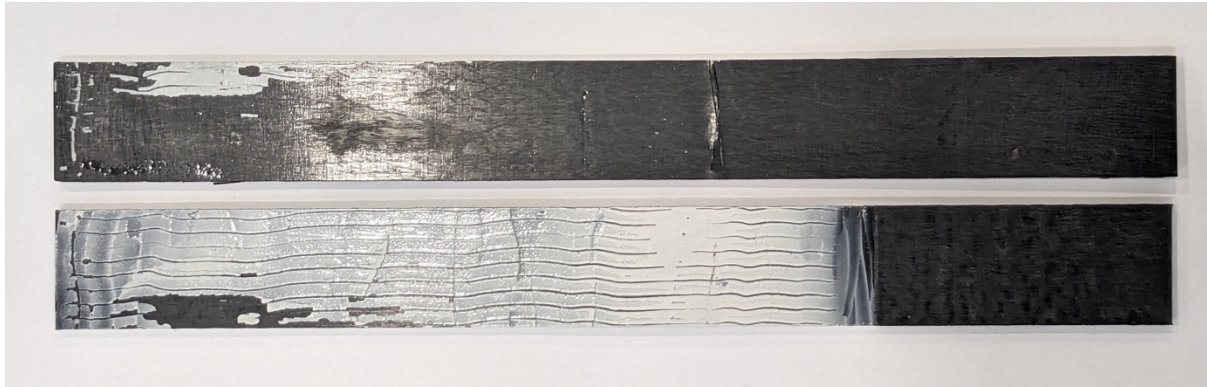


**Figure 4.10:** Adhesive failure of Thermoplastic specimen.

#### 4.5. Single-lap joints test

The results of the single lap joint experiments provide a clear idea of the performance and strength of various materials combinations and treatments. Table 4.5 shows the single lap joints test results.

In the case of the “Thermoplastic hot stamping/Thermoplastic hot stamping” combination, mechanical and chemical treatments of the surface were tested. The mechanical treatment specimens demonstrated adhesive failure, with maximum load values ranging from 8.71 kN to 10.47 kN. The chemical treatment specimens also experienced adhesive failure, Figure 4.11a, with maximum load values ranging from 4.14 kN to 5.49 kN. These results highlight the importance of considering the specific treatment method when working with a thermoplastic matrix, a treatment with thicker mesh sandpaper between 60 and 80 is recommended. In conclusion, mechanical and chemical treatments impact the strength of adhesive bonds.

**Table 4.5:** Single lap joint test results.

Combination	Specimen	Failure mode	Maximum Load [kN]	Average [kN]	STDV	COV (%)
<b>Thermoplastic hot stamping/ Thermoplastic hot stamping</b>	Mechanical treatment	P01	10.47	9.79	0.94	9.60
		P02	10.18			
		P03	8.71			
	Chemical treatment	P04	4.85	4.82	0.67	13.9
		P05	5.49			
		P06	4.14			
<b>Thermoset hot press / Thermoset hot press</b>	P19	Cohesive	16.61	15.25	0.84	5.50
	P20	Cohesive	15.01			
	P21	Cohesive	15.02			
	P24	Cohesive	14.06			
	P25	Cohesive	15.07			
	P26	Cohesive	15.62			
<b>Heated-VARTM / Thermoset hot press</b>	P27	Fibre tear	15.16	12.45	1.83	14.69
	P28	Fibre tear	12.29			
	P29	Fibre tear	12.39			
	P32	Fibre tear	10.19			
	P33	Fibre tear	13.82			
	P34	Fibre tear	10.87			
<b>Heated-VARTM / Heated-VARTM</b>	P35	Fibre tear	9	9.40	1.53	16.27
	P36	Fibre tear	8.74			
	P37	Fibre tear	8.39			
	P40	Fibre tear	10.61			
	P41	Fibre tear	7.77			
	P42	Fibre tear	11.86			
<b>Thermoplastic hot stamping / Heated-VARTM</b>	P43	Adhesive	5.83	5.67	0.57	10.05
	P44	Adhesive	6.2			
	P45	Adhesive	4.69			
	P46	Adhesive	5.72			
	P47	Adhesive	5.92			
<b>Thermoplastic hot stamping / Thermoset hot press</b>	P51	Adhesive	13.42	12.91	1.26	9.75
	P53	Adhesive	13.83			
	P54	Adhesive	14.41			
	P55	Adhesive	13.04			
	P56	Adhesive	11.47			
P57	Adhesive	11.31				

Cohesive failure was observed in all specimens for the “Thermoset hot press/Thermoset hot press” combination as illustrated in Figure 4.11b. The joints exhibited high maximum load values, ranging from 14.06 kN to 16.61 kN, with the highest average of 15.25 kN. This load indicates the strong bonding capacity of the thermoset hot press joints. The cohesive failure mode Figure 4.11b suggests that the joint maintained its integrity, with the failure occurring within the adhesive rather than at the interface.

In the case of the “heated VARTM/thermoset hot press” combination, the joints experienced fibre tear failure as illustrated in Figure 4.11bc. The maximum load values ranged from 10.19 kN to 15.16 kN. The average load values varied, indicating potential variations in joint quality. Fibre tear failure indicates that the applied load caused the fibres within the material to separate or tear, which may be an area of improvement for future designs or process modifications.

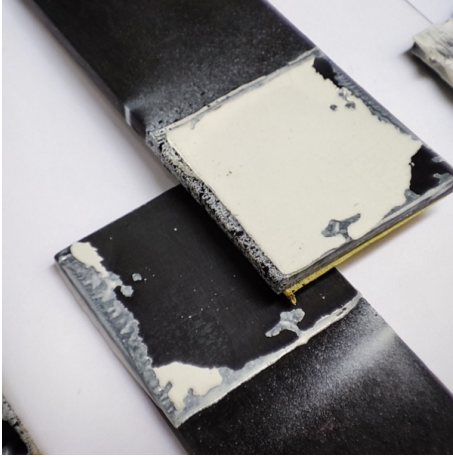
In the fourth combination, fibre tear failure was observed in all specimens for the “Heated-VARTM/Heated-VARTM”. The maximum load values ranged from 7.77 kN to 11.86 kN. These joints exhibited lower load-carrying capacities compared to the other combinations tested. This suggests that the heated-VARTM/heated-VARTM joints may benefit from further optimisation.

The combinations, namely "Thermoplastic hot stamping /heated-VARTM" and "Thermoplastic hot stamping/Thermoset hot press," reveal distinct adhesive failure behaviours.

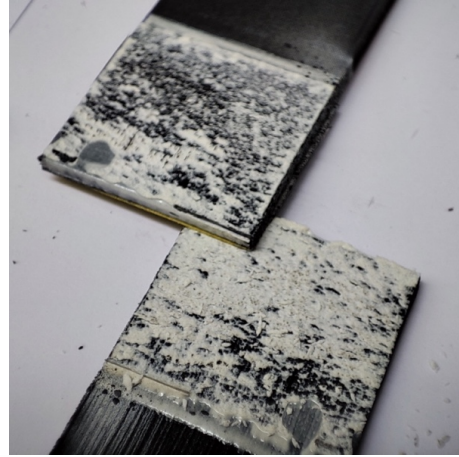
In the "Thermoplastic hot stamping/heated-VARTM" combination, adhesive failure was observed as the predominant mode of joint separation. The specimens displayed a maximum load of 5.83 kN, with an average load of 5.67 kN and a relatively low standard deviation of 0.57. This suggests a consistent adhesive bond strength among the specimens.

The "Thermoplastic hot stamping/Thermoset hot press" combination showcased adhesive failures with an interesting trend: a failure from the thermoplastic side. While the maximum load reached 14.41 kN and the average load was 12.91 kN, with a standard deviation of 1.26.

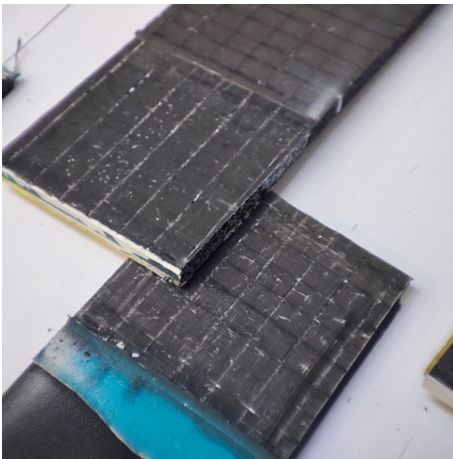
The variation in some results of the single lap joints, could stem from temperature and moisture changes, directly affecting adhesives' strength and mechanical properties. When the external environment changes, the width of the joint affect how fast the environment changes in the interior of the bondline.



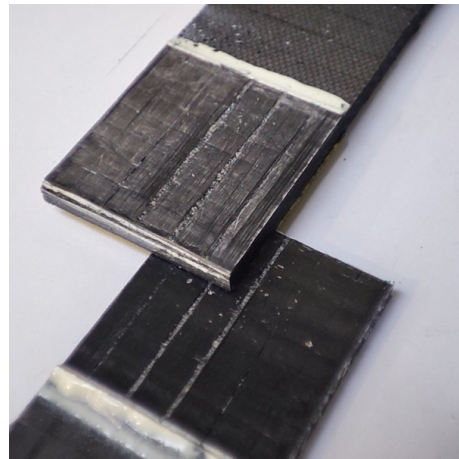
(a) Thermoplastic hot stamping/Thermoplastic hot stamping



(b) Thermoset hot press/Thermoset hot press



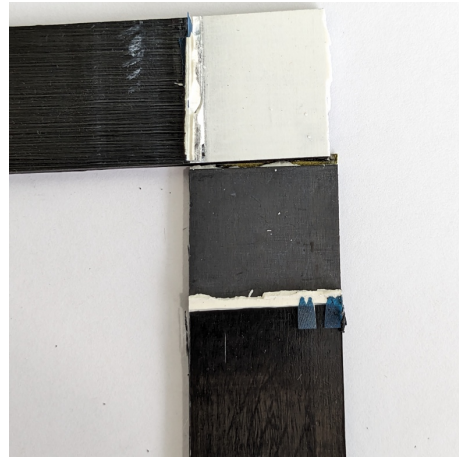
(c) Heated VARTM/Thermoset hot press



(d) Heated VARTM/ Heated VARTM



(e) Thermoplastic hot stamping /Heated VARTM



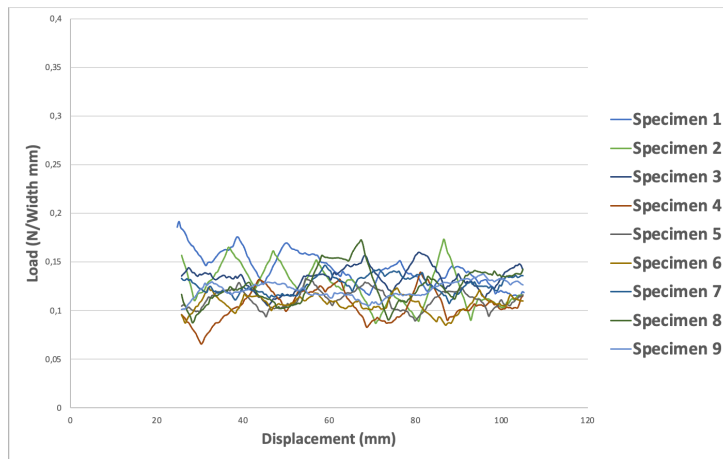
(f) Thermoplastic hot stamping / Thermoset hot press

**Figure 4.11:** Failure modes of SLJ specimens.

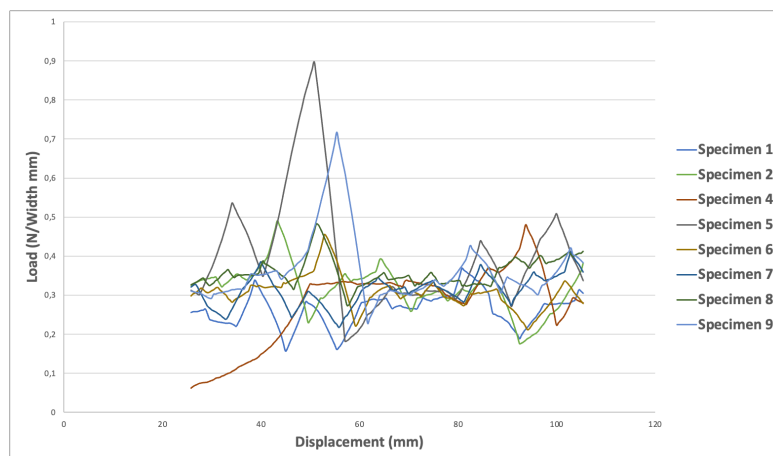
Overall, these results emphasise the influence of various factors, such as surface treatment method, the combination of materials, and manufacturing processes, on the strength and failure modes of single lap joints. By considering these results, the overall performance of adhesive joints can be improved by selecting the most appropriate materials, surface treatment method and manufacturing process.

#### 4.6. Floating roller peel test

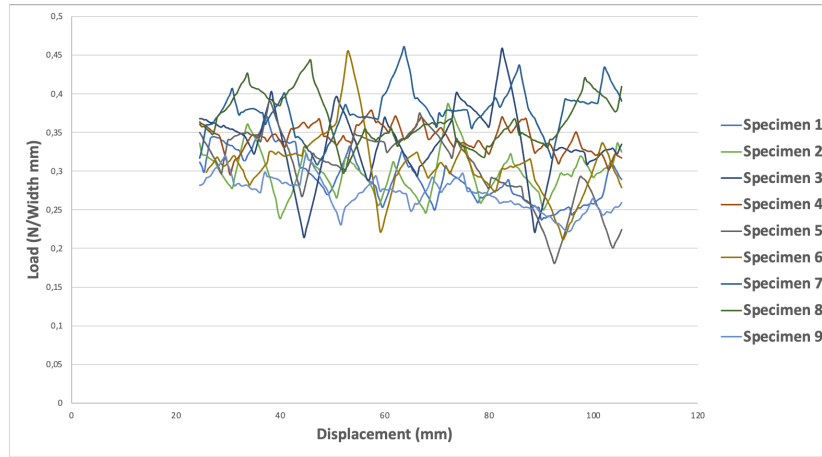
The initial crack of the specimens was short for clamping on the machine grips and had to be manually increased by pre-loading to enable testing [48]. For each material combination, the load-displacement curves were recorded during testing Figure 4.12a, b, c and d.



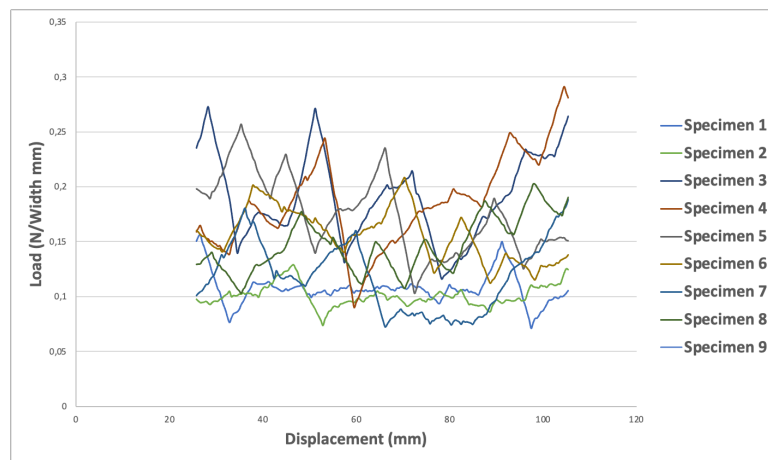
(a) Rigid heated VARTM/Flexible thermoplastic hot stamping.



(b) Rigid heated VARTM/Flexible thermoset hot press



(c) Rigid thermoset hot press/Flexible thermoset hot press.



(d) Rigid thermoset hot press/Flexible thermoplastic hot stamping.

**Figure 4.12:** Experimental  $P/b$  curves for each configuration.

In this work, the interval defined for obtaining the results was between the  $25.4\text{ mm}$  and the  $105.4\text{ mm}$  of crack propagation. This interval was selected because it complied with the recommendations of the standard. The calculation of  $P/b$  is done by averaging the measured force  $P$  during the tests by the specimen width  $b$ , at every point in the measurement range [47].

Table 4.6 presents the results for each combination, including the average  $P/b$  values, standard deviations and coefficient of variation. The minimum  $P/b$  is  $0.122\text{ N/mm}$  for the Heated VARTM/thermoplastic hot stamping configuration, and the maximum is  $0.327\text{ N/mm}$  for the Thermoset hot press/Thermoset hot press configuration, similar to the Heated VARTM/Thermoset hot press configuration, with a value of  $0.306\text{ N/mm}$ . In the case of Thermoset hot press/thermoplastic

hot stamping, the average peeling load was  $0.147 N/mm$  higher than the Heated VARTM/Thermoplastic hot stamping configuration and lower than the others.

**Table 4.6:** Floating roller test results

	Specimen	$P_{max}$ [N]	$P_{min}$ [N]	$P_{average}$ [N]	$\frac{P_{average}}{Width} [\frac{N}{mm}]$
Rigid heated VARTM/Flexible thermoplastic hot stamping	1	2.92	1.75	2.19	0.143
	2	2,60	1.30	1.89	0.126
	3	2.20	1.44	1.83	0.133
	4	2.09	0.97	1.57	0.106
	5	1.83	1.23	1.54	0.112
	6	1.85	1.27	1.60	0.107
	7	2.00	1.46	1.72	0.127
	8	2.60	1.32	1.88	0.125
	9	1.93	1.42	1.70	0.121
	<b>AVERAGE</b>	-	-	-	0.122
	<b>STDV</b>	-	-	-	0.0124
<b>COV (%)</b>	-	-	-	10.16	
Rigid heated VARTM/Flexible thermoset hot press	1	5.35	2.75	3.81	0.262
	2	7.09	2.55	4.61	0.318
	3	17.01	5.21	-	-
	4	6.97	0.9	4.01	0.276
	5	12.68	2.57	-	-
	6	6.73	3.13	4.55	0.307
	7	6.11	3.23	4.64	0.312
	8	7.04	4.00	5.23	0.358
	9	10.59	3.37	-	-
	<b>AVERAGE</b>	-	-	-	0.306
	<b>STDV</b>	-	-	-	0.033
<b>COV (%)</b>	-	-	-	10.78	
Rigid thermoset hot press/Flexible thermoset hot press	1	5.43	3.47	4.27	0.291
	2	5.75	3.53	4.43	0.298
	3	6.65	3.10	4.87	0.336
	4	5.63	3.38	5.09	0.342
	5	5.58	3.58	4.36	0.305
	6	6.27	4.42	5.25	0.356
	7	6.68	4.46	5.49	0.379
	8	6.13	4.10	5.06	0.366
	9	4.53	3.11	3.80	0.270
	<b>AVERAGE</b>	-	-	-	0.327
	<b>STDV</b>	-	-	-	0.037
<b>COV (%)</b>	-	-	-	11.31	
	1	2.36	1.07	1.61	0.107



## Chapter 4 | Experimental results

	<b>2</b>	1.94	1.11	1.52	0.101
	<b>3</b>	4.18	1.77	2.91	0.19
	<b>4</b>	4.43	1.37	2.82	0.185
<b>Rigid thermoset hot press/Flexible</b>	<b>5</b>	3.83	1.53	2.60	0.174
	<b>6</b>	3.11	1.67	2.33	0.156
<b>thermoplastic hot stamping</b>	<b>7</b>	2.82	1.08	1.78	0.118
	<b>8</b>	3.01	1.53	2.19	0.148
	<b>AVERAGE</b>	-	-	-	0.147
	<b>STDV</b>	-	-	-	0.035
	<b>COV (%)</b>	-	-	-	23.8

The coefficients of variation were calculated as 10.16 % for the Heated VARTM/thermoplastic hot stamping configuration, 10.78 % for the Heated-VARTM/Thermoset hot press configuration, and 11.31 % for the Thermoset hot press/Thermoset hot press configuration, which indicates good agreement between results. The coefficient of variation in the Thermoset hot press/thermoplastic hot stamping configuration was higher than the other cases.

THIS PAGE WAS INTENTIONALLY LEFT BLANK

## 5. NUMERICAL STUDY

The Numerical FE analysis was carried out using Abaqus® software to reproduce the experimental results. This software was chosen due to its integrated, cohesive zone model module, which allows for predicting the strength of the single-lap joints and peel of the tested adhesive joints.

### 5.1. Single lap joint

Two distinct modelling strategies are available for simulating single lap joint and peel tests: the 2D and 3D approaches. The first method uses 2D shells with elastic orthotropic properties to represent the adherends. These properties can be determined using A, B, and D matrices. For the adhesive, two options are available: cohesive elements with a traction-separation law or a continuum approach using bulk properties.

The second method uses 3D continuum shells to represent the adherends with the stacking sequence defined in the previous section. In this case, the material properties used are those of individual plies. A similar approach to the 2D model can be applied for the adhesive layer but with adding a 3D cohesive element instead of the 2D one. A third approach uses solid elements, but this strategy is computationally demanding.

#### *5.1.1. Modelling strategy*

The adherends were modelled using 3D solid, with the material properties of individual plies. The adhesive was modelled using a cohesive element (COH3D8), and geometrical non-linearities were considered. The joints were modelled as three-dimensional, with continuum shell elements (SC8R from ABAQUS®), with meshes constructed to reduce computational time while maintaining precision through bias effects towards specimen edges and adhesive layer thickness, as illustrated in Figure 5.1. The overlap region and cohesive elements were meshed using 0.02 mm × 0.02 mm elements, allowing to accurately capture stress variations these regions.

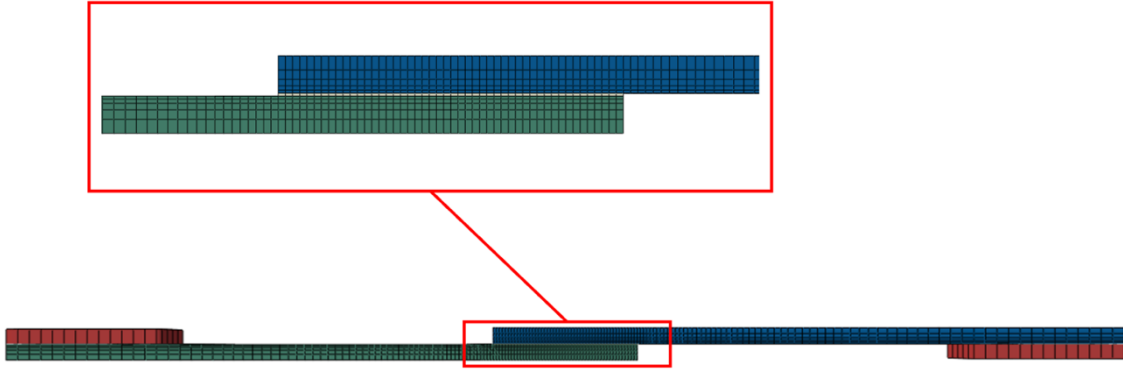


**Figure 5.1:** Detail of the mesh for the model.

Loading conditions were introduced to simulate the actual testing conditions, consisting of clamping the joint at one edge, which means that every degree of freedom is constrained, and applying horizontal displacement along the length direction of the specimen to the other edge, as illustrated in Figure 5.2. In the cohesive zone model analysis, the adhesive was modelled with a cohesive element using a traction separation law, as described in the previous section.

After running the model, we encountered convergence issues that should be addressed in future work.

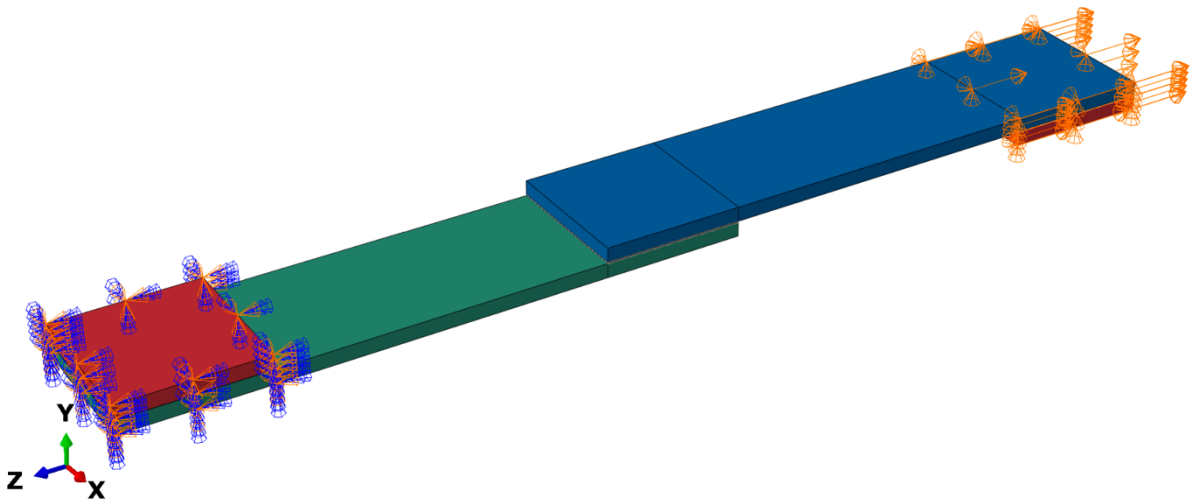


**Figure 5.2:** Boundary conditions.

## 5.2. Subcomponent model

The subcomponent model consists of two main stages. The first stage is performed before the test to identify the critical regions more likely to fail and define the LVDT positions. The second stage is carried

out after the test using a cohesive zone model to replicate the actual test. In this thesis, the first stage was performed using a linear analysis.

### 5.2.1. Test setup

The test sample is a portion of the fuselage composed of sections of the upper skin with stringers integrated, the frame, and a connector that connects the parts through bonded joints within defined contact areas between the CFRP parts surfaces, as illustrated Figure 5.3.

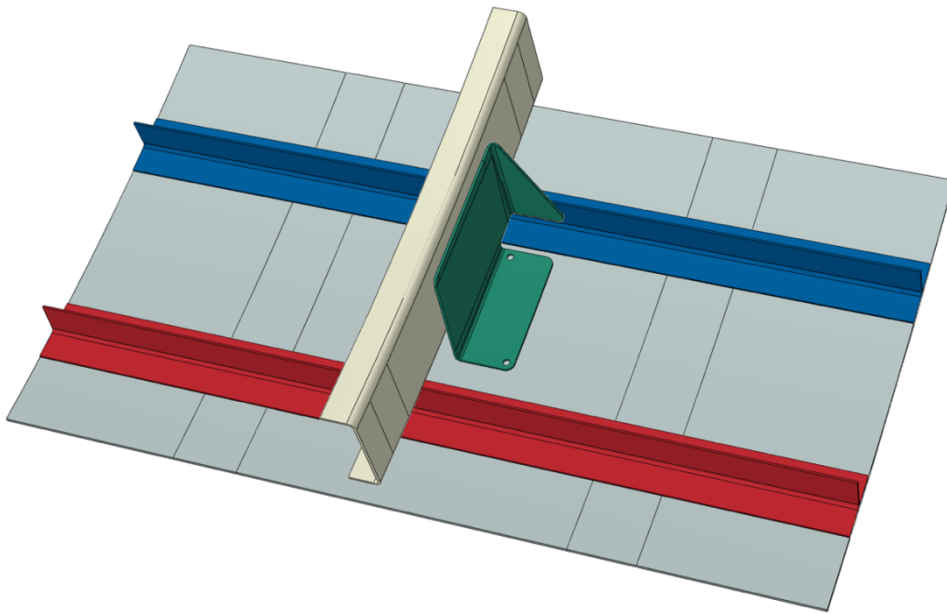


**Figure 5.3:** Test Specimen (CFRP part)

All three parts composing the test sample, frame, skin/stringers and connector, are made of Heated-VARTM material bonded with an epoxy adhesive. The frame and skin/stringers are produced by vacuum infusion using an epoxy resin matrix and layup of  $0^{\circ}/90^{\circ}$  and  $+45^{\circ}/-45^{\circ}$  tweel fabric plies. The connector is produced by hot stamping a carbon fibre UD plies with a thermoset matrix (see Table 5.1).

**Table 5.1:** Parts nominal thicknesses and stacking sequences.

Parts	Thickness [mm]	Material	Layup	Abaqus Layup
Frame	1.68	HiMax / RTM6	0°/90°/0°/90°/45°/-45°/-45°/45°/90°/0°	0°/0°/45°/-45°/0°
Connector	1.68	Thermoset DT120	0°/90°/0°/90°/45°/-45°/-45°/45°/90°/0°/90°/0°	0°/90°/0°/90°/45°/-45°/45°/45°/90°/0°/90°/0°
Skin	2.28	HiMax / RTM6	0°/90°/45°/-45°/0°/90°/90°/0°/-45°/45°/90°/0°	0°/45°/0°/0°/-45°/0°
Stringer	1.12	HiMax / RTM6	0°/90°/0°/90°/0°/90°/0°/90°	0°/0°/0°/0°

The test consists of pulling the frame vertically while the skin/stringers are fixed in the test bed. The specimen is fixed to the test bed by tight metallic fixtures, as illustrated in Figure 5.4. A thin rubber mat is used between the metallic fixture and the Skin/Stingers part to avoid damaging the CFRP parts and to account for the uncertainties of the CFRP thickness due to the manufacturing process. The load is applied by a hydraulic actuator, with a ball joint connected to a metallic fixture that is previously tied to the frame. The test setup ensures the relative positioning of the sample and actuator axis to ensure the load is applied with the actuator axis passing through a predefined point at the sample in the defined direction (see figure 4).

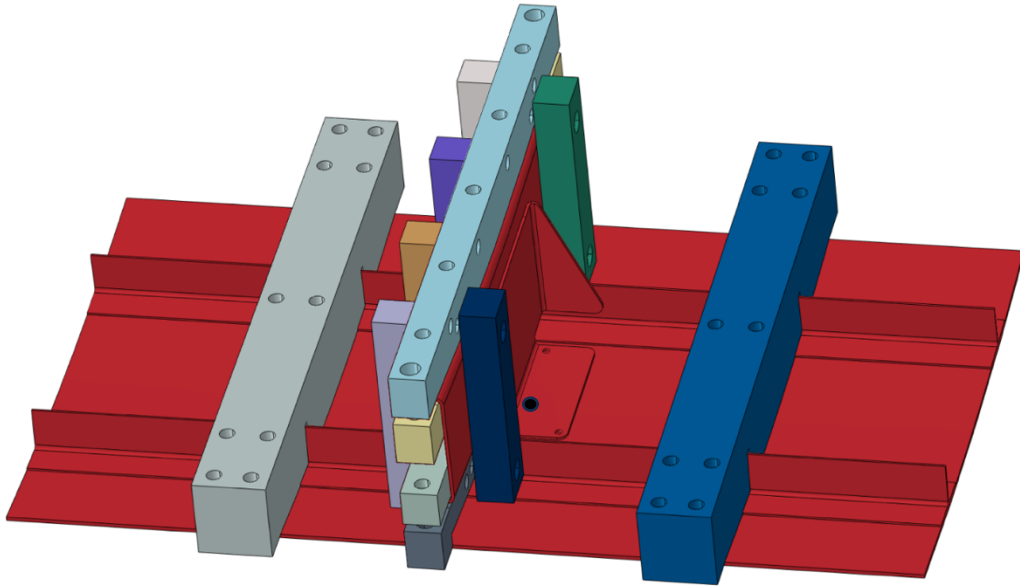


**Figure 5.4:** Representation of the test fixtures tight to the Frame and Skin/Stringers and load application point.

### 5.2.2. *Materials definition*

After drawing all the parts, laminate definitions were created using the "create composite layup" option in ABAQUS®. It is worth mentioning that this model features curved parts, so we used a discrete orientation method to define the material orientation accurately as in real applications, Figure shows the material orientation of the frame. The Hashin damage criterion was introduced for indication purposes in this model since it is defined without the damage evolution model.

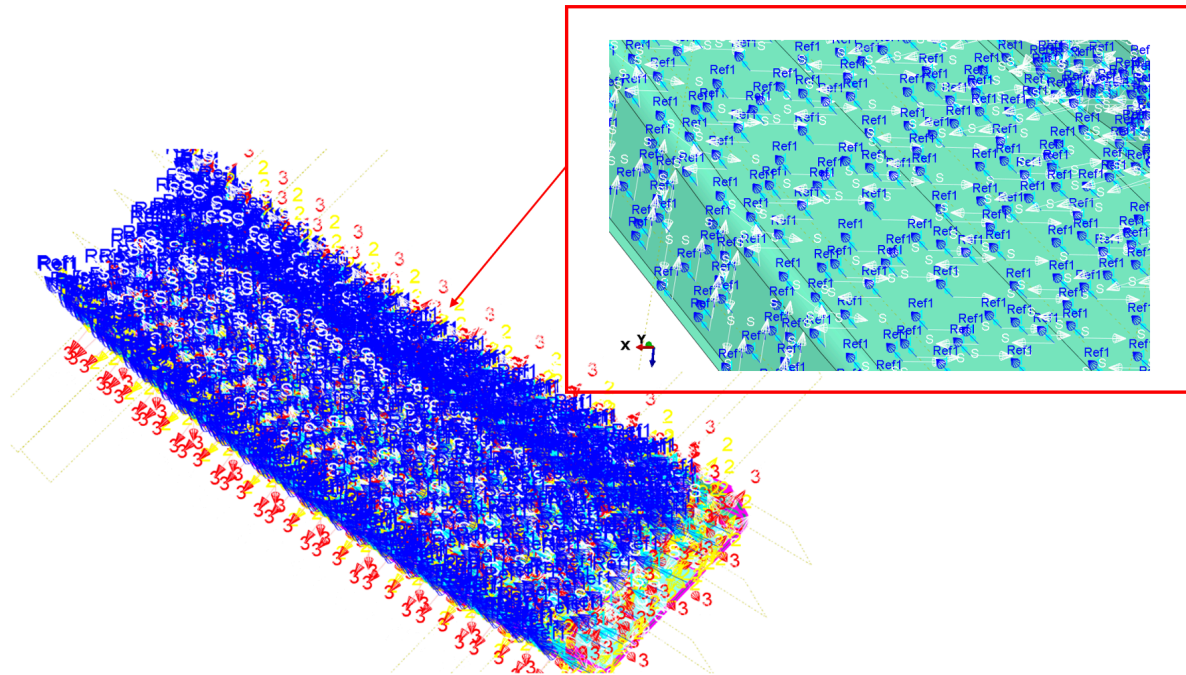


**Figure 5.5:** Frame Material orientation.

The mechanical properties of the materials used in the model are presented in Table 5.2.

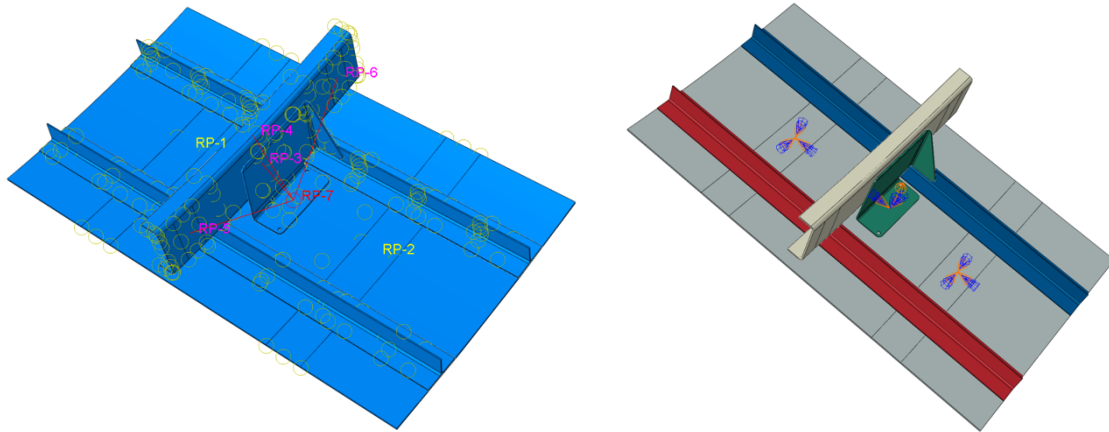
**Table 5.2:** Material Properties.

Properties	HiMax/RTM6	Thermoset DT120
$E_{11}$ [MPa]	74000	140000
$E_{22}$ [MPa]	74000	5000
$\nu_{12}$	0.04	0.36
$G_{12}$ [MPa]	3100	3200
$G_{23}$ [MPa]	761	1760

### 5.2.3. Boundary condition

The boundary conditions were applied to simulate the actual testing scenario. All subcomponents have been connected by means of TIE constraints. The fixtures were considered rigid enough and were non-deformable during the test. Therefore, rigid body constraints were defined (RP1 to RP6) with a tie node to constrain the regions in direct contact with the fixtures. The load was applied on a reference point (RP7) connected to (RP3) to (RP6) through a kinematic coupling, as illustrated in Figure 5.6. An imposed displacement of 3mm was applied in this stage to determine the critical regions.





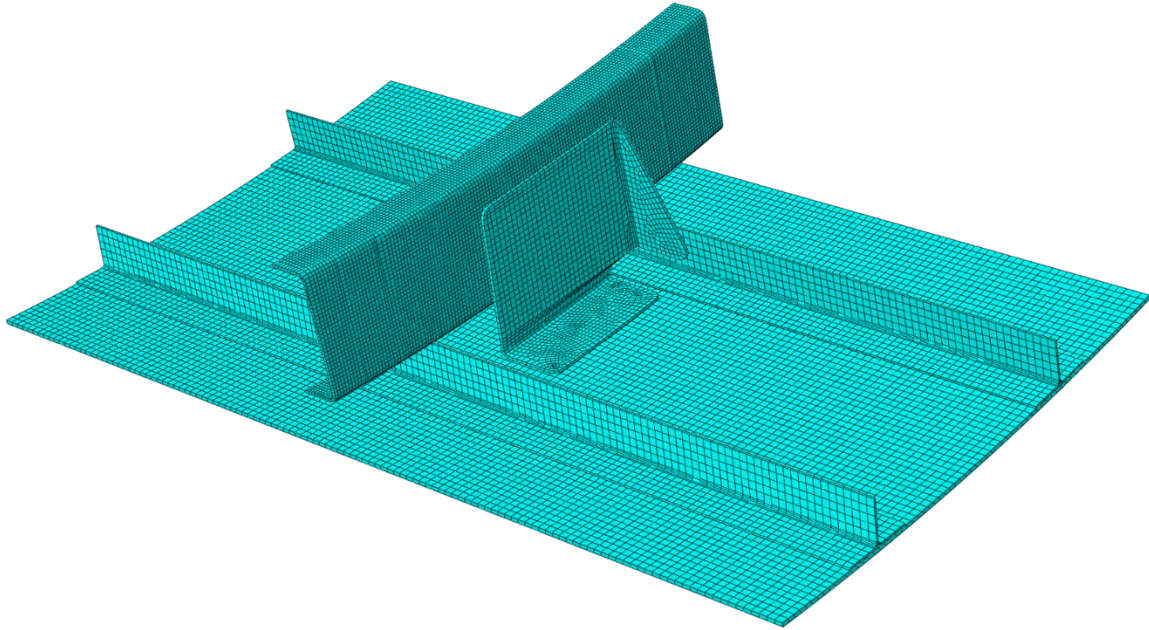
(a) Constraint

(b) Boundary conditions

**Figure 5.6:** Boundary condition and constraint applied to the panel.

#### 5.2.4. Mesh

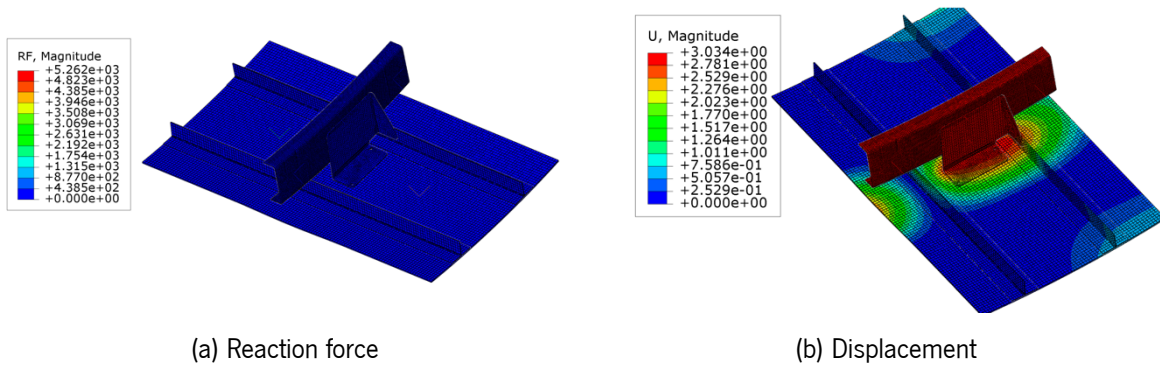
The composite panel has been discretized by means of continuum shell elements (SC8R) with a reduced integration scheme. an element size of 2 mm was employed to model the skin, stringers, and connector, and 1 mm for the Frame. In the case of the connector, it was very challenging to have a structural mesh, so partitioning was needed to obtain an acceptable mesh to avoid compromising the results, as illustrated in Figure 5.7.



**Figure 5.7:** Detail of the mesh.

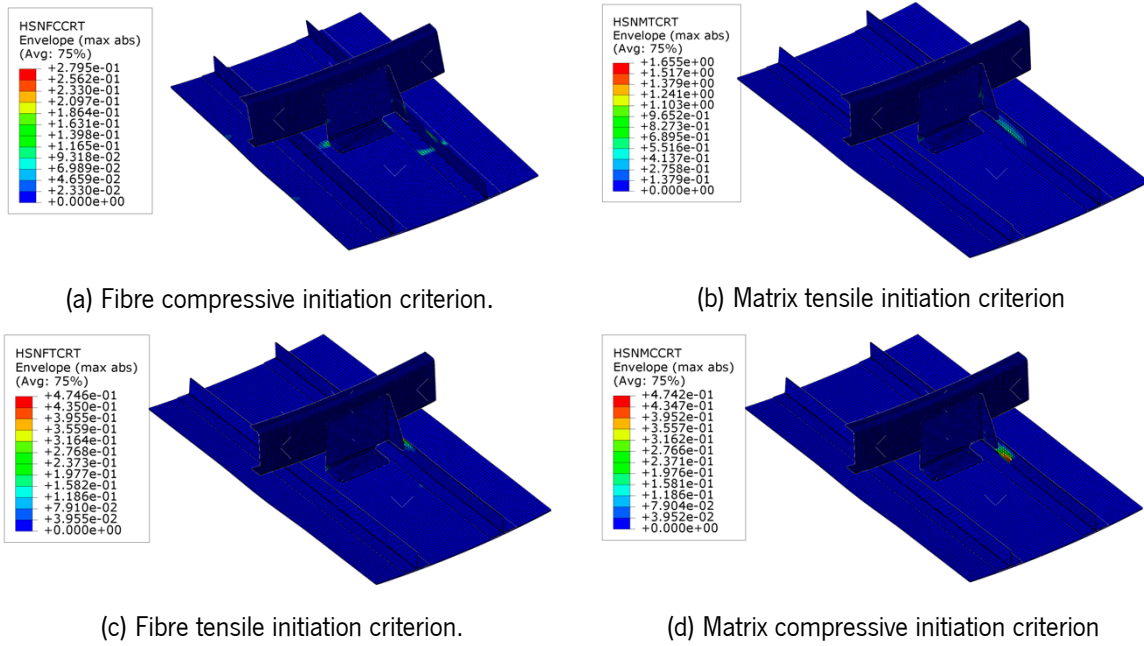
### 5.3. Numerical results

Figure 5.8 shows that the displacement at the end of the model is the same in the frame, proving that the load was applied correctly.



**Figure 5.8:** Reaction forces and the imposed load.

In this model, the Hashin damage criterion was defined to have an initial understanding of the panel's behaviour. However, it should be noted that this criterion is not entirely representative as it is not correlated with the damage evolution model. The results indicate matrix tension failure, as shown in Figure 5.9. It is worth mentioning that the value of HSNMTCRT was 1.65, meaning a satisfaction of the matrix tensile initiation criterion. The maximum force registered at the initiation ( $HSNMTCRT = 1$ ) was 5.2kN, as illustrated Figure 5.9.



**Figure 5.9:** Hashin damage criterion.

The values of stress components reached at the end of the analysis  $S_{11} = 1069MPa$  and  $S_{22} = 452MPa$ . By analysing the distribution of stress and damage values across the panel, it becomes evident that the areas where failure is likely to occur first are concentrated around the connector, as shown in Figure 5.10.

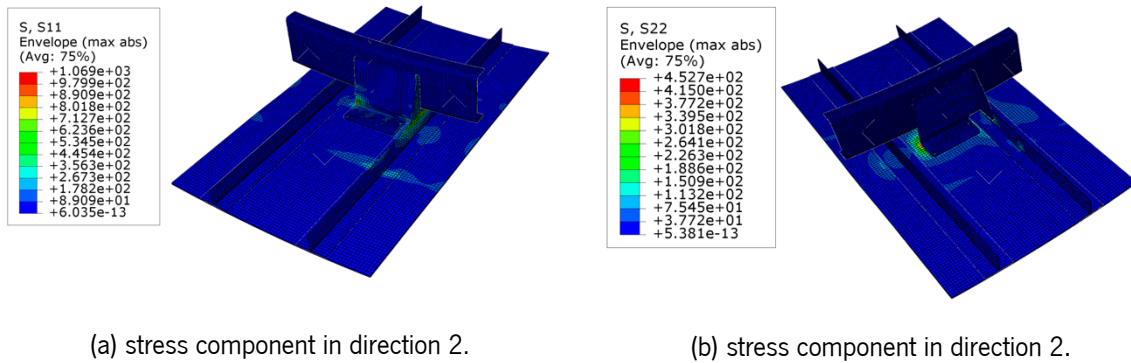


**Figure 5.10:** Stress Distribution.

THIS PAGE WAS INTENTIONALLY LEFT BLANK

## 6. CONCLUSIONS AND FURTHER DEVELOPMENTS

### 6.1. Main conclusions

This work aims to characterise the mechanical and fracture properties of adhesive carbon composite joints. Innovative out-of-autoclave manufacturing processes were employed to produce high-performance carbon composites designed to meet the stringent quality standards required in the aeronautical sector. Given the increasing demand for aircraft production, this research contributes significantly to a crucial area of study.

Developing alternative manufacturing processes to replace the conventional autoclave method is essential for producing more cost-effective, faster-produced, and environmentally friendly composites. In this study, carbon composites were manufactured using heated vacuum-assisted resin transfer moulding (heated-VARTM) and two variations of stamping. Both thermoset and thermoplastic matrices were considered, resulting in three types of carbon composites.

In the initial phase of this research, experimental characterization of 3M™ Scotch-Weld™ (EC-9323) epoxy adhesive was conducted. Four distinct tests were carried out: i. bulk tensile test, ii. thick adherend shear test, iii. double-cantilever beam test, and iv. end-notched flexure test. For the last two tests, the three aforementioned types of composites were employed as adherents to assess the impact of composite material on mode I and mode II fracture toughness.

In the subsequent phase of the study, the single-lap shear bond and peel strengths of composite-to-composite adhesive joints were experimentally characterised. Various combinations of composites were bonded using 3M™ Scotch-Weld™ (EC-9323) epoxy adhesive.

Through the bulk tensile tests it was possible to obtain the next tensile properties of 3M™ Scotch-Weld™ (EC-9323):  $E = 1275 \pm 88.89$  MPa,  $\sigma_f = 27.53 \pm 1.36$  MPa, and  $\varepsilon_f = 4.54 \pm 0.79\%$ . A slight difference was found in failure strain, explained by the presence of defects in the specimens that could compromise the full plasticity of the specimen to develop. It was not possible to compare these obtained results with information from the manufacturer's datasheet as such data was unavailable.

Shear properties were obtained using TAST test:  $G = 308 \pm 15.7$  MPa,  $\tau_f = 28.08 \pm 0.92$  MPa, and  $\gamma_f = 28 \pm 3.2\%$ . A good agreement was found between the value of  $\tau_f$  given by the manufacturer (27 MPa) and the one determined by the TAST test. However, no information was given by the manufacturer regarding the remaining properties.

To characterise  $G_{IC}$ , three types of specimens were tested: Thermoset hot press, Heated-VARTM, and thermoplastic hot stamping. In the case of heated-VARTM specimens, the crack initiation occurred within the adhesive, progressing cohesively. The failure mode transitioned to a fibre tear within the adherend. The  $G_{IC}$  values, obtained by heated-VARTM DCB tests, are  $1247 \pm 217$  J/m<sup>2</sup> (CBT),  $1392 \pm 105$  J/m<sup>2</sup> (ECM) and  $1302 \pm 163$  J/m<sup>2</sup> (CCM) for the NPC test, and  $1537 \pm 163$  J/m<sup>2</sup> (CBT),  $1699 \pm 286$  J/m<sup>2</sup> (ECM) and  $1681 \pm 309$  J/m<sup>2</sup> (CCM) for the PC test. The thermoplastic hot stamping specimens consistently showed adhesive-based failure, characterised by developing crack patterns distinct from those observed in thermoset hot press specimens. Despite the relatively smooth crack propagation, instability occurred at the crack onset, with crack lengths exceeding 5mm. To conclude, it is essential to exercise caution when interpreting results derived from this test. The  $G_{IC}$  values, obtained by thermoplastic hot stamping DCB tests, are  $59.55 \pm 10$  J/m<sup>2</sup> (CBT),  $67.68 \pm 19.28$  J/m<sup>2</sup> (ECM) and  $59.8 \pm 11.84$  J/m<sup>2</sup> (CCM) for the NPC test and  $67.5 \pm 11.42$  J/m<sup>2</sup> (CBT),  $73.7 \pm 19.85$  J/m<sup>2</sup> (ECM) and  $86.8 \pm 31.01$  J/m<sup>2</sup> (CCM) for the PC test. The coefficient of variations demonstrates a noticeable variability in results in the case of thermoplastic hot stamping specimens that can be related to the unstable crack propagation and the adhesive failure. Parallel to these results, the thermoset hot press specimens exhibited an adhesive failure, with unstable crack propagation accompanied with a big drop in load displacement curve, which led us to non-valid test.

ENF test is a reliable method to characterise  $G_{IIC}$ . This property was estimated using CCM method. The thermoset hot press ENF test results gave a value of  $G_{IIC NPC} = 5.28 \pm 0.54$  kJ/m<sup>2</sup> and  $G_{IIC PC} = 5.12 \pm 0.32$  kJ/m<sup>2</sup>. In the case of the Heated-VARTM test,  $G_{IIC NPC} = 4.97 \pm 0.31$  kJ/m<sup>2</sup> and  $G_{IIC PC} = 4.28 \pm 0.38$  kJ/m<sup>2</sup>. In the case of thermoplastic, the obtained values were  $G_{IIC NPC} = 2.73 \pm 0.165$  kJ/m<sup>2</sup> and  $G_{IIC PC} = 1.61 \pm 0.102$  kJ/m<sup>2</sup> lower than in the other cases. A cohesive failure was experienced in the case of Heated-VARTM and Thermoplastic hot press. However, thermoplastic hot stamping specimens experienced adhesive failure, which can explain the lower value of  $G_{IIC}$ .

For the single lap joints test, six combinations of composites were tested: Thermoplastic hot stamping/Thermoplastic hot stamping, Thermoset hot press/Thermoset hot press, Heated-

VARTM/Thermoset hot press, Heated-VARTM/Heated-VARTM, Thermoplastic hot stamping/Heated-VARTM, and Thermoplastic hot stamping/Thermoset hot press. In the present work, the bond strength and failure modes of different material combinations was evaluated.

Thermoset hot press/Thermoset hot press combination exhibited highest maximum load values, ranging from 14.06 kN to 16.61 kN, with the highest average of 15.25 kN, coupled with cohesive failure. In contrast, the Thermoplastic hot stamping/Heated VARTM combination had the lowest maximum load with a value of 5.67 kN. This load indicates the strong bonding capacity of the Thermoset hot press/Thermoset hot press joints. For the thermoplastic hot stamping/thermoplastic hot stamping combination, mechanical and chemical treatments of surfaces were tested. Both treatments led to adhesive failure, with a maximum load of 9.79 kN and 4.82 kN, respectively, highlighting the importance of considering a specific treatment method when working with a thermoplastic matrix. Both Heated-VARTM/Thermoset hot press and Thermoplastic hot stamping/Thermoset hot press joints exhibited maximum loads of 12.45 kN and 12.91 kN, respectively, while also displaying differing failure modes – the former experiencing fibre tear and the latter encountering adhesive failure. Finally, during Heated-VARTM/Heated VARTM, fibre tear failure was observed in all specimens. These joints exhibited lower load-carrying capacities compared to the other combinations tested.

The Heated-VARTM/Thermoset hot press combination and the Heated-VARTM /Heated-VARTM had a fibre tear failure, a phenomenon expected in the Thermoplastic hot stamping/Heated-VARTM combination. This result was predicted due to the higher load (12.91 kN) associated with the thermoplastic adherend in the Thermoplastic hot stamping/Thermoset hot press combination, comparable to the loads in Heated-VARTM/Thermoset hot press and Heated-VARTM/Heated-VARTM combinations. However, contrary to expectations, the thermoplastic/Heated-VARTM combination exhibited adhesive failure at a lower load. This finding further emphasises the significance of the surface treatment method in achieving successful composite bonding.

In general, treatment methods significantly impact joint strength and failure modes. Specifically, mechanical treatment has significantly improved thermoplastic bonding compared to chemical treatment. Moreover, cohesive failure in thermoset hot press/thermoset hot press joints demonstrated strong bonding. However, it's worth mentioning that certain joints involving Heated-VARTM laminates exhibit fibre tear failures, which highlight specific areas requiring improvement. Additionally, environmental factors, such as temperature and moisture, notably influence joint strength.

The floating roller peel test method was used to study four composite-composite joint combinations under peel loading: Rigid heated VARTM/Flexile thermoplastic hot stamping, Rigid heated VARTM/Flexible thermoset hot press, Rigid thermoset hot press/Flexible thermoset hot press, and Rigid thermoset hot press/Flexible thermoplastic hot stamping. The results revealed a range of average P/b values, from a minimum of  $0.122\pm 0.0124$  N/mm in Rigid heated VARTM/Flexile thermoplastic hot stamping configuration to a maximum of  $0.327\pm 0.037$  N/mm in the Rigid thermoset hot press/Flexible thermoset hot press. In the case of Heated-VARTM/Thermoset hot press configuration, the test gave a value of  $0.306\pm 0.033$  N/mm. Moreover, in the thermoset hot press/thermoplastic case, the average peeling load was  $0.147\pm 0.035$  N/mm higher than the Heated-VARTM/thermoplastic hot stamping configuration and lower than the remaining configurations.

The linear analysis of the subcomponent model has provided a clear idea of the critical region, notably centred around the connector. Moreover, the identified convergence issues within the single lap joint highlight an area for improvement in future work.

## 6.2. Further developments

This study has provided a practical understanding of the mechanical and fracture properties of adhesive carbon composite joints. Still, several avenues remain for future research and improvement in this field.

1. Surface Treatment Enhancement for DCB Tests: The results from the Double Cantilever Beam (DCB) tests have demonstrated the need for further investigation into surface treatment methods. A more thorough exploration of surface treatments could enhance the reliability and consistency of DCB test results, ensuring a more accurate characterisation of fracture toughness.
2. Completion of numerical analysis: The numerical modelling aspect of this research is an ongoing endeavour. The numerical simulations must be finalised, particularly those related to single lap joints. Further refinement and validation of the numerical models will contribute to a deeper understanding of composite joint behaviour.
3. Convergence solutions for single lap joints: Convergence issues in numerical simulations of single lap joints were encountered during this study. Future work should focus on developing effective solutions to address these convergence challenges, ensuring the accuracy and reliability of numerical predictions.



4. Development of peel test models: Building numerical models for the floating roller peel tests should be a priority for future research. These models can help predict and understand the peeling behaviour of composite-to-composite joints, providing an understanding of adhesive performance under different loading conditions.
5. Cohesive Zone Modelling for subcomponent test: Future work should prioritize the creation of subcomponent models using cohesive zone modelling techniques. These models can accurately reproduce the observed behaviour in the experimental test.

THIS PAGE WAS INTENTIONALLY LEFT BLANK

### References

- [1] I. Martín, K. Fernández, J. Cuenca, C. Sánchez, S. Anaya, and R. Élices, 'Design and manufacture of a reinforced fuselage structure through automatic laying-up and in-situ consolidation with co-consolidation of skin and stringers using thermoplastic composite materials', *Heliyon*, vol. 9, no. 1, Jan. 2023, doi: 10.1016/j.heliyon.2022.e12728.
- [2] J. Kupski and S. Teixeira de Freitas, 'Design of adhesively bonded lap joints with laminated CFRP adherends: Review, challenges and new opportunities for aerospace structures', *Compos Struct*, vol. 268, Jul. 2021, doi: 10.1016/j.compstruct.2021.113923.
- [3] R. BIELAWSKI, 'COMPOSITE MATERIALS IN MILITARY AVIATION AND SELECTED PROBLEMS WITH IMPLEMENTATION', *Review of the Air Force Academy*, vol. 15, no. 1, pp. 11–16, May 2017, doi: 10.19062/1842-9238.2017.15.1.2.
- [4] R. B. Heslehurst, *Design and analysis of structural joints with composite materials / Rikard Benton Heslehurst*. DEStech Publications, 2013.
- [5] A. Daniel and G. Gay, *Design and Applications*. [Online]. Available: [www.taylorandfrancisgroup.com](http://www.taylorandfrancisgroup.com)
- [6] M. D. Banea and L. F. M. Da Silva, 'Adhesively bonded joints in composite materials: An overview', *Proceedings of the Institution of Mechanical Engineers, Part L: Journal of Materials: Design and Applications*, vol. 223, no. 1. pp. 1–18, Jan. 01, 2009. doi: 10.1243/14644207JMDA219.
- [7] M. Kazemi, S. Faisal Kabir, and E. H. Fini, 'State of the art in recycling waste thermoplastics and thermosets and their applications in construction', *Resources, Conservation and Recycling*, vol. 174. Elsevier B.V., Nov. 01, 2021. doi: 10.1016/j.resconrec.2021.105776.
- [8] U. Vaidya, 'Thermoplastic composites for aerospace applications', vol. 52, pp. 41–44, Apr. 2015.
- [9] C. Meola *et al.*, 'New perspectives on impact damaging of thermoset- and thermoplastic-matrix composites from thermographic images', *Compos Struct*, vol. 152, pp. 746–754, May 2016, doi: 10.1016/j.compstruct.2016.05.083.
- [10] "Composites Used in the Aerospace Industry" <https://www.azom.com/article.aspx?ArticleID=8152> (accessed Feb. 22, 2023).'
- [11] P. Hubert, T. Centea, L. Grunefelder, S. Nutt, J. Kratz, and A. Levy, 'Out-of-Autoclave Prepreg Processing. In *Comprehensive Composite Materials II*', 2nd ed. Elsevier, 2018, pp. 63–94.
- [12] T. Centea, L. K. Grunenfelder, and S. R. Nutt, 'A review of out-of-autoclave prepregs - Material properties, process phenomena, and manufacturing considerations', *Composites Part A: Applied*

## References

---

- Science and Manufacturing*, vol. 70. Elsevier Ltd, pp. 132–154, 2015. doi: 10.1016/j.compositesa.2014.09.029.
- [13] H. Chen, S. Li, J. Wang, and A. Ding, 'A focused review on the thermo-stamping process and simulation progresses of continuous fibre reinforced thermoplastic composites', *Composites Part B: Engineering*, vol. 224. Elsevier Ltd, Nov. 01, 2021. doi: 10.1016/j.compositesb.2021.109196.
- [14] U. K. Vaidya and K. K. Chawla, 'Processing of fibre reinforced thermoplastic composites', *International Materials Reviews*, vol. 53, no. 4, pp. 185–218, Jul. 2008, doi: 10.1179/174328008X325223.
- [15] M. D. Banea, L. F. M. Da Silva, and R. D. S. G. Campilho, 'The effect of adhesive thickness on the mechanical behavior of a structural polyurethane adhesive', *Journal of Adhesion*, vol. 91, no. 5, pp. 331–346, Jan. 2014, doi: 10.1080/00218464.2014.903802.
- [16] S. Marzi, A. Biel, and U. Stigh, 'On experimental methods to investigate the effect of layer thickness on the fracture behavior of adhesively bonded joints', *Int J Adhes Adhes*, vol. 31, no. 8, pp. 840–850, Dec. 2011, doi: 10.1016/j.ijadhadh.2011.08.004.
- [17] R. Lopes Fernandes, S. Teixeira de Freitas, M. K. Budzik, J. A. Poulis, and R. Benedictus, 'From thin to extra-thick adhesive layer thicknesses: Fracture of bonded joints under mode I loading conditions', *Eng Fract Mech*, vol. 218, Sep. 2019, doi: 10.1016/j.engfracmech.2019.106607.
- [18] T. Carlberger and U. Stigh, 'Influence of layer thickness on cohesive properties of an epoxy-based adhesive-an experimental study', *Journal of Adhesion*, vol. 86, no. 8, pp. 816–835, 2010, doi: 10.1080/00218464.2010.498718.
- [19] V. Cooper, A. Ivankovic, A. Karac, D. McAuliffe, and N. Murphy, 'Effects of bond gap thickness on the fracture of nano-toughened epoxy adhesive joints', *Polymer (Guildf)*, vol. 53, no. 24, pp. 5540–5553, Nov. 2012, doi: 10.1016/j.polymer.2012.09.049.
- [20] C. Sarrado, A. Turon, J. Costa, and J. Renart, 'An experimental analysis of the fracture behavior of composite bonded joints in terms of cohesive laws', *Compos Part A Appl Sci Manuf*, vol. 90, pp. 234–242, Nov. 2016, doi: 10.1016/j.compositesa.2016.07.004.
- [21] T. M. S. Faneco, R. D. S. G. Campilho, F. J. G. Silva, and R. M. Lopes, 'Strength and fracture characterization of a novel polyurethane adhesive for the automotive industry', *J Test Eval*, vol. 45, no. 2, pp. 398–407, 2017, doi: 10.1520/JTE20150335.
- [22] M. D. Banea, L. F. M. Da Silva, and R. D. S. G. Campilho, 'Moulds design for adhesive bulk and joint specimens manufacturing', *Assembly Automation*, vol. 32, no. 3, pp. 284–292, 2012, doi: 10.1108/01445151211244456.

## References

---

- [23] M. D. Banea and L. F. M. da Silva, 'Mechanical characterization of flexible adhesives', in *Journal of Adhesion*, 2009, pp. 261–285. doi: 10.1080/00218460902881808.
- [24] 'from IHS', 2001. [Online]. Available: [www.iso.ch](http://www.iso.ch)
- [25] R. M. Lopes, R. D. S. G. Campilho, F. J. G. Da Silva, and T. M. S. Faneco, 'Comparative evaluation of the Double-Cantilever Beam and Tapered Double-Cantilever Beam tests for estimation of the tensile fracture toughness of adhesive joints', *Int J Adhes Adhes*, vol. 67, pp. 103–111, Jun. 2016, doi: 10.1016/j.ijadhadh.2015.12.032.
- [26] Z. Wang and G. Xian, 'Cohesive zone model prediction of debonding failure in CFRP-to-steel bonded interface with a ductile adhesive', *Compos Sci Technol*, vol. 230, Nov. 2022, doi: 10.1016/j.compscitech.2022.109315.
- [27] A. Turon, P. P. Camanho, A. Soto, and E. V. González, 'Analysis of delamination damage in composite structures using cohesive elements', in *Comprehensive Composite Materials II*, Elsevier, 2017, pp. 136–156. doi: 10.1016/B978-0-12-803581-8.10059-1.
- [28] L. M. Fernández-Cañadas, I. Ivañez, S. Sanchez-Saez, and E. J. Barbero, 'Effect of adhesive thickness and overlap on the behavior of composite single-lap joints', *Mechanics of Advanced Materials and Structures*, vol. 28, no. 11, pp. 1111–1120, 2021, doi: 10.1080/15376494.2019.1639086.
- [29] 'ABAQUS 6.14 ABAQUS/CAE USER'S GUIDE', 2014.
- [30] J. A. B. P. Neto, R. D. S. G. Campilho, and L. F. M. Da Silva, 'Parametric study of adhesive joints with composites', in *International Journal of Adhesion and Adhesives*, Sep. 2012, pp. 96–101. doi: 10.1016/j.ijadhadh.2012.01.019.
- [31] A. J. S. Leal, R. D. S. G. Campilho, F. J. G. Silva, D. F. O. Silva, and F. J. P. Moreira, 'Comparison of different test configurations for the shear fracture toughness evaluation of a ductile adhesive', in *Procedia Manufacturing*, Elsevier B.V., 2019, pp. 940–947. doi: 10.1016/j.promfg.2020.01.177.
- [32] R. D. S. G. Campilho, M. D. Banea, J. A. B. P. Neto, and L. F. M. Da Silva, 'Modelling adhesive joints with cohesive zone models: Effect of the cohesive law shape of the adhesive layer', *Int J Adhes Adhes*, vol. 44, pp. 48–56, 2013, doi: 10.1016/j.ijadhadh.2013.02.006.
- [33] T. F. C. Pereira, R. D. S. G. Campilho, R. J. B. Rocha, and I. J. Sánchez-Arce, 'Cohesive zone parameter influence on the impact strength of composite adhesive joints', in *Procedia Structural Integrity*, Elsevier B.V., 2022, pp. 14–23. doi: 10.1016/j.prostr.2022.05.004.

## References

---

- [34] L. Sun, Y. Tie, Y. Hou, X. Lu, and C. Li, 'Prediction of failure behavior of adhesively bonded CFRP scarf joints using a cohesive zone model', *Eng Fract Mech*, vol. 228, Apr. 2020, doi: 10.1016/j.engfracmech.2020.106897.
- [35] 'GAVIÃO-INVESTIGAÇÃO E DESENVOLVIMENTO DE TECNOLOGIAS PARA PRODUÇÃO DE COMPONENTES DE AERONAVES DE LARGA ESCALA Document: E3.2.-Resultados do Desenvolvimento de Processos de Fabrico'.
- [36] 'HiMax / RTM6-Mechanical results NDA n°220117'.
- [37] 'HexTow ® AS7 Carbon Fiber', 2020. [Online]. Available: <http://www.hexcel.com/contact>
- [38] 'Matrix DS-Data Sheet Issue DT120 Versatile High Toughness Epoxy Matrix', 2020.
- [39] 'Typical-Fibre-properties—AQ-863'.
- [40] 'PTDS\_AE250(AS4)\_134-143gsmUDT'.
- [41] '3M™ Scotch-Weld™ Structural Epoxy Adhesive EC-9323 B/A', 2022. [Online]. Available: [www.3m.com/sds](http://www.3m.com/sds)
- [42] 'ISO 527-1-1993\_Tensile Properties'.
- [43] 'Standard Test Method for Mode I Interlaminar Fracture Toughness of Unidirectional Fiber-Reinforced Polymer Matrix Composites 1', doi: 10.1520/D5528\_D5528M-21.
- [44] 'Standard Test Method for Mode I Interlaminar Fracture Toughness of Unidirectional Fiber-Reinforced Polymer Matrix Composites 1', doi: 10.1520/D5528\_D5528M-21.
- [45] 'Standard Test Method for Determination of the Mode II Interlaminar Fracture Toughness of Unidirectional Fiber-Reinforced Polymer Matrix Composites 1', doi: 10.1520/D7905\_D7905M-19E01.
- [46] 'D 5868 - 01 (2014)'.
- [47] J. P. O. Pereira, R. G. S. G. Campilho, P. J. R. O. Nóvoa, F. J. G. Silva, and D. C. Gonçalves, 'Adherend effect on the peel strength of a brittle adhesive', in *Procedia Structural Integrity*, Elsevier B.V., 2021, pp. 722–729. doi: 10.1016/j.prostr.2022.02.002.
- [48] M. M. Arouche, S. Budhe, M. D. Banea, S. Teixeira de Freitas, and S. de Barros, 'Interlaminar adhesion assessment of carbon-epoxy laminates under salt water ageing using peel tests', *Proceedings of the Institution of Mechanical Engineers, Part L: Journal of Materials: Design and Applications*, vol. 233, no. 8, pp. 1555–1563, Aug. 2019, doi: 10.1177/1464420718766626.
- [49] S. T. de Freitas and J. Sinke, 'Test method to assess interface adhesion in composite bonding', *Applied Adhesion Science*, vol. 3, no. 1, Dec. 2015, doi: 10.1186/s40563-015-0033-5.

## References

---

- [50] 'Standard Test Method for Floating Roller Peel Resistance of Adhesives 1', doi: 10.1520/D3167-10.
- [51] J. P. R. Monteiro, R. D. S. G. Campilho, E. A. S. Marques, and L. F. M. da Silva, 'Experimental estimation of the mechanical and fracture properties of a new epoxy adhesive', *Applied Adhesion Science*, vol. 3, no. 1, Dec. 2015, doi: 10.1186/s40563-015-0056-y.
- [52] M. G. Cardoso, J. E. C. Pinto, R. D. S. G. Campilho, P. J. R. O. Nóvoa, F. J. G. Silva, and L. D. C. Ramalho, 'A new structural two-component epoxy adhesive: Strength and fracture characterization', in *Procedia Manufacturing*, Elsevier B.V., 2020, pp. 771–778. doi: 10.1016/j.promfg.2020.10.108.